PREDICTION OF OUTDOOR AND INDOOR VENTILATION OF HIGH-RISE BUILDING NEIGHBORHOODS BASED ON FLOW AND TURBULENCE AROUND BUILDINGS

PAN SHANSHAN

SCHOOL OF MECHANICAL AND AEROSPACE ENGINEERING

A thesis submitted to the Nanyang Technological University
in partial fulfillment of the requirement for the degree of
Master of Engineering

2015

Abstract

The global trend of urbanization has led to the increasing concern of the urban environment. Urban airflow which is directly related to pollutant dispersion and natural ventilation has attracted considerable amount of research interests. This thesis focuses on the airflow around high-rise building neighborhoods, based on which the outdoor and the indoor ventilation potentials are predicted.

A field measurement campaign was carried out in a high-rise residential building neighborhood in Singapore in the northeast and the southwest monsoon seasons. Ten integrated weather stations were installed at the pedestrian level and in the buildings to measure wind speed, wind direction and temperature. Reference wind speeds at the roof and at the airport were also measured. In general, strong mixing seems to exist in the neighborhood. It is found that the pedestrian level wind speed in the neighborhood is relatively uniform, being about 40% of the wind speed at the roof, when the angle of attack of the incident wind is less than 60°. The vertical wind profiles in the downwind buildings also vary little with height. In addition, the in-canopy turbulence also shows high spatial and temporal uniformity when normalized with the roof turbulence velocity.

For the neighborhood studied, the outdoor ventilation potential is equivalent to the amount of the airflow available within the neighborhood when the ambient flow condition is given. Hence, the wind speeds at the pedestrian level and in the buildings over height are converted to fractions of the airport wind speed and compared between the two monsoon seasons. It is found that this neighborhood is in the advantageous condition during the northeast monsoon because of the low upwind obstruction.

Two types of the indoor ventilation are covered, cross ventilation and single-sided ventilation.

Relatively good agreement is found between the measured cross-ventilation velocity in the neighborhood and the calculated velocity from the wind pressure coefficient. CFD simulations were performed on the single-sided ventilation to investigate the effect of turbulence intensity. The results suggest that the air change rate increases with increasing turbulence intensity when the window is on the windward or side walls.

Acknowledgement

First and foremost, I would like to express my deep sense of gratitude to my supervisors, **Prof. Leslie Keith Norford** and **Prof. Miao Jianmin** for their guidance and support in the past four years. Especially when I was faced with the hard decision lately, they helped me with all they can, giving me advice on both research and life. Being able to work with them is the best part of this four years' study.

I am very grateful to Prof. Rex Britter, who is always patient with my endless questions and inspires me with sparkling ideas. My sincere thanks to Dr. Terianne C. Hall, who shared her experience in CFD generously.

The field measurement would not be possible without the help of Dr. Mike Allen, Dr. Wang Wenqiang and Mr. Alex Toh in hardware building, programming and instrument installation. I owe them a great deal of gratitude.

I would like to thank all of my lab mates in the Micromachines Lab 1 for their constant support and valuable inputs to this work. Special thanks to Dr. Liu Shuwei, Dr. Liu Haobing, Dr. Ajay Kottapalli and Dr. Jing Xiangmeng, who have always been inspirational to me.

Technical staffs of the Micromachines Lab 1 are very supportive. Special thanks to Mr. Nordin Bin Abdul Kassim for his generous and timely help. I am also thankful to Ms. Jocelyn Sales and Ms. Maria Gotoking in SMART for their care during my stay in the MIT.

Finally, I would like to thank my family and friends for their love and support. They are my source of courage.

Thanks to the National Research Foundation of Singapore for funding this project through the Singapore-MIT Alliance for Research and Technology (SMART) and its Center for

Environmental Sensing and Modeling (CENSAM). Part of this project is in collaboration with Housing Development Board of Singapore (HDB) and conducted with the permission of Pasir-Ris Punggol Town Council of Singapore.

Table of Contents

Chapter 1 Introduction

Chapter 2 Literature Review

Chapter 3 Methodology

Chapter 4 Mean Flow and Turbulence and Prediction of Pedestrian Level Ventilation Potentials

Chapter 5 Estimation of Wind-Driven Natural Ventilation Rate

Chapter 6 Conclusion and Future Work

List of Tables

Chapter 2

Chapter 3

Chapter 4

Chapter 5

List of Figures

Chapter 1

Chapter 2

Chapter 3

Chapter 4

Chapter 5

List of Symbols

$\overline{\ }$	Overbar, meaning average.
A	Area of a window or other openings [m].
A_{eff}	Effective window area [m].
A_F	Frontal area of a roughness element [m^2].
A_P	Plan area of a roughness element [m^2].
A_T	Site area of a roughness element [m^2].
B	Breadth of the building [m].
C_D	Discharge coefficient of an opening [-].
C_d	Drag coefficient [-].
C_p	Wind pressure coefficient [-].
D	Molecular diffusion coefficient [m^2/s].
H	Building height [m].
I	Turbulence intensity [%].
J	Mass diffusion flux [kg/m^2-s].
L	Length of the building [m].
$\tilde{L}$	Length scale [m].
Q	Volumetric flow rate [m^3/s].
Q^*	Non-dimensional flow rate [m^3/s].
R_b	Bulk Richardson Number [-].
S	Rate of source release [kg/m^3-s].
T_H	Temperature at the building height [°C].
T_0	Surface temperature [°C].
T_a	Ambient temperature [°C].

U	Wind speed magnitude [m/s].
V	Ventilation velocity [m^3/s].
W	Width of a street canyon [m].
Y	Mass fraction of a species [-].
a	Attenuation coefficient [-].
c	Concentration [kg/m^3].
g	Gravitational acceleration [m/s^2].
k	Turbulence kinetic energy [m^2/s^2].
p	Pressure [pascal].
q	Volumetric tracer source [kg/m^3-s].
$\tilde{t}$	Time scale [s].
u, v	Velocity vector [m/s].
u', v', w'	The longitudinal, transverse and the vertical components of turbulence velocity [m/s].
u_B	Velocity scale resulted from buoyancy [m/s].
u_C	Characteristic wind speed [m/s].
u_H	Wind velocity at building height [m/s].
u_z	Wind velocity at height z [m/s].
u_*	Friction velocity [m/s].
z	A variable representing height [m].
z_d	Displacement height [m].
z_0	Surface roughness height [m].
α	Angle of attack [degree].
δ	Urban boundary layer thickness [m].
ϵ	Dissipation rate of turbulence kinetic energy [m^2/s^3].

θ	Wind direction relative to the true north [degree].
κ	Von Karman’s constant (0.4).
λ_f	Frontal area density [m^2/m^2].
λ_p	Plan area density [m^2/m^2].
μ	Viscosity of fluid [kg/m-s].
μ_t	Turbulence viscosity of fluid [kg/m-s].
ρ	Density [kg/m^3].
$\sigma_{u,v}$	Root mean square of u and v turbulent velocities [m/s].

Chapter 1 Introduction

1.1 Background and Motivation

In recent years, rapid urbanization is taking place all over the world. Cities expand their sizes and heights, and the increasing population density, especially in central urban areas, leads to challenging situations in infrastructure construction, urban hygiene, and other social economical aspects. The intensive human activities also exert stresses on the environment. The change of surface albedo and materials (from vegetation to concrete and asphalt) alters the solar gain and the energy budget of the urban areas, leading to the urban heat island effect and the change of rainfall patterns [1]. The construction of buildings increases the surface roughness and displaces the synoptic wind, resulting in the formation of the urban boundary layer (UBL) (Figure 1.1) which affects the dispersion of pollutants and air quality [1].

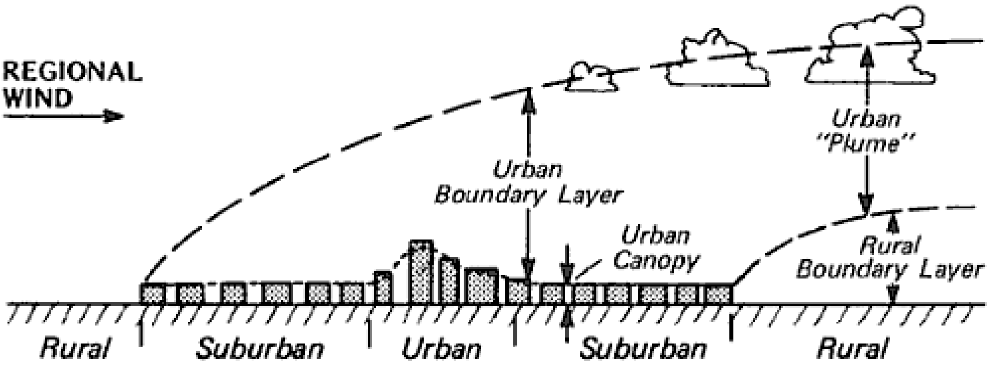

Figure 1.1 Schematic representation of the urban boundary layer [1].

The significance of the (negative) impacts of the urban development on the environment started being recognized in 1970s and some solutions have been proposed [2]. Nowadays, the idea of building a sustainable city is promoted throughout the world. Architectural designs and urban planning strategies that enable natural lighting and ventilations are advocated. New technologies such as solar panels, wind turbines fit for urban usage, and green roofs and walls that require little maintenance are applied to new buildings as well as the retrofit of existing buildings.

The effective designs and the proper application of new technologies could not be achieved without a good understanding of the physics of the interaction between the urban structures and the environment. Hence, numerous studies on urban climatology have been carried out, including studies on urban heat island effect [3-5], investigations on urban boundary layer, urban airflow and pollutant dispersion [6-8], studies on energy budget and species transport [9-10] and so on.

In many of these physical processes, the movement of air plays an important role, simply because the atmosphere is the medium in which these processes are taking place. The airflow can transport heat and pollutants from their sources of generation, mitigating the local intensity of the heat island effect and preventing the accumulation of pollutants at streets or near industrial exhaust vents. In the process of transportation, constant mixing happens and subsequently dilutes the pollutant concentration, in many cases to the degree that is no longer harmful to human. The dilution of pollutants can also reduce the likelihood of the production of certain hazardous chemical species through photochemical reactions, because it reduces the residence time of the reactants.

The airflow in the urban area is very complex, especially in the bottom layer of the UBL below the building height, which is the urban canopy layer (UCL) (Figure 1.1). The flow within this layer receives energy through momentum exchange with the high-speed airflow above it and loses energy due to the drag forces exerted by buildings and other obstacles [11]. Some characteristics of the airflow in the UCL include a) flowing at a reduced speed; b) constant changes of direction due to the blockage of buildings; and c) being subject to strong and frequent local disturbances such as acceleration around tall buildings, flow separation behind buildings, formation of vortices, etc [11]. The dependence of flow in the UCL on urban morphology makes it difficult a) to predict a local flow phenomenon accurately based on the general description of the flow in the UCL; and b) to obtain a general description of flow in the UCL from a few local flow observations.

As mentioned above, the knowledge of urban fluid dynamics is useful for many applications, but this study focuses on the ventilation of outdoor urban spaces and the natural ventilation of buildings. Although the regional wind pattern and the pollution sources determine the overall air quality of a city, studies have shown that the pollutant concentration in a well-ventilated urban area can be significantly different from an area with similar building density but different morphologies given the same pollution sources and the input wind [12]. Therefore, localized investigations of various types of outdoor spaces are necessary. Indoor ventilation is even more essential because people spend up to 90% of their time in buildings [13]. In some tropical countries, the HVAC systems account for up to 70% of the total energy consumption of the building [14]. Hence, if natural ventilation can be implemented, it can save a substantial amount of energy as well as provides a more natural and pleasant environment for the residents.

The specific urban morphology studied in this project is the high-rise residential building groups in densely-populated cities. To accommodate the increasing population in the limited city areas, the construction of high-rise buildings is inevitable throughout the world. Cities such as Hong Kong, Shanghai, New York and Singapore are good examples. The high-rise buildings pose more challenges because they disturb the flow more drastically, amplifying the gusts formed at the bottom of the buildings and distorting the shear layer above the buildings [15]. The deeper urban canopy also makes it more difficult for air exchange between the canopy and the atmosphere above [16].

In the current study, a two-season outdoor airflow field measurement was carried out in a representative high-rise residential building group in Singapore, where mean flow and turbulence statistics at the pedestrian level and at several heights were measured and analyzed under different background flow conditions. With moderate generalization and approximation, the ventilation rate of the outdoor space between buildings could be estimated. Afterwards, the ventilation of buildings was studied. The cross-ventilation flow rate could be calculated based on the urban density and was then compared to the actual measurement. Numerical simulations on single-sided ventilation were performed to assess its practicality. Influencing factors such as the wind angle and the turbulence intensity were also investigated.

1.2 Objective

This work aims to

1) Develop an in-depth understanding of the mean flow and turbulence in a typical high-rise residential building neighborhood in Singapore;

2) Quantify the ventilation potential of the outdoor spaces in the high-rise residential building neighborhood; and

3) Estimate the indoor ventilation potentials through cross-ventilation and single-sided ventilation.

1.3 Organization of Report

Chapter 2 reviews the relevant literature in urban airflow, cross ventilation and single-sided ventilation. It starts with an introduction of the structure of the urban boundary layer. Several theoretical models on the mean flow and turbulence profiles on different spatial scales are discussed. The two ventilation mechanisms of buildings, cross ventilation and single-sided ventilation, are reviewed last.

Chapter 3 presents the methodology of this research. The field measurement site and the procedures are described in details, followed by a general introduction of the CFD modeling.

The results obtained from the field measurement are presented in Chapter 4, including temperature variations and stability conditions, mean flow at the pedestrian level and its vertical profile and the turbulence statistics. The local wind data are linked to the airport or the rooftop reference station to produce dimensionless ratios which can be used to estimate the outdoor ventilation rate if only the wind condition at the reference stations are known. Since the measurement data are available from both northeast and southwest monsoon seasons, cross-season comparisons are made.

In Chapter 5 the cross-ventilation flow rate of the building is calculated from the estimated wind pressure coefficients and compared with the actual measurement. CFD simulations on the single-sided ventilation are conducted. The model is validated by a wind-tunnel experiment. The dependence of the single-sided ventilation flow rate on the wind angle and turbulence intensity is studied.

Chapter 6 concludes the thesis and proposes the future work.

References

1. Oke, T. *Boundary Layer Climates, 2nd ed*. New York: Routledge, 1987.

2. Urban Ecology, http://www.urbanecology.org/, [15 Oct 2014].

3. Chow, W. T. L., and Roth, M., "Temporal Dynamics of the Urban Heat Island of Singapore," *International Journal of Climatology*, 26, pp 2243-2260, 2006.

4. Chow, W. T. L., Brennan, D., and Brazel, A. J., "Urban Heat Lsland Research in Phoenix, Arizona: theoretical Contributions and Policy Applications," *Bulletin of American Meteorological Society*, 93, pp 517-530, 2012.

5. Santamouris, M., "On the Energy Impact of Urban Heat Island and Global Warming on Buildings," *Energy and Buildings*, 82, pp 100-113, 2014.

6. Rotach, M.W., Vogt, R., Bernhofer, C., Batchvarova, E., Christen, A., Clappier, A., Feddersen, B., Gryning, S.-E., Martucci, G., Mayer, H., Mitev, V., Oke, T.R., Parlow, E., Richner, H., Roth, M., Roulet, Y.-A., Ruffieux, D., Salmond, J.A., Schatzmann, M., and Voogt, J.A., "BUBBLE – an Urban Boudary Layer Meterology Project," *Theoretical and Applied Climatology*, vol 81, pp 231-261, 2005.

7. DAPPLE – Dispersion of Air Pollution and Penetration into the Local Environment project, http://www.dapple.org.uk/index.html, Apr 2013 [15 Oct 2014].

8. Balogun, A.A., Tomlin, A.S., Wood, C.R., Barlow, J.F., Belcher, S.E., Smalley, R.J., Lingard, J.J.N., Arnold, S.J., Dobre, A., Robins, A.G., Martin, D., and Shallcross, D.E., "In-street wind direction variability in the vicinity of a busy intersection in central London," *Boundary-layer Meteorology* vol. 136 pp 489-513, 2010.

9. Harman, I. N., “The Role of Roughness Sublayer Dynamics within Surface Exchange Schemes,” *Boundary-Layer Meteorology*, 142, pp 1-20, 2012.

10. Velasco, E., Roth, M., Tan, S.H., Quak, M., Nabarro, S.D.A, and Norford, L., “The Role of Vegetation in the CO_2 Flux from a Tropical Urban Neighbourhood,” *Atmospheric Chemistry and Physics*, 13, pp 10185-10202, 2013.

11. Britter, R. E., and Di Sabatino, S. “Chapter 7 Flow through Urban Canopies,” in *Handbook of Envionmental Fluid Dynamics Volume Two*, Fernando, H. J. S. Ed. CRC Press/Taylor & Francis Group, 2013.

12. Yuan, C., Ng, E., and Norford, L. K., “Improving Air Quality in High-Density Cities by Understanding the Relationship between Air Pollutant Dispersion and Urban Morphologies,” *Building and Environment*, 71, pp 245-258, 2014.

13. Sherman, M., “ASHRAE’s New Residential Ventilation Standard,” *ASHRAE Journal’s Official Product & Show Guide*, pp S149-S156, 2004.

14. National Environment Agency, “Singapore’s Second National Communication: Under the United Nations Framework Convention on Climate Change,” NEA, Singapore, Nov, 2010.

15. Blocken, B. and Carmeliet, J. “Pedestrian Wind Environment around Buildings: Literature Review and Practical Examples,” *Journal of Thermal Environment and Building Science*, 28, pp 107-159, 2004.

16. Hang, J., Li, Y., Buccolieri, R., Sandberg, M., and Di Sabatino, S., “On the Contribution of Mean Flow and Turbulence to City Breathability: The Case of Long Streets with Tall Buildings,” *Science of the Total Environment*, 416, pp 362-373, 2012.

Chapter 2 Literature Review

2.1 Urban Boundary Layer

2.1.1 The Structure of the Urban Boundary Layer

Like any viscous fluid that flows over a rough surface, a boundary layer develops in the lowest 100 m to 3000 m of the atmosphere in response to the influence of the Earth’s surface. It is called the atmospheric boundary layer or planetary boundary layer [1]. The urban boundary layer (UBL) specifically refers to the atmospheric boundary layer over urban areas, whose characteristics are governed by urban surface roughness, such as asphalt ground, high-rise buildings and street networks [2] (Figure 2.1a).

The region of most interest is the surface layer which is comprised of the inertial sublayer and the roughness sublayer (Figure 2.1b). The inertial sublayer is comparable to the inertial sublayer in the classic turbulent boundary layer theory, where the logarithmic velocity profile is found and the Reynolds stress is approximately constant [3]. In this region, the impacts of individual buildings are mixed and indiscernible, thus the meteorological properties measured in this layer should be representative of the entire local area [4]. It is generally accepted that the inertial sublayer starts from $2H$ to 0.25δ, where H is the average building height and δ is the UBL thickness [5].

Beneath the inertial sublayer is the roughness sublayer, where the micro-scale effects produced by each roughness element exist and interact. Wind speed and turbulence characteristics here can be highly temporally and spatially varying. The Urban Canopy Layer (UCL) is at the very bottom below the average building height [4].

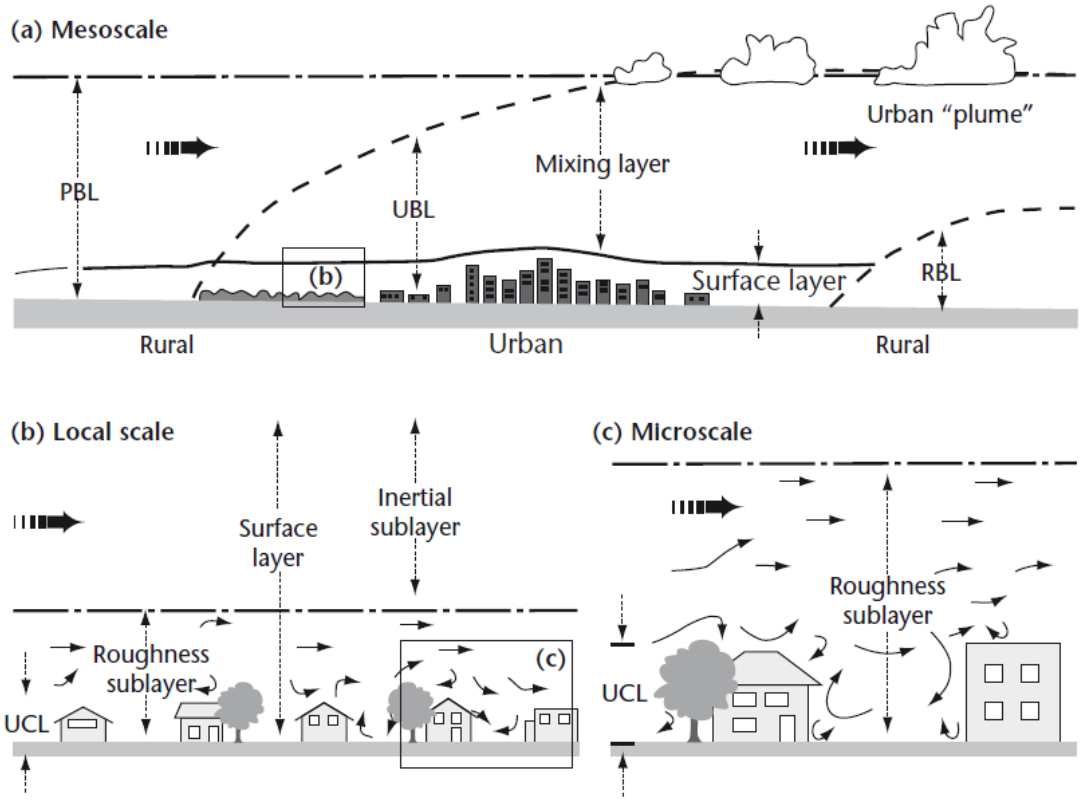

Figure 2.1 Schematic diagram of urban boundary layer structures [4].

2.1.2 The Scales of the Urban Boundary Layer

When dealing with fluid mechanics problems, scaling is always an important part. Similarly in urban airflow studies, it is necessary to tackle different problems differently according to their relevant scales. The length scales and the time scales can be related through $\tilde{L} = U\tilde{t}$, where U is an appropriate wind velocity [6]. For the current study, the airflow properties on three length scales are concerned: city scale (average city area, 10 or 20 km), neighborhood scale (1 or 2 km) and street scale (100 or 200 m) [6].

Studies on the city scale investigate the integrated impact of the whole urban landscape on the airflow above the city. Normally the entire urban area is taken as one, described by parameters such as the roughness height z_0 and the displacement height z_d (Figure 2.2). The disturbances produced by individual roughness elements are averaged out. The flow in the inertial sublayer can be studied on this scale [6-7].

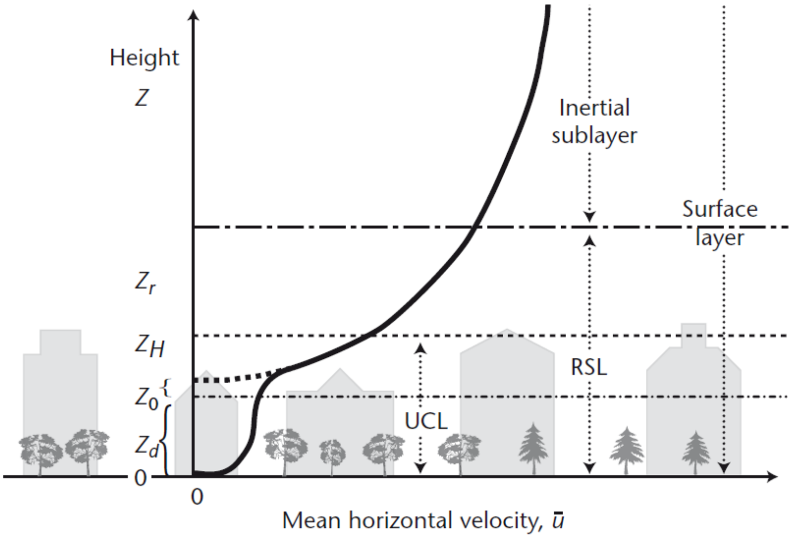

Figure 2.2 Generalized mean wind velocity profile in a dense urban area. Displacement height scale z_d, roughness height scale z_0, average building height z_H and the roughness sublayer height z_r are indicated [4].

The neighborhood scale and the street scale deal with flow within the urban canopy layer. The neighborhood scale is intended for a spatial range of several neighborhoods of similar building types. On this scale wind velocity and turbulence in the immediate area around buildings are the interest of study. The high non-uniformity of the flow field is often treated by using spatially averaged variables in the mathematical models [8-9].

The street scale addresses flow within or near one or two individual streets, buildings or intersections [6]. This scale is feasible for detailed mapping of airflow, pollutant concentration, etc. by field measurements, wind tunnel experiments and numerical simulations such as Large-Eddy Simulation. The flow properties are subject to strong variations with local geometry, posing challenges on the generalization of findings [10-11].

The different spatial scales form “a hierarchy of complexity” [6]. The knowledge of the flow on a smaller scale helps to accurately parameterize its flow properties into the model of the next-larger scale. On the contrary, the information on a larger scale can provide useful boundary conditions for the modeling of the flow on the next-smaller scale.

2.2 Airflow on the City Scale

2.2.1 Wind Profile in the Inertial Sublayer

As mentioned above, the flow and turbulence characteristics in the inertial sublayer represent the processes happening on the city scale. It is generally accepted that the mean velocity profile in the inertial sublayer follows the logarithmic law in neutral stability [1],

$$u_z = \frac{u_*}{\kappa} \ln\left(\frac{z - z_d}{z_0}\right), \tag{2.1}$$

where z_d is the displacement height, z_0 is the surface roughness height, u_* is the friction velocity ($u_* = \sqrt{\tau_{wall}/\rho}$), and κ is the von Karman’s constant (0.4). It should be emphasized that this equation is only applicable in the inertial sublayer. Any attempt to extrapolate the profile down into the roughness sublayer is fundamentally wrong.

2.4.3 Estimation of Surface Roughness

To solve the wind speed using the logarithmic wind profile (Equation 2.1), the knowledge of z_0 and z_d is required. There are two methods to determine z_0 and z_d [7]:

1) Morphometric methods that derive the two parameters from surface morphology or the geometry of roughness obstacles. For example, z_0 and z_d are related to building height, width and spacing.

2) Micrometeorological methods that measure the wind speed at multiple heights in the inertial sublayer and fit the data with the logarithmic profile to obtain the corresponding z_0 and z_d.

Morphometric methods would have great advantages if they were universally applicable. However, the equations which describe z_0 and z_d often involve empirical coefficients that are derived from wind tunnel experiments of unidirectional flow over regularly arranged simple geometries. It is doubtful whether they can represent the real cities. Micrometeorological methods are not constrained by the complexity of the surface, but they are laborious and site dependent.

Substantial efforts have been devoted to the parameterization of urban surfaces, but no method has been proved to be outstandingly effective so far [7]. The roughness height, z_0 increases with increasing building density, but after a certain point when buildings are so closely packed that the flow only skims over the top of the buildings, z_0 begins to decrease. The displacement height, z_d increases monotonically with increasing building density, but the relation is not straightforward.

The simplest method of estimating z_0 and z_d is the "rule of thumb", which establishes the first-order relations between z_0 and z_d and the averaged building height ($\overline{H}$).

$$z_0 = 0.1\overline{H}; \tag{2.2}$$

$$z_d = 0.7\overline{H}. \tag{2.3}$$

Though unable to depict the full picture of z_0 and z_d variations, these relations provide a rough idea of the magnitude of the two length scales. The validity of the rule of thumb has been proved by many studies [7].

There are many more complex methods to compute the parameters z_0 and z_d. Grimond and Oke [7] provided a comprehensive review on the existing methods. They found that the parameters calculated from the methods proposed by Bottema [12-13] and Macdonald et al.

[14] had the best match with the z_0 and z_d calculated from the field measurement data.

2.3 Airflow on the Neighborhood Scale

Compared to the city scale, more homogeneity in surface roughness (i.e. buildings) can be found on the neighborhood scale of 1-2 km, which makes it valid to take the spatially averaged values as indicators of the airflow characteristics of a neighborhood. Studies on the airflow within the UCL also tend to base their experiments on this scale because a) the flow is close to the fully developed stage after passing a fetch of this distance (for homogeneous terrain types) [4]; b) and it is more feasible to construct wind tunnel models or computational models with enough details on this scale [14-15].

2.3.1 The Mean Velocity Profile

There are some disputes about the existence of a meaningful mean velocity profile below the inertial sublayer and the shape of it [6], but it is generally agreed that the wind velocity is slower and more uniform in the urban canopy layer than above it [16].

2.3.1.1 Exponential Velocity Profile

Macdonald [17] derived an exponential mean-velocity profile for the flow in the UCL, based on the original work by Cionco [18] on flow in an ideal vegetative canopy. Started from balancing the shear stress over an area and the pressure drag force on the roughness elements in that area, using the Prandtl mixing-length model, Macdonald [17] arrived at the following equation

$$u_z = u_H \exp\left[a\left(\frac{z}{H} - 1\right)\right], \tag{2.4}$$

where u_H is the wind velocity at the building height $H$and a is the attenuation coefficient. He then performed curve-fitting on the empirical data obtained from the wind tunnel experiments of in-line and staggered cube arrays [14] and provided an estimate of a by $a = 9.6\ \lambda_f$.

The frontal area density λ_f is defined as the ratio of the frontal area of the building (A_F), which is the area perpendicular to the wind direction, to the total plot area (A_T) (Figure 2.3).

$$\lambda_f = \frac{A_F}{A_T} \tag{2.5}$$

A related parameter is the plan area density λ_p which is defined as the ratio of the plan area (A_P) of the building to the total plot area (A_T) (Figure 2.3).

$$\lambda_p = \frac{A_p}{A_T} \tag{2.6}$$

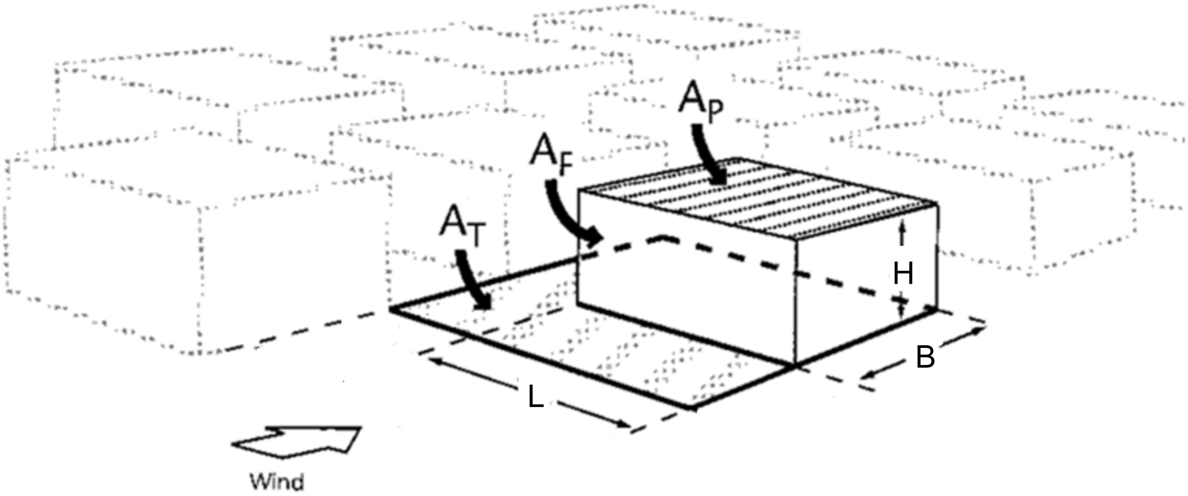

Figure 2.3 Definition of surface dimensions. Modified from [7].

Plotting Equation 2.4 in the form of normalized velocity u_z/u_H against normalized height z/z_H at different frontal area densities (Figure 2.4), the profiles shift toward lower speed with increasing λ_f. It should be noted that the speed does not decrease to zero at z = 0, which implies the inability of Macdonald's model to predict velocity very close to the ground.

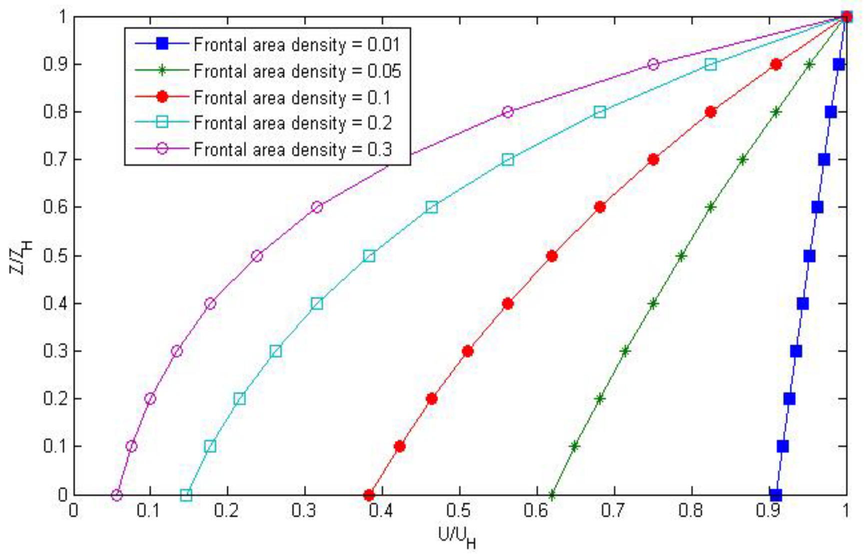

Figure 2.4 Normalized velocity profiles at different frontal area densities.

Macdonald’s model is subject to two other constraints. Firstly, it is only suitable for low-packing-density obstacle arrays where $\lambda_f < 0.3$, because otherwise the recirculation vortices formed between rows of buildings would change the flow pattern fundamentally. Secondly, the model requires the knowledge of the wind speed at the building height, which is very difficult to accurately measure because the existing shear layer produces a large velocity gradient at that height.

2.3.1.2 Constant Velocity Profile

Some experimental results have shown a very uniform velocity profile below the building height with different packing densities λ_f or λ_p (Figure 2.5) [19-21]. Based on these, Bentham and Britter [22] argued that a single constant wind speed could be used to characterize the velocity in the urban canopy layer. Derived also from the balance between the surface shear stress and the pressure drag on the obstacles, the characteristic velocity scaled by the friction velocity is a function of λ_f,

$$\frac{u_c}{u_*} = \left(\frac{C_d}{2}\lambda_f\right)^{-1/2}, \tag{2.7}$$

Where u_* is the friction velocity in the inertial sublayer rather than that derived from the local Reynolds stress. C_d is the drag coefficient, which is equal to 1 for cubic obstacles [22].

They also suggested that for densely packed buildings (λ_f > 0.2), λ_f was the proper descriptor of the surface roughness; thus

$$\frac{u_c}{u_*} = (\frac{\lambda_f}{2})^{-1/2}, \tag{2.8}$$

However, when λ_f < 0.2, λ_f should be replaced by z_0/z_H , giving

$$\frac{u_c}{u_*} = (\frac{z_0}{2z_H})^{-1/2}. \tag{2.9}$$

The model have shown good agreement with several sets of existing wind tunnel data, the λ_f of which ranges from 0.01 to 0.44, but the author claimed that the model should be applicable to even higher packing densities.

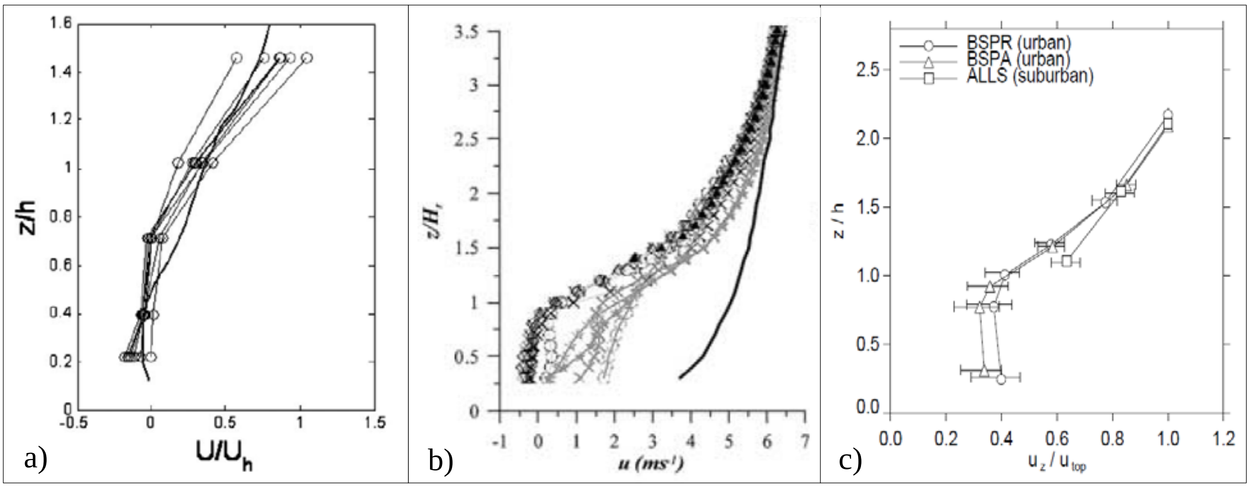

Figure 2.5 The mean velocity profile plotted against height normalized by the average building height from a) the MUST field experiment (λ_f = 0.1)[19]; b) wind tunnel model of the central part of Nantes, France (Black lines represent measurement in the canyons) (0.4 <

$\lambda_p < 0.8$) [20]; and c) field measurements in two urban canyons in Basel, Switzerland (λ_p = 0.57, 0.42) [21].

2.3.2 Turbulence

The turbulence profile in the urban area has three distinct regions, with the maximum value occurring around the building height and more uniform profiles below and above it [6]. For the turbulence above the building height, Roth [23] has done an extensive review on the experiments and found that the turbulence above the roughness sublayer ($z/z_H > 2.5$) had small deviations of the urban average, u'/u_{*_Loc}, v'/u_{*_Loc}, w'/u_{*_Loc} = [2.32 ± 0.16, 1.81 ± 0.20, 1.25 ± 0.07], where u_{*_Loc} is the square root of the local Reynolds stress. Louka et al. [24] and Christen et al. [21] also reported relatively uniform turbulence profiles above 1.25 z_H in their field experiments in street canyons.

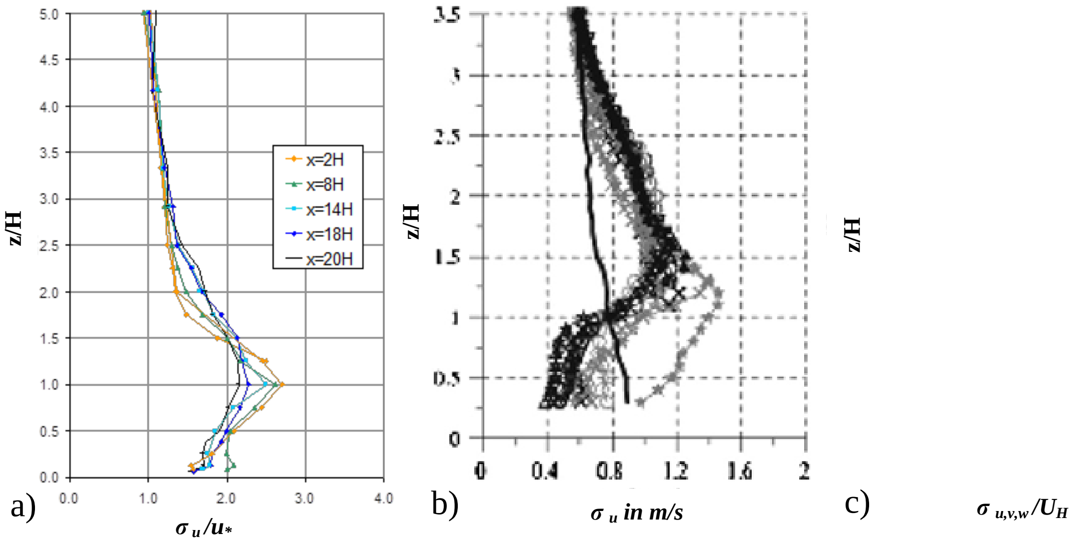

Figure 2.6 a) The vertical profiles of the longitudinal component of turbulence velocity scaled by the square root of the maximum Reynolds stress and measured at different longitudinal locations [25]. b) The vertical profile of the longitudinal component of turbulence velocity. The u_* in the inertial sublayer is 0.6 m/s [26]. c) The vertical profiles of all three turbulence

velocity components scaled by the mean wind velocity at the building height u_H [27]. Modified from [28].

Limited data are available for turbulence below the building height in the urban canopy layer. Figure 2.6 presents the turbulence profiles of three wind tunnel studies [25-28]. A few observations can be made. The maximum turbulence occurs between 1-1.5 z_H and all the three components of the turbulence velocity are quite uniform below the building height. Hence, it is valid to average the turbulence velocity over height within the UCL to obtain a single value which is expected to be a function of the morphology.

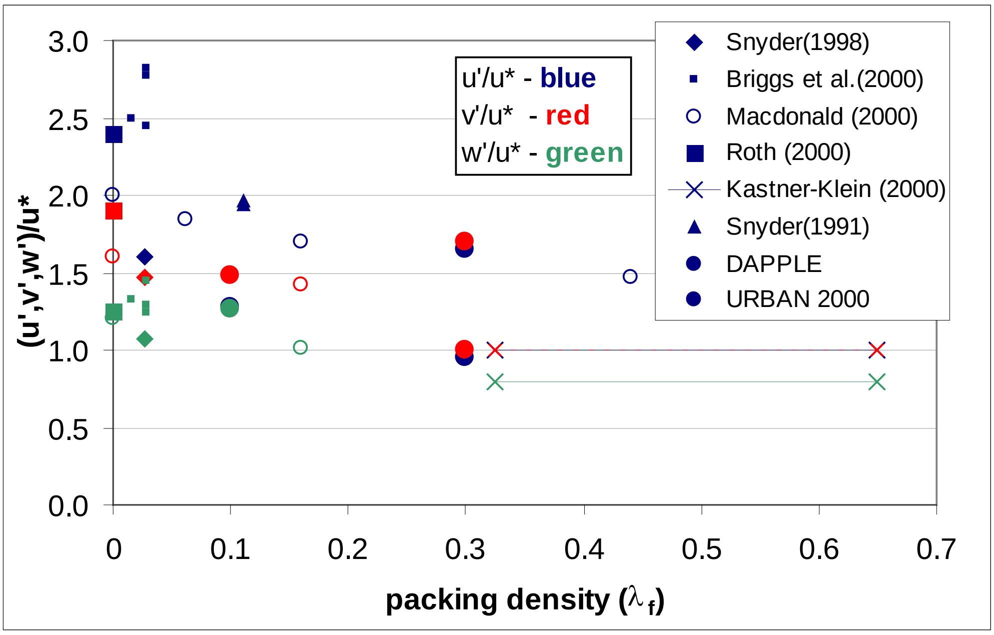

Figure 2.7 $(u',v',w')/u*$ plotted against λ_f [28].

Lloyd [28] have reviewed several studies and used a volume averaging method, i.e. averaging over vertical and horizontal spaces, to obtain a single value of each turbulence velocity component scaled by u_*. She then plotted them against the packing density λ_f (Figure 2.7). The best-fit curves for each component (u', v', w') are shown in Figure 2.8 [28]. The turbulence level decreases with increasing λ_f first and stops decreasing when $\lambda_f > 0.4$. The final turbulence levels are $(u',v',w')/u_* \approx [1.0, 1.0, 0.8]$.

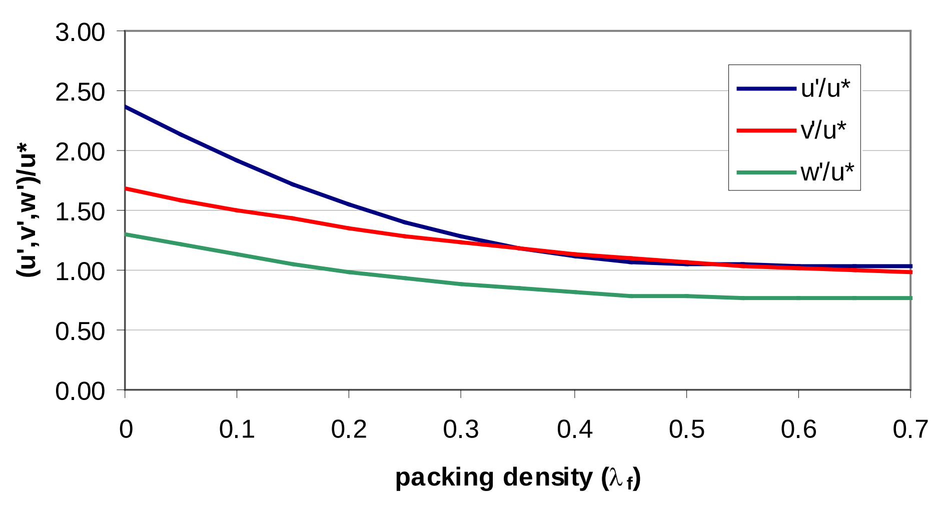

Figure 2.8 The best-fit curves for each turbulence velocity component [28].

2.4 Airflow on the Street Scale

The typical street-scale structure is the street canyon. The key parameter that determines the flow pattern in a street canyon is the ratio of the building height to the width of the street, the aspect ratio *H/W*. For flow perpendicular to a street canyon, three flow regimes can occur depending on the aspect ratio (Figure 2.9) [2]. When the separation between buildings is sufficient ($H/W < 0.3$), the buildings act like isolated roughness elements. This is the isolated roughness flow regime (Figure 2.9a). When buildings get closer ($0.3 < H/W < 0.65$), the recirculation vortex behind the upwind building interferes with the frontal vortex of the downwind building, creating the wake interference flow (Figure 2.9b). At even smaller separation ($H/W > 0.65$), the main flow skims over the top of the buildings without entering the space between the buildings (Figure 2.9c). Steady recirculation vortices (more than one vortex when $H/W > 1$ [29]) form in the space, driven by the shear flow above the buildings. Building arrays in the skimming flow regime are subjected to stagnant air flow and ineffective pollutant dispersion, and thus often considered the worst case in thermal comfort and dispersion studies.

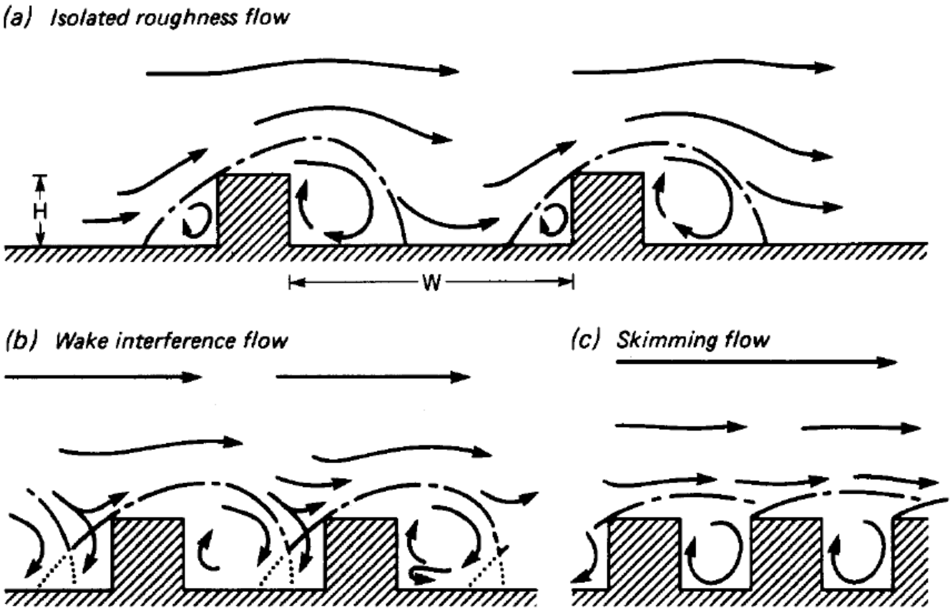

Figure 2.9 Flow regimes associated with street canyons [2] pp 267.

At the end of the street canyon, the flow separates from the upwind building and forms a horizontal recirculation vortex which can extend 2-3*H* into the street canyon if the length of the street is sufficient (Figure 2.10) [30-31]. When the flow comes at an angle to the normal of the street, the horizontal recirculation vortex at the upwind street end is stretched and the recirculation vortex at the downwind end hardly maintains. A helical vortex forms along the street [2, 32-33]. When the angle increases, at a certain point, flow is merely channeled down the street, destroying the vertical and horizontal vortices.

Street canyons tend to be the focus of pollution dispersion study because they are the source of traffic pollution and have concentrated human activities. Hence, the flow condition in a street canyon near ground level is of crucial interest. Table 2.1 summaries a few recent field measurements that were carried out in street canyons and reported the mean wind speed at/near the ground level. Since the ground wind speed was normalized by different reference wind speeds in different studies, it is hard to cross-compare over different *H/W*. Roughly, for 1.06 < *H/W* < 1.4, the ground wind speed is about 2/3 of the wind speed at the building height (Study No. 1, 2 and 3). For *H/W* < 1, the ground wind speed is about 0.4 times of the wind speed in the inertial sublayer at 2*H* (Study No. 4 and 7).

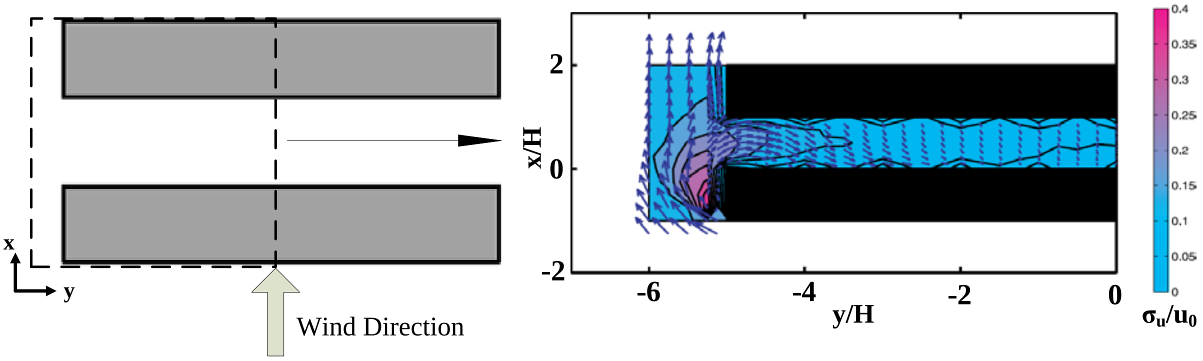

Figure 2.10 A CFD simulation shows the formation of an end vortex in a street canyon with perpendicular approaching flow. The arrows represent velocity vector. The color scale represents the turbulence level. Modified from [30].

Table 2.1 Some recent urban street canyon field measurements. *U* is the scalar wind speed.

No.	Reference	Street Canyon Aspect Ratio, H/W	Normalized ground wind speed
1	DePaul & Sheih, 1986 [34]	1.4	$U_{0.06H}/U_{1.2H} = 0.63$
2	Nakamura & Oke, 1988 [35]	1.06	$U_{0.06H}/U_{1.2H} = 0.69$
3	Rotach, 1995 [36]	1.22	$U_{\text{canyon avg}}/U_{1.15H} = 0.73$
4	Christen et al. 2003 [21]	1, 0.56	$U_{0.25H}/U_{2.2H} \approx 0.4$
5	Klein & Clark, 2007 [37]	2.6	$U_p/U_{4H} < 0.2^{+}$
6	Niachou et al., 2008[38]	1.7	$U_{0.16H}/U_{1.1\mathrm{H}} = 0.2$
7	Dallman et al., 2014 [39]	0.67	$U_{0.4H}/U_{2H} = 0.42$

$^{+}U_p$ are measured at 3 meter above ground.

2.5 Natural Ventilation of Buildings

Natural ventilation is driven by pressure differences between the indoor and the outdoor environments. The flow equation of windows and other intentional large openings shows clear relation between flow rate and the pressure difference across the openings,

$$Q = C_D A \sqrt{\frac{2\Delta p}{\rho}}. \tag{2.10}$$

where Δp is the pressure difference, ρ is the air density, A is the opening area, C_D is the dimensionless discharge coefficient of the opening [40]. The pressure difference can be induced by the temperature difference (the stack effect), the mean wind velocity field around the building envelope, and the turbulence fluctuation which causes pressure fluctuation [41]. The following sections will review the wind-driven natural ventilation for cross ventilation and single-sided ventilation.

2.5.1 Wind Pressure Coefficient

For wind-induced cross ventilation the flow is moved because the pressure field on the windward side of the building is larger than that of the leeward side. The pressure on the building exterior can be non-dimensionalized by the normal pressure scale ρU^2. The pattern of the dimensionless pressure depends only on the geometry of the building, the direction of wind but no longer the wind speed. In other words, the pressure distribution on the building exterior is fixed for an incoming wind direction [42]. In this manner, the wind pressure coefficient can be defined,

$$p = C_p \rho \frac{{U_{ref}}^2}{2} \tag{2.11}$$

Where p is wind surface pressure relative to outdoor static pressure, ρ is air density and U_{ref} is a reference wind speed, and C_p is the wind pressure coefficient [40]. The value of C_p depends also on the choice of the reference wind speed U_{ref}.

2.5.2 Single-Sided Ventilation

Although cross-ventilation is a preferred mechanism for ventilation, it is hard to achieve in such places as classrooms or cellular offices. For a room with a single opening, the two-way flow driven by the thermal effect can be significant. However, this section intends to survey the literature on pure wind-driven single-sided ventilation.

Similar to the case of cross-ventilation, both mean flow and the turbulence exchange play a role in single-sided ventilation. The contribution of these two components varies depending on the building geometry and the angle of the window [43-44]. Bu and Kato [44] found in their LES simulation that the turbulence exchange accounts for more than half of the total air exchange of a room with only a windward or leeward opening in the building array. A counterintuitive finding from the simulations and the experiments is that mean flow across the window exists even when the window is normal to the incoming flow direction [45]. A satisfactory explanation or theoretical model for this has not been proposed. Wand and Chen [43] argued that it was because the incoming flow had developed a power-law profile thus the wind speed was different over the height of the window, but it could not explain why the same phenomenon was observed in the wind tunnel experiment with uniform input wind speed [45].

Based on the wind tunnel experiments on an isolated low-rise building, Warren and Parkins [46] proposed an empirical formula that predicted the overall wind-driven single-sided ventilation flow rate (including both mean flow and turbulence)

$$Q = 0.025AU_R \tag{2.12}$$

where A is the window area and U_R is a reference wind speed measured at the standard height. For wind tunnel experiments using uniform inlet wind speed, U_R is that wind speed. Although Equation 2.12 is a rough estimate, it is useful in identifying that the ventilation flow rate is independent of the ambient wind speed. Furthermore, based on this formula, a non-dimensional flow rate (Q^*) can be derived

$$Q^* = \frac{Q}{AU} \tag{2.13}$$

and it is more sensible to relate wind angle and turbulence intensity to Q^* because these variables are dimensionally consistent.

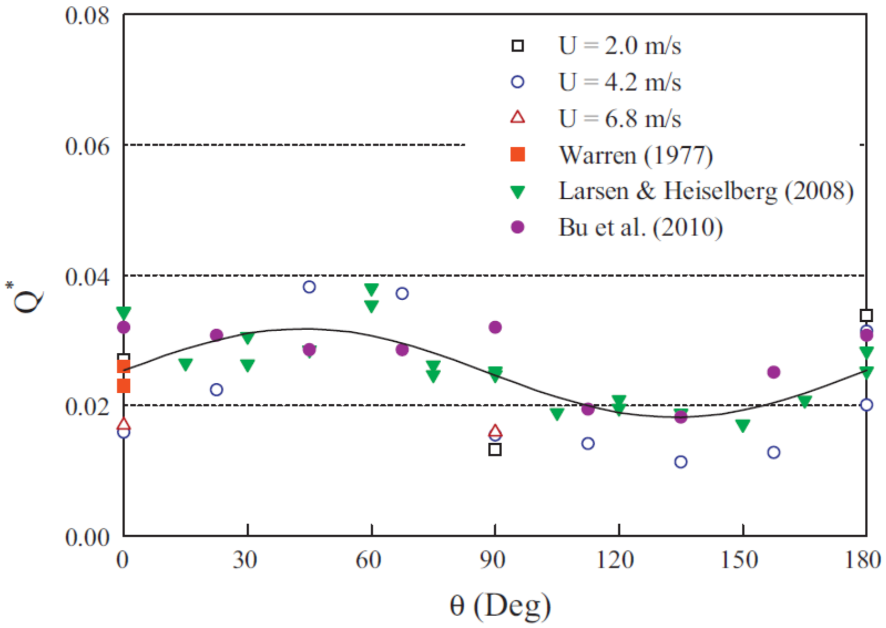

Figure 2.11 Dimensionless ventilation rate Q^* as a function of wind direction angle [47].

Only a few studies have systematically investigated the effect of wind angle and turbulence intensity in single-sided ventilation flow rate. Chu et al. [47] conducted wind-tunnel experiments and summarized the data from previous experiments, arriving at a sinusoidal relation between Q^* and the angle (Figure 2.11). However, the data lie in a relative narrow range [0.015, 0.04] compared to the Q^* of a cross-ventilated room ($Q^* = 0.08$ [47]). Hence, when it comes to estimating the difference between the Q^* of a room with a single opening and the Q^* of the same room with two openings, using $Q^*_{single\text{-}sided} \approx 0.025$ is feasible. The effect of turbulence intensity was demonstrated by Warren and Parkins [46] (Figure 2.12). The ventilation rate with higher turbulence intensity (9% instead of 0.8%) is significantly higher.

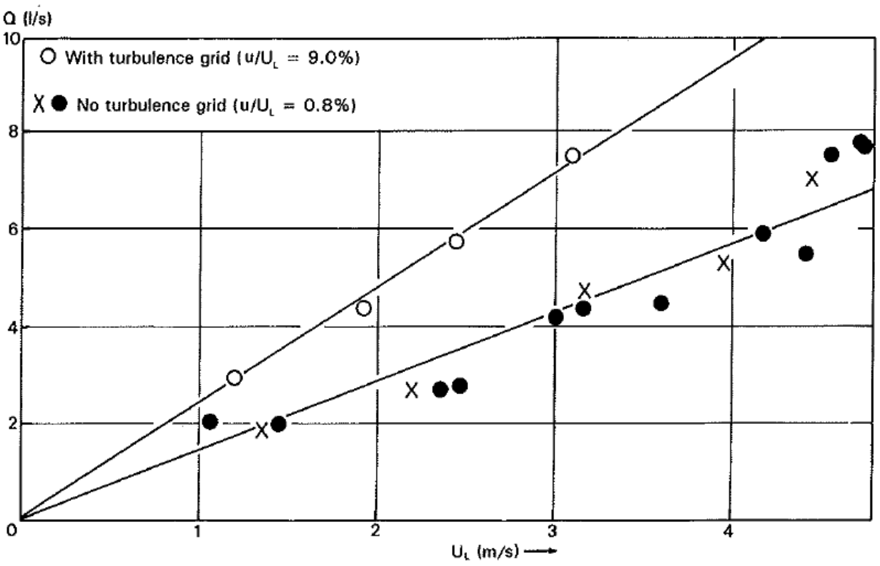

Figure 2.12 Variation rate of Q with wind-tunnel velocity at different with and without turbulence grid [46].

2.6 Summary

This chapter reviewed the structure of the urban boundary layer and the key characteristics of the mean flow velocity and the turbulence profiles on different scales. Most of these findings are obtained and verified by wind tunnel experiments and numerical simulations, while full-scale field measurement data are rare. Full-scale field measurements can be very important because it reflects the real-world conditions reducing the risk of overlook of certain key parameters in the process of setting up the simulated environment. Moreover, most of the studies were conducted in Europe or North America, where low-rise buildings dominate the morphology. The airflow around high-rise buildings is less known. It is also a question whether the theoretical results obtained from low-rise buildings are also applicable to high-rise buildings. As a result, the current project involving the flow measurement around high-rise building groups is proposed.

References

1. Stull, R. B. *An Introduction ot Boundary Layer Meteorology*. Dordrecht, The Netherlands: Kluwer Academic Publishers, 1997.

2. Oke, T. *Boundary Layer Climates, 2nd ed*. New York: Routledge, 1987.

3. Tennekes, H., and Lumley, J. L., *A First Course in Turbulence*. Cambridge, Massachusetts: The MIT Press, 1972.

4. World Meteorological Organization. "WMO Guide to Meteorological Instruments and Methods of Observation, Part II Observing Systems, Chapter 11 Urban Observation," Internet:ftp://ftp.wmo.int/Documents/MediaPublic/Publications/WMO8_CIMOguide/WMO8_Ed2008_Up2010_en.pdf. Aug, 2008 [27 Oct 2014].

5. Raupach, M. R., Thom, A. S., and Edwards, I. "A Wind-Tunnel Study of Turbulent Flow Close to Regularly Arrayed Rough Surfaces," *Boundary-layer Meteorology,* 18, pp373-397, 1980.

6. Britter, R. E., and Hanna, S. R. "Flow and Dispersion in Urban Areas," *Annual Review of Fluid Mechanics*, 35, pp 469-496, 2003.

7. Grimmond, C. S. B., and Oke, T. R. "Aerodynamic Properties of Urban Areas Derived from Analysis of Surface Form," *Journal of Applied Meteorology*, 38, pp 1262-1292, 1999.

8. Bentham, T., and Britter, R. " Spatially Averaged Flow within Obstacle Arrays," *Atmospheric Environment*, 37,pp. 2037-2043. 2003.

9. Di Sabatino, S., Solazzo, E., Paradisi, P., and Britter, R. "A Simple Model for Saptially-

averaged Wind Profiles Within and Above an Urban Canopy," *Boundary-Layer Meteorology*, 127, pp 131-151, 2008.

10. Brown, M.J., Khalsa, H., Nelson, M., and Boswell, D., "Street Canyon Flow Patterns in a Horizontal PlaneL Measurements from the Joint Urban 2003 Field Experiment," in *Proceedings of AMS Symposium on the Urban Environment,* Vancouver, B.C., 2004.

11. Li, X.-X., Liu, C.-H., and Leung, D. Y. C., "Large-Eddy Simulation of Flow and Pollutant Dispersion in High-Aspect –Ratio Urban Street Canyons with Wall Model," *Boundary-Layer Meteorology*, 129, pp 249-268, 2008.

12. Bottema, M. "Parameterisation of Aerodynamic Roughness Parameters in Relation with Air Pollutant Removal Efficiency of Streets," *Air Pollution Engineering and Management*, H. Power et al., Eds, Computational Mechanics, pp 235-242, 1995.

13. Bottema, M. "Urban roughness Modelling in Relation to Pollutant Dispersion," *Atmospheric Environment*, 31, pp 3059-3075, 1997.

14. Macdonald, R.W., Griffiths, R.F., and Hall, D.H. "An Improved Method for the Estimation of Surface Roughness of Obstacle Arrays," *Atmospheric Environment*, 32, pp 1857-1864, 1988.

15. Hamlyn, D., and Britter, R., "A Numertical Study of the Flow Field and Exchange Processes within a Canopy of Urban-Type Roughness," *Atmospheric Environment*, 39, pp 3243-3254, 2005.

16. Britter, R. E., and Di Sabatino, S. "Chapter 7 Flow through Urban Canopies," in *Handbook of Envionmental Fluid Dynamics Volume Two,* Fernando, H. J. S. Ed. CRC Press/Taylor & Francis Group, 2013.

17. Macdonald, R. “Modelling the Mean Velocity Profile in the Urban Canopy Layer,” *Boundary-Layer Meteorology,* 97, pp 25-45. 2000.

18. Cionco, R. M. “A Mathematical Model for Air Flow in a Vegetative Canopy,” *Journal of Applied Meteorology*, 4, pp517-522, 1965.

19. Fernando, H. J. S., Zajic, D., Di Sabatino, S., Dimitrova, R., Hedquist, B., and Dallman, A., “Flow, Turbulence , and Pollutant Dispersion in Urban Atmospheres,” *Physics of Fluids*, 22, 051301, 2010.

20. Kastner-Klein, P., and Rotach, M. W., “Mean Flow and Turbulence Characteristics in an Urban Roughness Sublayer,” *Boundary-Layer Meteorology*, 111, pp 58-84, 2004.

21. Christen, A., Vogt, R., and Rotach, M.W., “Profile Measurements of Selected Turbulence Parameters over Different Urban Surfaces,” *Preprint 4th International Conference on Urban Air Quality, Prague, March 25-27*, pp 408-411, 2003.

22. Bentham, T., and Britter, R. “ Spatially Averaged Flow within Obstacle Arrays,” *Atmospheric Environment*, 37, pp. 2037-2043. 2003.

23. Roth, M., “Review of Atmospheric Turbulence over Cities,” Quarterly Journal of the Royal Meteorological Society, 126, pp 941-990, 2000.

24. Louka, P., Belcher, S.E., and Harrison, R.G. “Coupling between air flow in street and the well-developed boundary layer aloft,” *Atmospheric Environment*, 34, pp 2613-2621, 2000.

25. Snyder, W.H., Davidson, M.J., and Lawson, R.E., Data Report: Building Array – Neutral Plumes. August 1991.

26. Kastner-Klein, P., Rotach, M., and Federovich E., “Experimental study on mean flow and

turbulence characteristics in an urban roughness sublayer," *14th Symp. Boundary Layer Turbulence*, American Meteorological Society, 2000.

27. Macdonald, R.W., Carter, S., and Slawson, P.R., "Measurements of mean velocity and turbulence statistics in simple obstacle arrays at 1:1200 scale," Thermal Fluids Report 2000-1, Department of Mechanical Engineering, University of Waterloo, 2000.

28. Lloyd, H., "Pollutant Dispersion in Urban Geometries – Turbulence within the Urban Canopy," Fourth-Year Project Report, University of Cambridge, 2004.

29. Li, X.-X., Liu, C.-H., and Leung, D. Y. C., "Large-Eddy Simulation of Flow and Pollutant Dispersion in High-Aspect-Ratio Urban Street Canyons with Wall Model," *Boundary-Layer Meteorology*, 129, pp 249-268, 2008.

30. Kastner-Klein, P., Berkowicz, R., and Britter, R., "The Influence of Street Architecture on Flow and Dispersion in Street Canyons," *Meteorology and Atmospheric physics*, 87, pp 121-121, 2004.

31. Brown, M.J., Khalsa, H., Nelson, M., and Boswell, D., "Street Canyon Flow Patterns in a Horizontal PlaneL Measurements from the Joint Urban 2003 Field Experiment," in *Proceedings of AMS Symposium on the Urban Environment*, Vancouver, B.C., 2004.

32. Balogun, A.A., Tomlin, A.S., Wood, C.R., Barlow, J.F., Belcher, S.E., Smalley, R.J., Lingard, J.J.N., Arnold, S.J., Dobre, A., Robins, A.G., Martin, D., and Shallcross, D.E., "In-street wind direction variability in the vicinity of a busy intersection in central London," *Boundary-layer Meteorology,* 136 pp 489-513, 2010.

33. Zajic, D., Fernando, J.S., Calhoun, R., Princevac, M., Brown, M.J., and Pardyjak, E.R., "Flow and Turbulence in an Urban Canyon," *Journal of Applied Meteorology and*

Climatology, 50, pp 203-223, 2011.

34. DePaul, F. T., and Sheih, C. M., “Measurements of Wind Velocities in a Street Canyon,” *Atmospheric Environment*, 20, pp 455-459, 1986.

35. Nakamura, Y., and Oke, T.R., “Wind, Temperature and Stability Conditions in an East-West Oriented Urban Canyon,” *Atmospheric Environment*, 22, pp 2691-2700, 1988.

36. Rotach, M.W., “Profiles of Turbulence Statistics in and above an Urban Street Canyon,” *Atmospheric Environment*, 29, pp 1473-1486, 1995.

37. Klein, P., and Clark, J.V., “Flow Variabitliy in a North American Downtown Street Canyon,” *Journal of Applied Meteorology and Climatology*, 46, pp 851-877, 2007.

38. Niachou, K., Livada, I., and Santamouris, M., “Experimental Study of Temperature and Airflow Distribution inside an Urban Street Canyon during Hot Summer Weather Conditions. Part II: Airflow Analysis,” *Building and Environment*, 43, pp 1393-1403, 2008.

39. Dallman, A., Magnusson, S., Britter, R., Norford, L, Entekhabi, D., and Fernando, H.J.S., “Conditions for Thermal Circulation in Urban Street Canyons,” *Building and Environment*, 80, pp 184-191, 2014.

40. ASHRAE. “Chapter 16 Ventilation and Infiltration,” in *2009 ASHRAE Handbook—Fundamentals (SI),* pp 16.7, 2009.

41. Etheridge, D.W., and Sandberg, M., *Building Vetilation: Theory and Measurement*. John Wiley and Sons Chichester, 1996.

42. ASHRAE. “Chapter 24 Airflow around Buildings,” in *2009 ASHRAE Handbook—*

Fundamentals (SI), 2009, pp. 24.1.

43. Bu, Z., and Kato, S., “Investigation of Ventilation Effectiveness for Wind-Driven Single-Sided Ventilated Buildings Located in an Urban Environment,” *International Jounal of Ventilation*, 10 No 1, pp 19-30, 2011.

44. Wang, H., and Chen, Q. “A New Emprirical Model for Predicting Single-Sided, Wind-Driven Natural Ventilation in Buildings,” *Energy and Buildings*, 54, pp386-394, 2012.

45. Larsen, T.S., and Heiselberg, P., “Single-Sided Natural Ventiation Driven by Wind Pressure and Temperature Difference,” *Energy and Buildings*, 40, pp 1031-1040, 2008.

46. Warren, P.R., and Parkins, L.M., “Single-Sided Ventilation through Open Windows,” *Proceedings ASHRAE SP 49*, pp 209-228, 1985.

47. Chu, C.R., Chen, R.H, and Chen, J.W., “A Laboratory Experiment of Shear-Induced Natural Ventilation,” *Energy and Buildings*, 43, pp 2631-2637, 2011.

Chapter 3 Methodology

3.1 Overview

There are generally three methods in urban airflow studies: field measurement, wind-tunnel experiment and numerical simulations. Each method has its pros and cons. The current study employed a field measurement to investigate the flow and the turbulence conditions around buildings. A case study was carried out in a representative residential building cluster in Singapore where sensors were installed at the pedestrian level and at several heights in the buildings to monitor flow and other weather variables. The observations from the field measurement provided valuable insights into the flow and turbulence patterns in a two-row building cluster. The outdoor ventilation potential of such a configuration was also revealed by the measurements. The indoor ventilation was studied by the numerical simulation because it has less physical constraints and allows easy manipulations of the test cases, although its reliability is not as good as the physical experiment.

3.2 Field Measurement

An outdoor airflow field measurement campaign was carried out in a high-rise residential building group in Singapore, in the northeast and southwest monsoon season. Sensors were installed to measure the mean flow and turbulence as well as such other variables as temperature and humidity. The reference airflow and other meteorological data measured by the standard meteorological station at the airport were also acquired.

3.2.1 Site Description

3.2.1.1 Singapore

The field measurement was conducted in the city of Singapore. Singapore (1.28°N 103.83°E) is a city state located in Southeast Asia with hot and humid tropical climate (annual average temperate = 27 °C; annual average relative humidity = 84.2% [1]). Two monsoon seasons influence the island, the northeast monsoon from December to March and the southwest monsoon from June to September. Singapore has a mild wind condition. The average surface wind speed falls within 1 m/s to 3 m/s [2].

Due to limited land area, Singapore adopts high-rise buildings for public housing. These buildings are commonly referred to as the *HDB*s because they are designed and constructed by the Housing and Development Board of Singapore. In 2013, 82% of the Singapore residents lived in *HDB*s [3]. The standard *HDB*s often have 10-16 stories and are in a diversity of forms. This study focused on a *HDB* cluster in a newly developed district, the Punggol New Town (Figure 3.1).

Figure 3.1 The landscape of the Punggol New Town, Singapore.

3.2.1.2 The Treelodge *HDB* Precinct

The selected high-rise residential building cluster for the field measurement is the Treelodge

HDB precinct (“Treelodge” in short) located in the northeast region of Singapore. The area to the immediate northeast of Treelodge is an undeveloped open terrain ($z_d \approx 0$) that stretches about 1.2 km until it reaches the Johor Strait. On the contrary, the immediate southwest of Treelodge is a span of 16-story high-rise buildings (Figure 3.2). The unique location of the site makes it the first row of the urban buildings during the northeast monsoon and the last row during the southwest monsoon, allowing the observation of two types of building-flow interactions. From the Google Map image, the plan area density of the Punggol area can be calculated, $\lambda_p \approx 0.24$. Assuming all the buildings have similar dimensions as the Treelodge building, i.e. $H = 2B$, and the monsoon wind direction is approximately perpendicular to the long dimension of the building (L), the frontal area density

$\lambda_f = (H \cdot L)/A_T = (2B \cdot L)/A_T = 2\lambda_p = 0.48.$

Figure 3.2 The location of the Treelodge and its surrounding environment.

The site consists of seven 16-story buildings arranged in two staggered rows with a longitudinal axis oriented at 120 degrees (Figure 3.3). The dimensions of a single building is roughly 50 m × 25 m × 50 m ($L \times B \times H$). The buildings rest on a podium about 5 m high and the ground level is made into a semi-sheltered car park. A walking deck for residents' activities, named the *eco-deck*, is built on top of the podium. It corresponds to the 2nd level of the buildings and is the pedestrian level in the current study.

Figure 3.3 The Treelodge plan view. Block numbers (e.g. 306A) – boxes with solid border; each gap between two buildings is labeled with an alphabet (e.g. A, B).

The spacing between two buildings on the same row (the *gap*) is small (~10m) compared to the distance between the two rows (~30m for the west half and ~50m for the east half) (Figure 3.3). In this sense, the Treelodge building group resembles a porous canyon, of which the height-to-width ratios are about 1.7 and 1. From this point onward, the spacing between the two rows of the buildings will be referred to as the *eco-deck canyon*. Table 3.1 summarizes the relevant dimensions of the Treelodge.

Table 3.1 Dimensions of Treelodge buildings, eco-deck canyon and the gaps.

Building Dimensions			**Gap Dimensions**	
	306A, B, C, D &305 D	305A & B	Gap	Width
Breadth *B*	26.2 m	26.2 m	A	11.0 m
Length *L*	54.1m	38.8 m	B	9.8 m
Height *H*	50.0 m	50.0 m	C	11.5 m
Eco-deck Canyon Dimension			D	21.5 m
Width *W*	Narrow: 30.1 m; Wide: 54.0 m		E	5.0 m

3.2.2 Instrumentation

Ten Vaisala WXT520 Weather Transmitters were used in the field measurements (Figure 3.4). They are integrated weather stations capable of measuring wind speed and direction, ambient pressure, temperature, humidity and precipitation [4]. The 2D wind speed and direction are sampled by the ultrasonic anemometer at 4 Hz and reported as one-second averages. The resolution of wind speed is 0.1 m/s and the direction is reported in 0°-359° with resolution of 1°. The unit that measures pressure, temperature and relative humidity at 1min interval resides in the radiation shield. The top “steel plate” is the piezoelectric precipitation sensor, activated only in rainfall events. Each sensor is paired with a 12V - 35Ah battery and a single-board computer the “*gumstix*” that logs data into an SD card. The data are downloaded manually at the end of each experimental period and post-processed offline.

Figure 3.4 Vaisala WXT520 weather transmitter.

3.2.3 Measurement Procedures

Two measurement campaigns were conducted, first in the northeast (NE) monsoon season (February – March 2012) and later in the southwest (SW) monsoon season (August - September 2012). Each campaign was divided into two phases.

3.2.3.1 NE monsoon

In the northeast monsoon phase I (NE Phase I), nine weather stations were deployed on the eco-deck (Figure 3.5, Stations 1 – 9) and one on the rooftop of Block 306C as the reference station (Figure 3.5, Station *rf*). Station 1 and 2 were located in the gaps between Block 305D and Block 306D, and the gap between Block 306D and Block 306C, respectively. Station 9 was installed next to the Punggol Road. The rest of the stations were situated along the eco-deck spine. Two types of sensor installation techniques were adopted. Sensors 1, 2 and 8 were mounted on 3 m metal poles that were clamped to the railings. Guide wires were used to stabilize the poles (Figure 3.6a). The other sensors were attached to short poles and then fixed on top of the wooden trellis that goes along the eco-deck (Figure 3.6b). They were kept at the same height as the sensors on the poles.

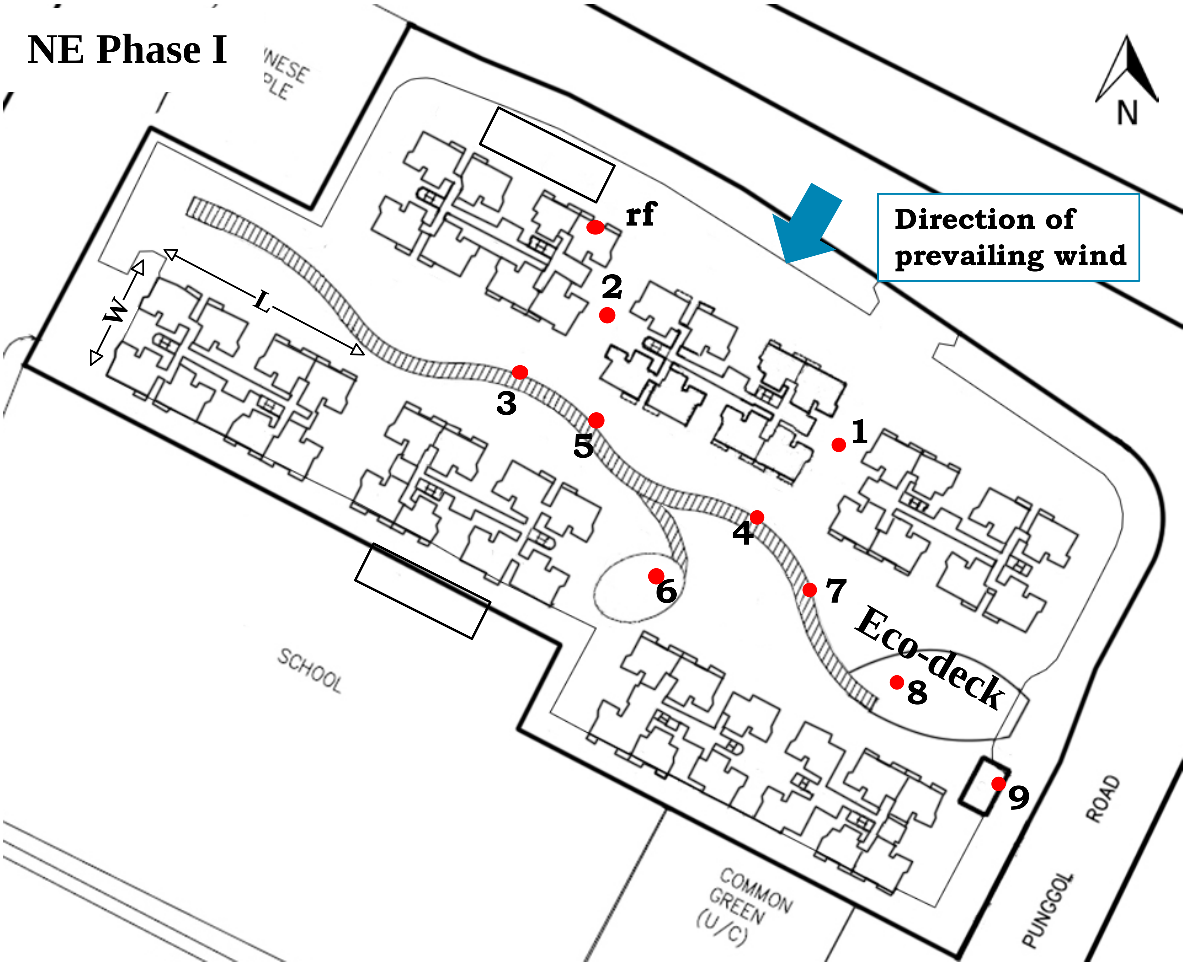

Figure 3.5 Site plan of the Treelodge and sensor layout in NE Phase I measurement. Station *rf* is on the roof of Block 306C. Stations 1 – 9 are on the eco-deck level.

The height requirements of a roof reference station have been suggested to be at least the building height or the maximum horizontal dimension of the roof [5]. For a high-rise building, it is impossible to meet those criteria. Moreover, the Treelodge buildings are under strict Air Force building height control. Therefore, the rooftop sensor could only go up to 2 m (Figure 3.6c). It was installed at the upwind building edge. NE Phase I was conducted from 24 Feb 2012 to 1 Mar 2012.

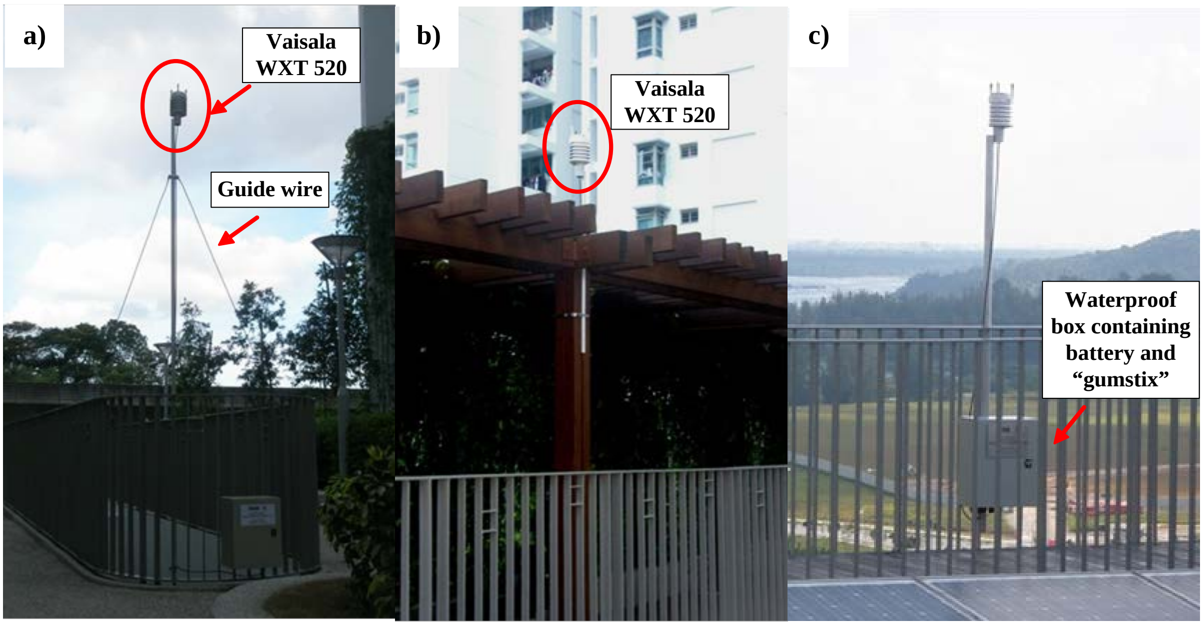

Figure 3.6 a) The Vaisala station installed on the pole; b) the Vaisala station installed on the trellis; and c) the Vaisala station installed on the roof.

Due to warm weather, *HDB* buildings in Singapore have large openings on the corridor walls for airflow to pass through. In the second phase of each of the two study periods, sensors were moved to these locations to gauge the airflow through the buildings. In the northeast monsoon phase II (NE Phase II) (Figure 3.7), only three sensors were left on the eco-deck, Stations 1 – 3, deployed in the same manners as Phase I. Stations 4 – 6 were installed at the north-side corridor openings Block 306C on the 3rd, 9th and 15th level respectively (Figure 3.8 a, b). The Vaisala sensor head was kept as far from all the walls as possible. Meanwhile, the concern of instrument security required that the Vaisala should be higher than the height of an average adult male. As a result, for Stations 4 – 6, the sensor was placed where the ultrasonic anemometer was 148 cm from the west wall, 158cm from the east wall, 38 cm from the ceiling and 190 cm from the floor. The wind velocities at the corresponding locations in the downwind building Block 306B were also measured. Stations 7 – 9 were shifted to the 3rd, 9th and 15th level of Block 306B (Figure 3.8 a, c). The residential units layout of Block 306B is the same as Block 306C, but rotated 180°, so the north-side corridor opening suitable for sensor installation became the one indicated in Figure 3.8 a. For sensors in Block 306B, the ultrasonic head was 98 cm from the west wall, 409 cm from the east wall, 38 cm from the ceiling and 190 cm from the floor. The roof station was not changed. NE Phase II was conducted from 14 Mar 2012 to 19 Mar 2012.

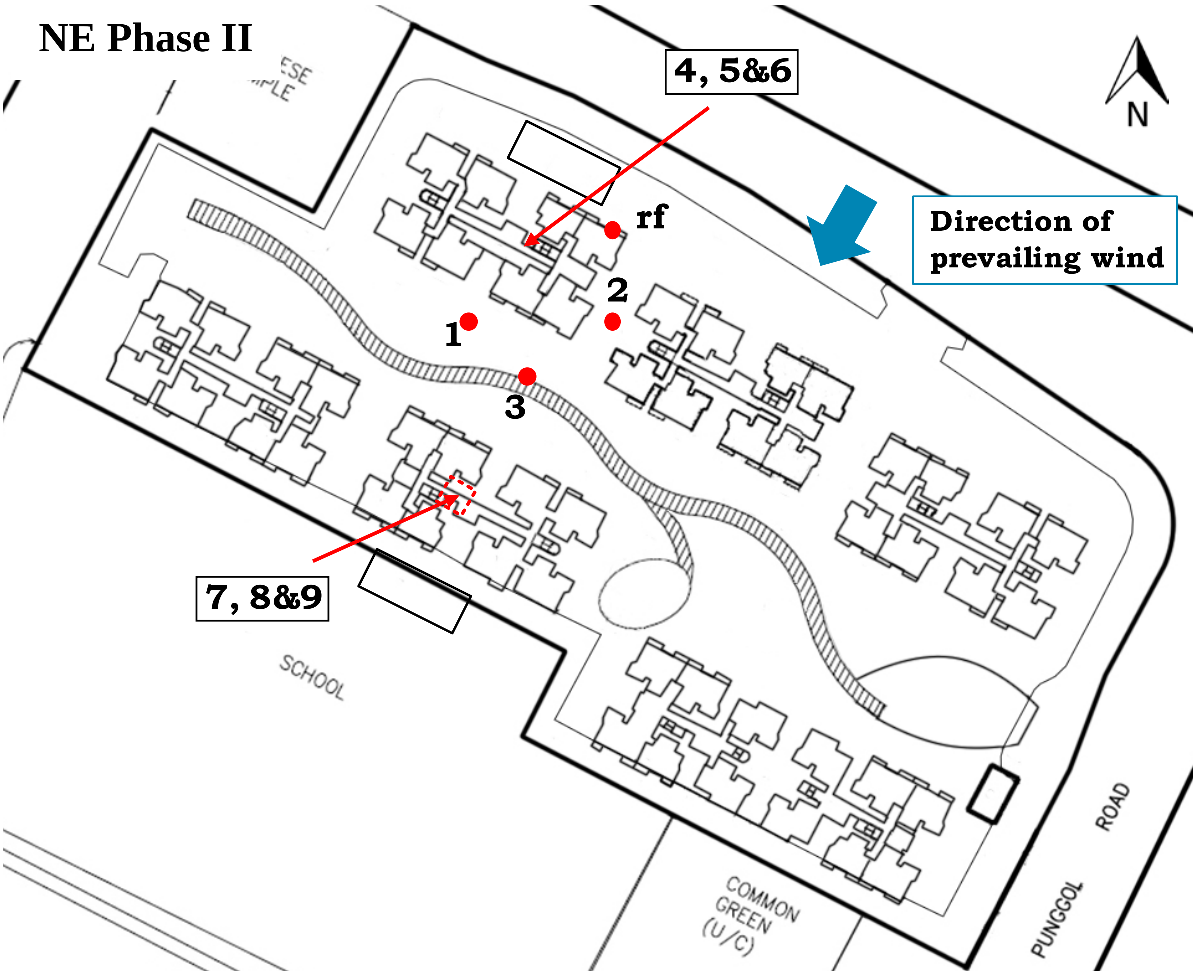

Figure 3.7 Sensor layout in NE Phase II measurement. The Station *rf* is on the roof of Block 306C. Stations 1 – 3 are on the eco-deck level. Stations 4 – 6 are installed at the 3rd, 9th and 15th floor of Block 306C respectively. Stations 7 – 9 are installed at the 3rd, 9th and 15th floor of Block 306B respectively.

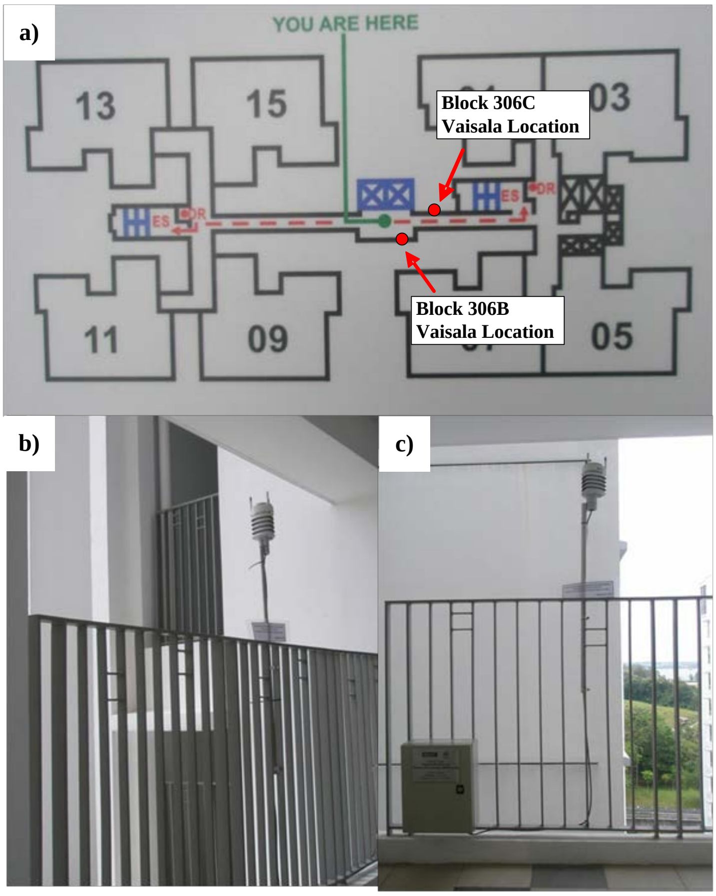

Figure 3.8 a) Floor plan of Block 306C and Block 306B; b) The Vaisala installed at the Block 306C corridor opening; and c) The Vaisala installed at the Block 306B corridor opening.

3.2.3.2 SW monsoon

The southwest monsoon season measurement campaign was designed in a similar way as the northeast monsoon. The reference station was installed on the rooftop of Block 306B in a similar manner. In the southwest monsoon phase I (SW Phase I), seven sensors were installed at 3 m on the eco-deck (Figure 3.9) either on poles or above the trellis similar to NE Phase I. In the southwest monsoon phase II (SW Phase II), sensors were again installed in the buildings, but were mounted on the south-side corridor openings of Block 306C and Block 306B on the 3rd, 9th and 15th floors (Figure 3.10). SW Phase I was conducted from 21 Aug 2012 to 26 Aug 2012, and SW Phase II from 28 Aug 2012 to 2 Sep 2012.

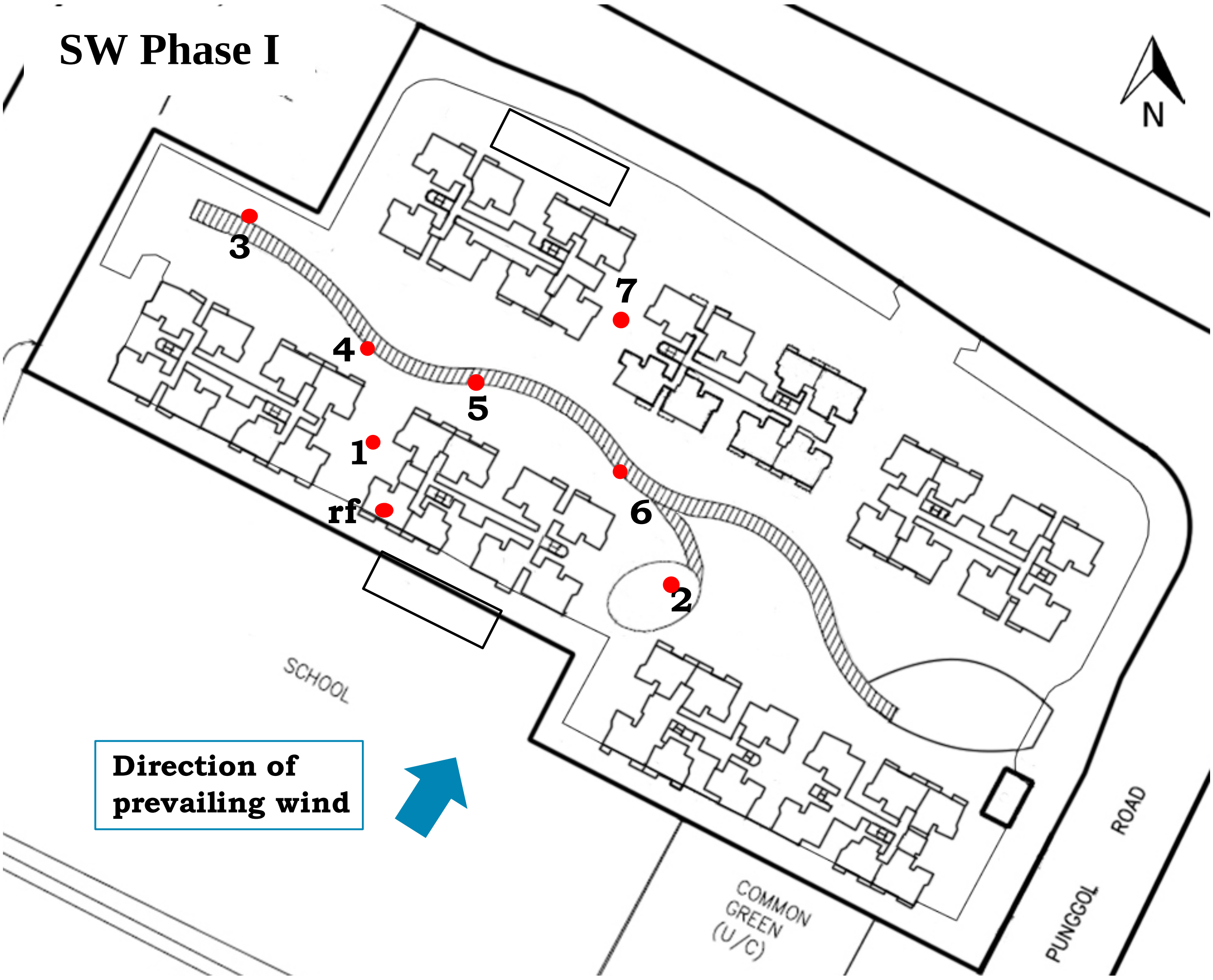

Figure 3.9 Sensor layout in SW Phase I measurement. The station *rf* is on the roof of Block 306B. Stations 1 – 7 are on the eco-deck level.

A long-term standard meteorological station is available at the Changi airport on the east end of the Singapore Island about 10 km southwest of the Treelodge site. The meteorological station records one-minute horizontal wind speed and direction at 15 m above ground. The wind data at this station during the field measurement period were obtained for the analysis.

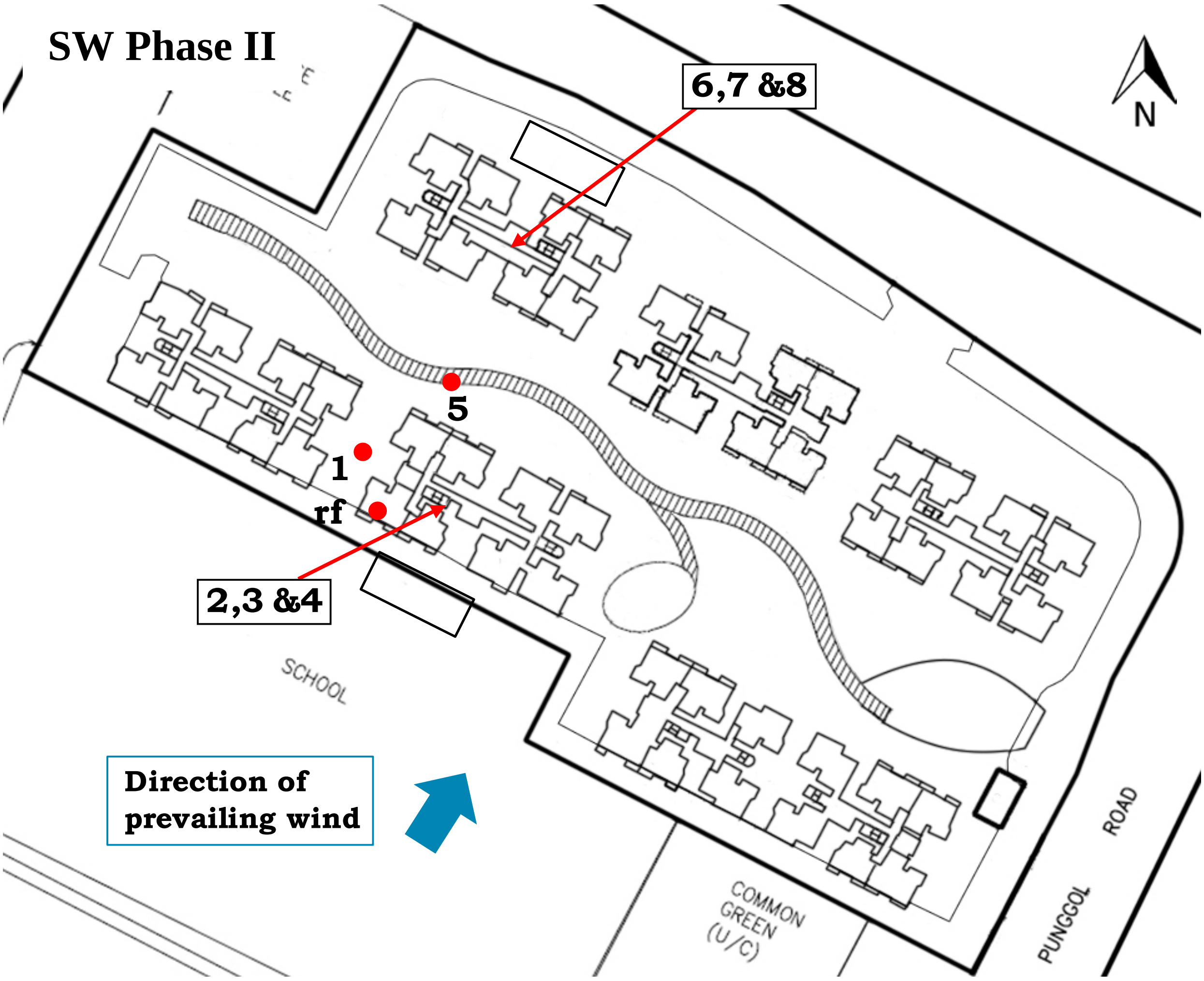

Figure 3.10 Sensor layout in SW Phase II measurement. The station *rf* is on the roof of Block 306B. Station 1and 5 are on the eco-deck level. Stations 2 – 4 are installed at the 3rd, 9th and 15th floor of Block 306B respectively. Stations 6 – 8 are installed at the 3rd, 9th and 15th floor of Block 306C respectively.

3.3 CFD Modeling

The single-sided ventilation of a building was investigated with CFD simulations that were computed using ANSYS FLUENT 13.0. Computational fluid dynamics (CFD) modeling resolves the flow field by solving the Navier-Stokes equations at finite grid points. Different methods are available with different calculation loads and for different purposes, including direct numerical simulation (DNS), large-eddy simulation (LES) and Reynolds-averaged Navier-Stokes (RANS) simulation [6]. Since in the current study the ventilation rate is of interest, a steady-state solution is sufficient. As a result, the RANS model was chosen, because it is time-saving and has acceptable accuracy in ventilation rate estimation [7]. The k-ε turbulence model was used, which is suitable for simulating flow that is far from the wall [8]. Its known overestimation of the separation zone is not very important for simulating indoor airflow [9]. The Semi-Implicit Method for Pressure-Linked Equations (SIMPLE) algorithm and second-order discretization schemes were applied. A volume source was input into the simulation, thus a passive species transport equation was solved together with the momentum equation. Chapter 5 will elaborate more details of the simulation, including validation processes and test cases.

Reference

1. National Environmental Agency, “Weather Statistics,” http://app2.nea.gov.sg/weather-climate/climate-information/weather-statistics, 07 Nov 2014, [11 Nov 2014].

2. National Environmental Agency, “Guide to Singapore’s Weather,” Nantional Environmental Agency of Singapore, 26 Mar 2007 [11 Nov 2014].

3. Housing and Development Board, “Key Statistics,” HDB Annual Report 2012/2013, Housing and Development Board of Singapore, 2013.

4. Vaisala, *Vaisala WXT520 Weather Transmitter User’s Guide*, Helsinki Finland: Vaisala Oyi, 2010.

5. World Meteorological Organization. “WMO Guide to Meteorological Instruments and Methods of Observation, Part II Observing Systems, Chapter 11 Urban Observation,” Internet:ftp://ftp.wmo.int/Documents/MediaPublic/Publications/WMO8_CIMOguide/WMO8_Ed2008_Up2010_en.pdf. Aug 2008 [11 Nov 2014].

6. Versteeg, H.K., and Malalasekera, W., *An Introduction to Computational Fluid Dynamics, the Finite Volume Method* 2^{nd} *ed.*, Edinburgh: Pearson Education Limited, 2007.

7. Buccolieri, R., Sandberg, M., and Di Sabatino, S., “City Breathability and its Link to Pollutant concentration Distribution winthin Urban-like Geometries,” *Atmospheric Environment*, vol 44, pp 1894-1903, 2010.

8. ANSYS, Inc. “ANSYS FLUENT User’s Guide,” ANSYS, Inc, Nov 2010, Release 13,0.

9. Franke, J., Hellsten, A., Schlunzen, H., and Carissimo, B. “Best practice guideline for the CFD simulation of ows in the urban environment,” COST Action 732: Quality assurance

and improvement of microscale meteorological models. Technical report, COST Office, May 2007.

Chapter 4 Mean Flow and Turbulence and Prediction of Pedestrian Level Ventilation Potentials

4.1 Overview

4.1.1 Chapter Overview

In this chapter, the flow and turbulence patterns around a high-rise residential building cluster are derived from the observations from the field measurement. The collected raw data are quality-checked and those do not meet the criteria are removed. The diurnal temperature variations are reported and the atmospheric stability conditions are found to be unstable in the majority of the time. Afterwards, the roof reference wind speed and direction are investigated and compared to the airport reference station. The roof station proves to be able to provide valid reference wind information for the analysis. The wind speed and flow pattern on the pedestrian level are analyzed with respect to different roof wind direction in the next subsection. The canyon-to-roof wind speed ratio of 0.4 appears to hold when the angle between the incoming wind and the normal of the canyon, i.e. angle of attack, is less than 60°. When the angle of attack is larger than 60°, airflow tends to channel along the canyon. The vertical wind profiles at the upwind buildings and the downwind buildings are presented after that. Nearly constant wind speed profiles are observed in the downwind buildings in both seasons. Turbulence statistics on the roof and in the canyon are assessed subsequently. The roof turbulence level turns out to be a better scale than the roof wind speed for the turbulence in the canyon. Furthermore, the normalized turbulence is highly spatially and temporally uniform in the canyon. Last but not least, the measurement results are summarized to predict the ventilation potential at the pedestrian level of the Treelodge canyon, with ready-to-use coefficients proposed.

4.1.2 Data Quality Check and Processing

Before and after each measurement, every weather station was put through the zero-wind check as recommended by the manufacturer (private communication), i.e. shielding the Vaisala sensor from the wind with a box: if the sensor outputs zero wind speed, it functions normally. It turned out that Station 1 and Station 4 in the NE monsoon measurements were malfunctioning. Therefore, data from Station 4 in both NE measurement phases and data from Station 1 in the NE Phase II were discarded. Afterwards, the missing data percentage was checked. For one-second wind data, no station had more than 0.1% missing data, and no missing data were found in temperature, humidity and pressure. Table 4.1 summarizes the data used for analysis from each measurement phase.

Table 4.1 Valid stations and duration for each measurement phase.

	Stations No.	**Durations**
NE Phase I	1-3, 5-9, rf	Feb 24, 15:00 – Mar 01, 20:00, 2012
NE Phase II	2-3, 5-9, rf	Mar 14, 21:00 – Mar 19 20:00, 2012
SW Phase I	1-7, rf	Aug 21, 12:00 – Aug 26, 16:00, 2012
SW Phase II	1-8, rf	Aug 28, 13:00 – Sep 02, 21:00, 2012

The Vaisala weather stations report horizontal wind speed magnitude U and horizontal wind direction θ, from which wind velocity vectors can be derived. Like previous studies [1-2], the local building coordinate is used, where the u-component is perpendicular to the long facades of the buildings 30° from the true north, and the v-component is aligned with the canyon.

Reynolds decomposition was performed on velocity vectors based on a 10-min averaging time, producing mean velocities $\bar{u}$, $\bar{v}$ and turbulent velocities u', v'. The 10-min average scalar wind speed is then calculated as $\sqrt{\bar{u}^2 + \bar{v}^2}$ and denoted by $\bar{U}$. It should be noted that this 10-min average scalar wind speed $\bar{U}$ is the variable used for analysis in most of this report, not the velocity components $\bar{u}$, $\bar{v}$. The 10-min average wind direction $\bar{\theta}$ is obtained by applying the inverse tangent function to the 10-min average velocity components ratio $\bar{u}/\bar{v}$. The handling of turbulent velocities will be presented in the Section 4.6. Temperature data are also averaged at 10-min interval.

Nakamura and Oke [3] have pointed out that for a street canyon the coupling between the wind aloft and the secondary flow in the canyon is lost below some threshold wind speed, which suggests that the correlation between the wind above the roof and the wind in the canyon would be insignificant at very low wind speed. The current analysis concerns mainly the local flow induced by the background flow. Hence, the low-wind scenario where the connection between the ground flow and the roof flow is lost does not fit the purpose of the study. As a result, the low-wind conditions are meant to be excluded. Careful inspection indicates that the 10-min average roof wind speed $\overline{U_{rf}}$ of 0.2 m/s would be a proper cut-off wind speed. Therefore, all timestamps with 10-min average roof wind speed $\overline{U_{rf}} < 0.2$ m/s are excluded in the current analysis. The total removed timestamps are less than 0.1% of the total data.

4.2 Temperature Variations and Stability

Singapore does not experience a large temperature variation over the year. This is well reflected in the temperature measurements at the Treelodge. Similar maximum (32.3°C – 33.9°C), minimum (23.3°C – 24.0°C) and diurnal mean (27.1°C – 28.0°C) temperature are found in February/March and August/September (Table 4.2).

Table 4.2 Diurnal mean, maximum and minimum temperature at the Treelodge during the measurement periods.

	Diurnal Mean [°C]	**Maximum [°C]**	**Minimum [°C]**
NE Phase I (Feb – Mar)	27.9	33.9	24.0
NE Phase II (Feb – Mar)	27.1	32.3	23.4
SW Phase I (Aug – Sep)	28.0	33.4	23.3
SW Phase II (Aug – Sep)	27.5	33.1	23.7

The average sunny-day diurnal cycles of air temperature at the roof and in the canyon, as well as the temperature difference between them for each monsoon season are shown in Figure 4.1. The roof temperature is the temperature measured by the roof station at 2 m above the building. The canyon temperature is the average temperature over all valid canyon stations. In daytime (10:00 – 16:00), the canyon air is warmer than the air above the roof by 1 °C at maximum in both NE and SW monsoon seasons. This observation is in general agreement with the previous study by Nakamura and Oke [3] in an east-west oriented canyon, who reported warmer canyon air during the day by less than 1 °C. Rotach [4] also reported consistently higher canyon air temperature based on 18-month average data.

The elevated canyon air temperature is related to the solar heating of the canyon ground and the building surfaces. In midday the surface receiving direct solar irradiance can be 10 °C warmer than the air [3], releasing heat through convenction and radiation to the canyon air. The solar power in the two measurement seasons was approximately the same, because both measurements were conducted within one month to the equinox and Singapore is 1°N. This explains the similarity between NE and SW canyon-roof temperature differences.

During the night the canyon temperature is about 0.5 °C higher than the roof temperature in the NE monsoon, but is nearly equal to the roof temperature in the SW monsoon. One hypothesis is that the canyon temperature is higher than the roof only at nights of sunny days. Therefore, in the SW monsoon measurement temperature differences appear in the night following the sunny day (20:00 – 24:00) but not in the night before (00:00 – 08:00) because the day before the chosen SW monsoon sunny day was always cloudy or rainy (Figure 4.1b).

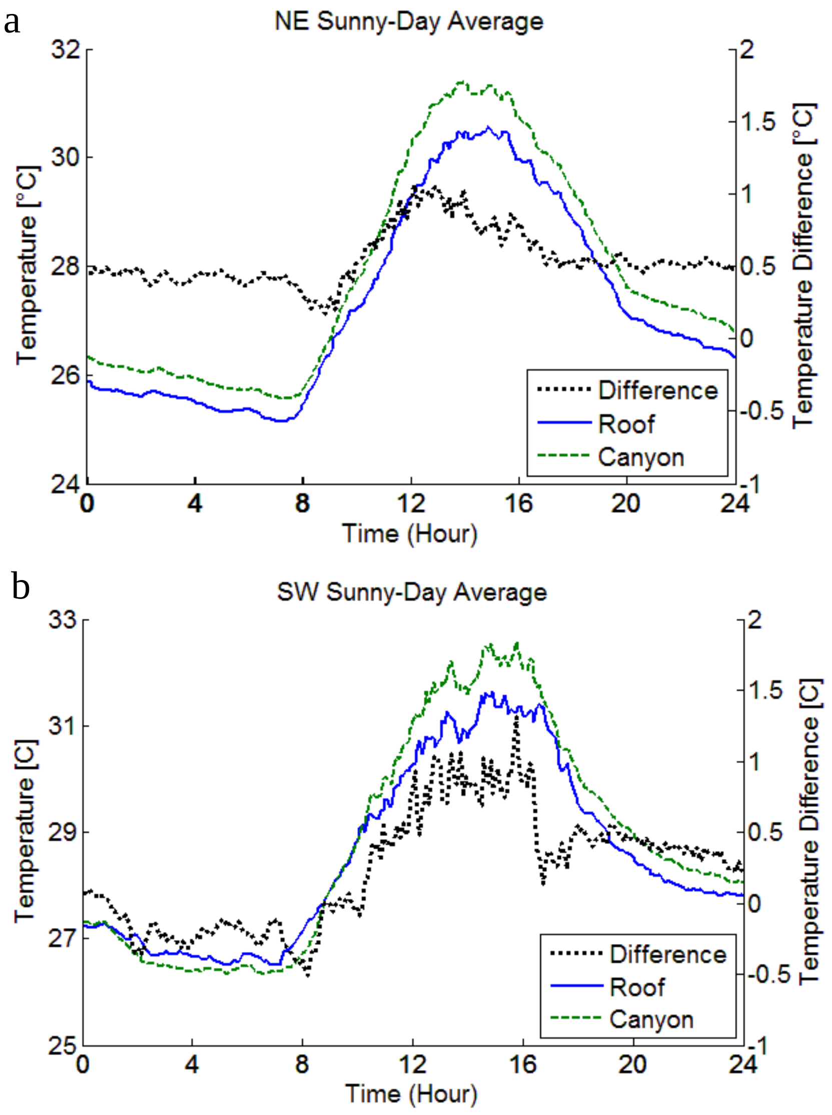

Figure 4.1 Average sunny-day diurnal cycle of air temperature days in a. the NE monsoon, and b. the SW monsoon. Solid blue line – temperature measured by the roof station; dashed line – average canyon temperature over all valid canyon stations; dotted line – temperature difference, positive meaning canyon temperature is higher than the roof temperature.

The fact that the near-ground temperature in the canyon is higher than the roof temperature suggests that the air in the canyon is unstable. The bulk Richardson number R_b could be used to indicate the stability condition [5].

$$R_b = gH\frac{T_H - T_0}{(T_a+273){U_H}^2}. \tag{4.1}$$

where T_0 is the surface temperature of the canyon ground, T_H is the temperature at the roof and T_a is the ambient air temperature. All temperature is in degree Celsius. U_H is the wind speed at the roof. H is the building height. g is the gravitational acceleration.

The bulk Richardson number represents the ratio of the square of the vertical airflow velocity scale resulted from buoyancy ($gH\frac{T_H - T_0}{(T_a+273)}$) to the square of the airflow velocity scale of the horizontal wind (${U_H}^2$). The original formula expressing the scale of the airflow velocity created by buoyancy is

$${u_B}^2 \sim gH\frac{\Delta\rho}{\rho}. \tag{4.2}$$

Substituting ideal gas law P = ρRT into the above relationship, assuming constant pressure, Equation (4.2) becomes

$${u_B}^2 \sim gH\frac{T}{\Delta T}. \tag{4.3}$$

Thus,

$$R_b = \frac{{u_B}^2}{{u_H}^2} = gH\frac{\Delta T}{T{U_H}^2} = gH\frac{T_H - T_0}{(T_a+273){U_H}^2}. \tag{4.1}$$

When the ground temperature is higher than the roof air temperature, the temperature difference $T_H - T_0$ is negative. The sign of R_b is also negative, indicating unstable condition. On the other hand, a positive R_b indicates stable condition. When the buoyancy velocity scale

u_B is larger than the horizontal velocity scale u_H, the magnitude of R_b is larger. In other words, the magnitude of R_b indicates the strength of stability or instability.

In the Treelodge measurement, the surface temperature of the canyon ground is not measured, thus T_0 is substituted by the near-ground canyon air temperature. The temperature measured by the roof station is used as T_H and the canyon air temperature is used as T_a.

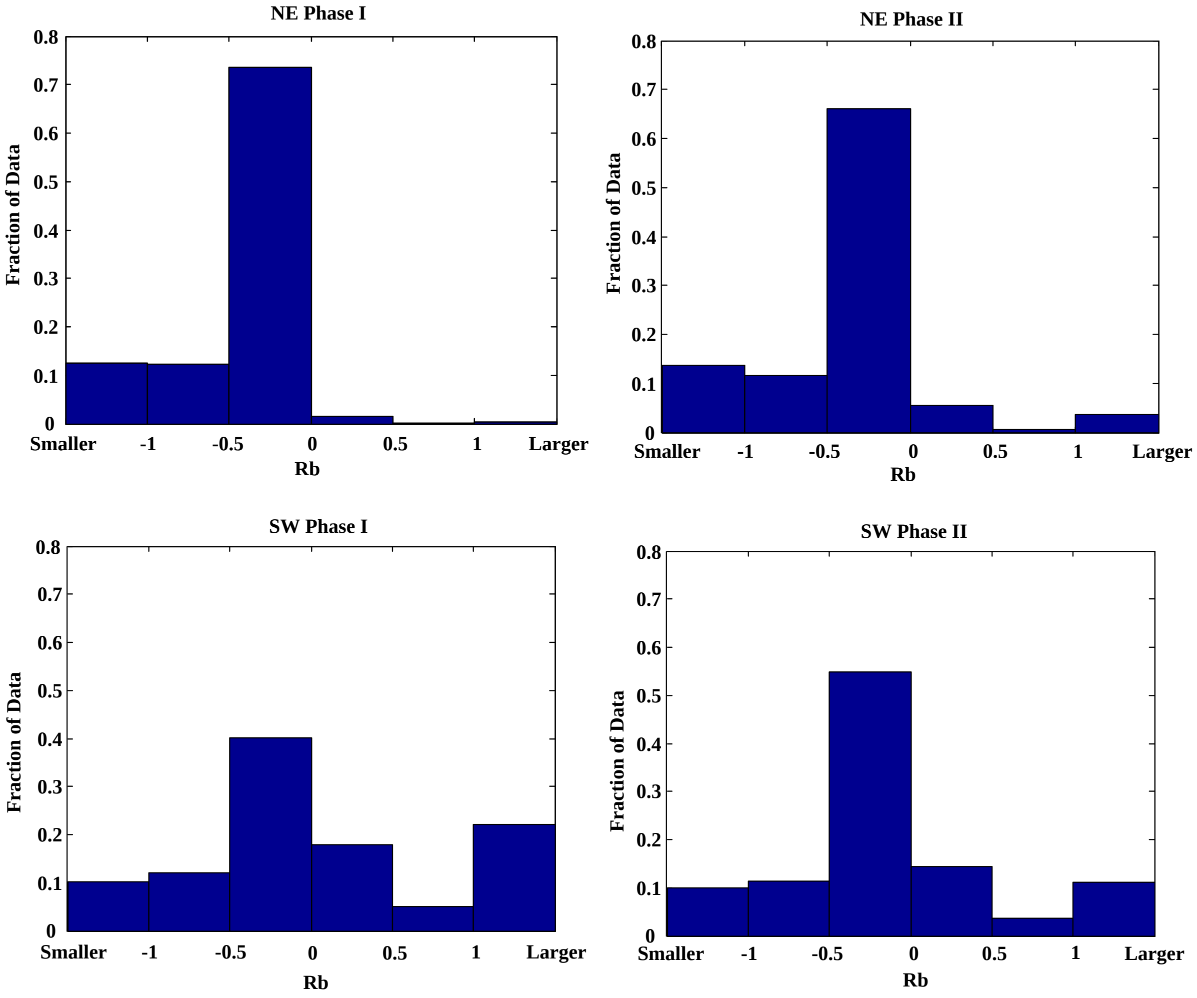

Figure 4.2 Distribution of the bulk Richardson number in each measurement phases.

Since both temperature and wind speed are presented in the form of 10min average, the bulk Richardson number at each 10 min interval is calculated and its distribution is shown in Figure 4.2. In all the measurements the highest frequency falls within -0.5 < R_b < 0. Unstable conditions were observed in the NE monsoon the majority of the time, whereas in the SW monsoon measurements the frequency of unstable conditions was reduced but still outnumbered the stable condition. Niachou et al. [5] found 21 percentage point reduction of unstable conditions (from 85% to 64%) at night compared to that during the day. However, the current measurements do not show the same result (Figure 4.3). In NE Phase II and SW Phase I, slight increase in the occurrence of the stable condition was observed but no more than 9 percentage points, whereas in the other two measurements, the same or even more unstable cases were found.

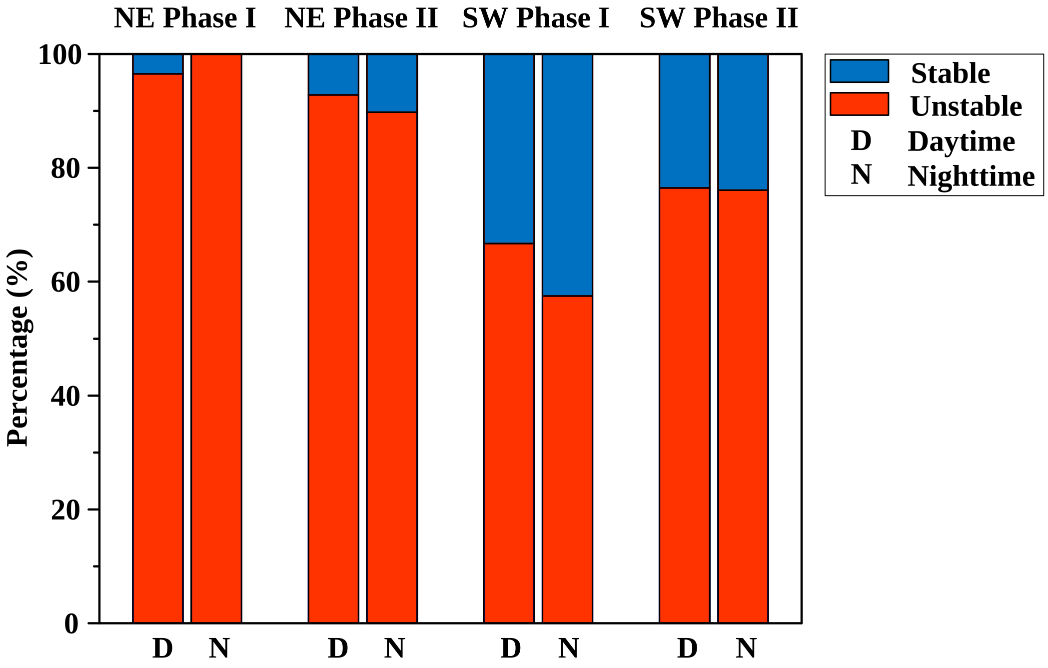

Figure 4.3 Percentage of stable and unstable condition during the daytime and the nighttime in each measurement phase.

4.3 Flow at Roof Reference Station and Flow at the Airport Reference Station

The Vaisala weather station set up on the roof is intended to provide local reference wind speed and direction. Ideally, the local-scale wind speed and direction should be measured in the inertial sublayer to be free from the disturbance of buildings as discussed in Section 2.1.

The World Meteorological Organization suggests a minimum requirement of 1.5 times the average building height for reference sensors to be placed on the roof [6]. This criterion is hard to meet among high-rise buildings such as the Treelodge buildings. However, the influence of the building on the wind above its roof may not be as significant as perceived. It could also be argued that as long as the influence of the geometry of interest on the airflow at a measurement station is constant, that station could be used as a reference station for studying airflow associated with the geometry. Examples include the study at an intersection in London, where the reference station was placed on the roof of a 15.5 m building at 2.9 m high. Good agreement in wind direction was found between the roof-top station and the sonic measurements on a 190 m tower 1.5 km away [7]. In addition, in the MID05 study five stations were set up on the roofs of five skyscrapers in the Manhattan Midtown. The combined roof-top wind speed was shown to be a useful reference wind speed [8].

In the current field measurement, measures have been taken to minimize the influence of the buildings on the roof station. First of all, the reference station was put at the upwind edge of the upwind building according to the prevailing wind direction of the monsoons. That is why the reference station was on different buildings in different monsoon seasons. Second, only data obtained when the reference station was upwind of the Treelodge buildings were used in the analysis. In other words, in the NE monsoon, only observations with wind directions from 300° to 120° are considered, whereas only observations with wind directions from 120° to 300° are considered in the SW monsoon.

To present a holistic picture of the airflow at the rooftop reference station, the 10-min average wind speed and direction measured at the roof station during the entire NE Phase I and SW Phase I are shown in Figure 4.4 without direction filtering. (The NE Phase II and SW Phase II are similar to their Phase I results and are not shown.) For comparison, the simultaneous

10-min average wind speed and direction recorded at the Changi Airport standard meteorological station are also presented in Figure 4.4.

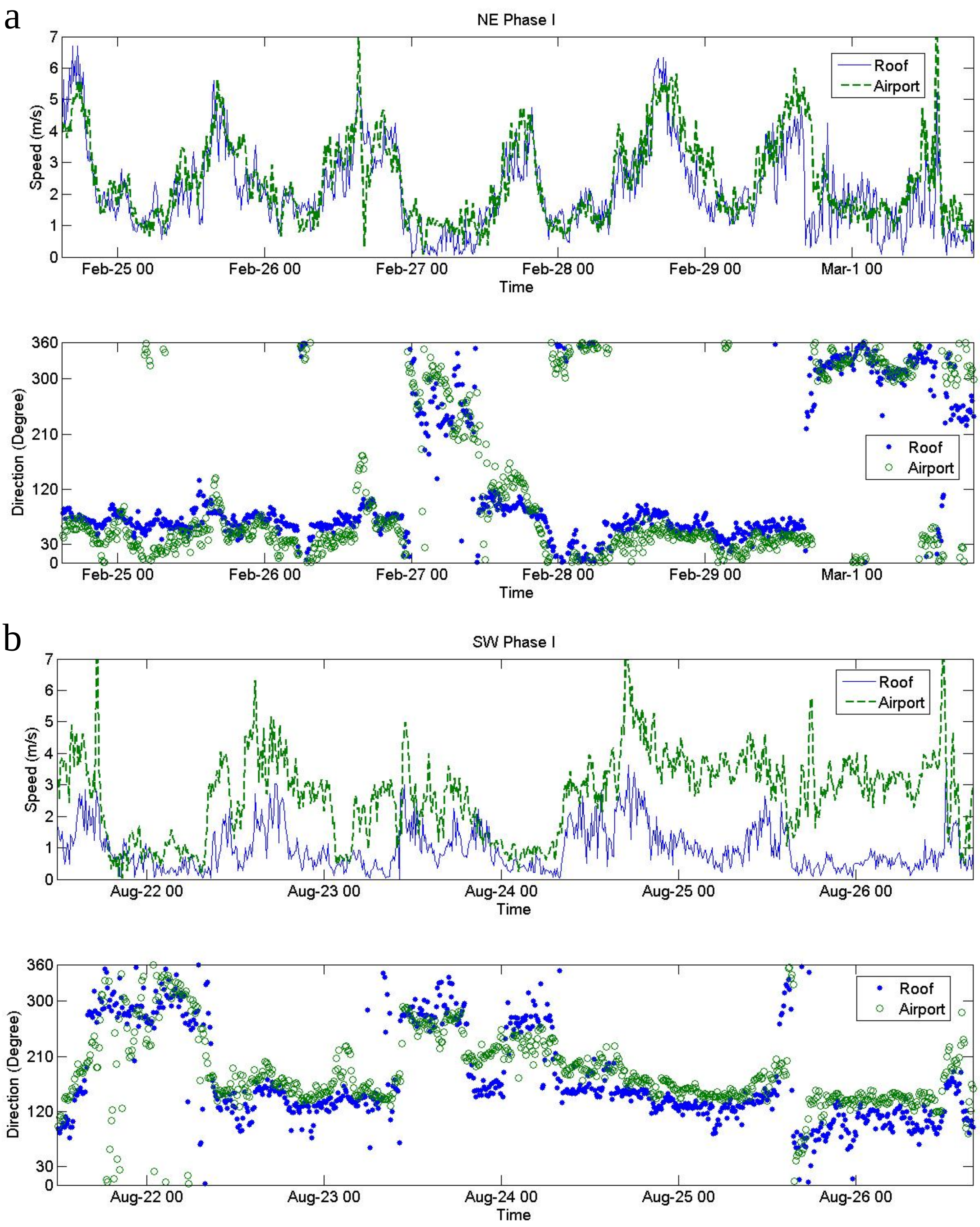

Figure 4.4 The wind speed and direction measured at the roof station and at the Changi station during a. NE Phase I, and b. SW Phase I.

In both seasons the monsoon wind direction predominates the observations ($\theta \in [30°, 90°]$ in NE Phase I and $\theta \in [120°, 210°]$ in SW Phase I). Consistent diurnal variations of wind speed are seen, especially for the NE Phase I, because most days and nights during the measurement period were clear. In contrast, in the SW Phase I it was cloudy or rainy. The strong monsoon wind that carried the cumulus clouds also resulted in elevated nighttime airport wind speed on, for example, Aug-25 and Aug-26 nights. The roof wind speed in the NE Phase I agrees very well with the airport wind speed, whereas in the SW Phase I the roof wind speed is about half of the airport wind speed. The roof wind directions are also similar to the airport wind directions, especially when the roof station is upwind of the site, i.e. around 60° in the NE Phase I and around 150° in the SW Phase I. The good agreements between the airport wind direction and the measured roof wind direction support the argument that the roof station could provide reference wind speed and direction when it is upwind of the Treelodge building group.

Observations with the desired roof wind direction were then selected and averaged over each measurement period (Table 4.3). For the NE monsoon, the roof wind speed is approximately equal to the airport wind speed. The average roof-to-airport wind speed ratios are close to unity and the standard deviations are less than half of the averages. For the SW monsoon, the roof wind speed is reduced by half compared to the airport wind speed and the standard deviations of the ratios are around 0.3. These observations are somewhat expected, because the wind from the northeast is unobstructed but the wind from the south have has passed over the built-up city area.

Given the low height of the sensor on the rooftop, which is subject to flow separation, good agreement between the roof and the airport wind directions were not expected. It is surprising to find that the wind direction differences between the roof and the airport stations are no more than 20.6° with standard deviation less than 38.4° for all measurements (Table 4.3). For the NE monsoon, the roof-minus-airport wind direction differences are positive, meaning the wind direction on the roof is more aligned with the buildings and the canyon. The negative wind direction differences for the SW monsoon suggest the same observation. This could probably be explained as the redirection of the oblique incoming flow by the (porous) canyon wall to be more parallel to the canyon.

Table 4.3 The comparison between wind speed and direction of the roof stations and the airport station.

	NE Phase I	NE Phase II	SW Phase I	SW Phase II
Total number of data points	797	594	501	580
Wind speed ratio, $U_{rf} / U_{airport}$	0.97	1.02	0.51	0.50
STD of $U_{rf} / U_{airport}$	0.37	0.51	0.32	0.30
Direction diff., $\theta_{rf} - \theta_{airport}$*[°]	14.8	4.4	-13.2	-20.6
STD of $\theta_{rf} - \theta_{airport}$ [°]	30.7	37.5	38.4	31.6
Daytime average U_{rf} [m/s]	2.58		1.57	
Nighttime average U_{rf} [m/s]	1.75		0.87	
Daytime average $U_{airport}$[m/s]	2.98		3.42	
Nighttime average $U_{airport}$ [m/s]	1.77		2.25	

*Direction differences are computed by subtracting directions measured at the airport from the directions measured at the roof.

The average daytime and nighttime wind speeds at the roof and the airport are also tabulated in Table 4.3. The average daytime roof wind speed in the NE monsoon is 2.58 m/s and the nighttime roof wind speed is 1.75 m/s. For the SW monsoon the average daytime roof wind speed is 1.57 m/s and the nighttime wind speed is 0.87 m/s. For residential buildings, nighttime ventilation is more critical because residents stay at home at night thus requiring thermal comfort, while at the same time producing more anthropogenic heat. The reduced nighttime wind speed suggests that other forms of ventilation such as stack effect or mechanical ventilation might be more effective.

4.4 Mean Flow on the Pedestrian Level

The eco-deck level wind speed is important because it directly affects the thermal comfort of the pedestrians and the ventilation of the space. The wind speed at a specific point on the eco-deck depends on three factors, the wind speed of the incoming flow U_0, the direction of the incoming flow θ_0 and its position on the eco-deck.

$$U_{eco-deck} = f(U_0, \theta_0, x, y). \tag{4.4}$$

In the current study, the incoming wind speed can be represented by the roof wind speed U_{rf} and the incoming wind direction can be estimated by the roof wind direction θ_{rf}, thus Equation (4.4) can be rewritten as

$$\frac{U_{eco-deck}}{U_{rf}} = f(\theta_{rf}, x, y). \tag{4.5}$$

Equation (4.5) defines a ground-to-roof wind speed ratio, which has also been used in other pedestrian airflow studies [9-10]. It reflects what fraction of the total wind resources is available on the ground. The ground flow was measured mainly in NE Phase I and SW Phase I. The rest of this section will analyze the wind speed ratios obtained in these two measurements, firstly with respect to the incoming wind directions, and then compared across stations.

In NE Phase I, the wind came from the northeast-east ($\theta_{rf} \in [45°, 90°]$) the majority of the time (Figure 4.5a). In SW Phase I, however, southeast wind ($\theta_{rf} \in [120°, 165°]$) dominated (Figure 4.5b). The data are separated into twenty-four direction sectors of 15 degrees according to the roof wind direction. The wind speed ratios at each station are then averaged within each direction sector to produce Figure 4.6 and Figure 4.8.

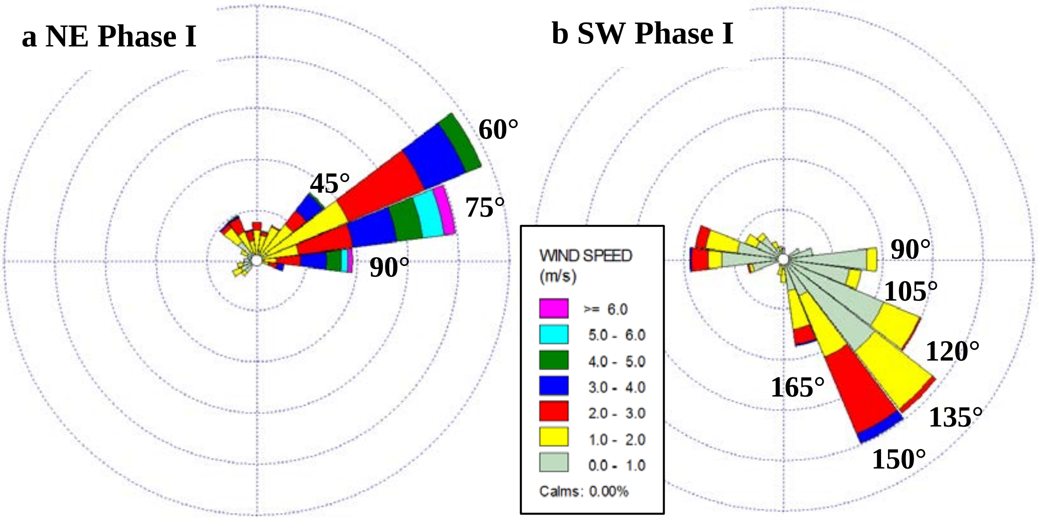

Figure 4.5 Wind rose of the roof station in a) NE Phase I, and b) SW Phase I. Each wind direction sector covers 15 degrees. The frequency determines the length of the wind rose petal. The direction sector is represented by its mid-value.

4.4.1 NE Monsoon Season

The timestamps at which the 10-min-average roof wind direction is between 45°and 90° in the NE Phase I measurement are selected out for the analysis. They are categorized into intervals of 15 degrees according to the roof direction and plotted in Figure 4.6. The two solid lines represent the two stations in the gap, Station 1 and Station 2 (station locations refer to Figure 4.7a). At $\theta_{rf} = 45°$ and $\theta_{rf} = 60°$, the wind speed of both stations is higher than the roof wind speed ($U_{st1}/U_{rf} > 1$ and $U_{st2}/U_{rf} > 1$), which is not observed at any other wind angles at any other stations. When the wind angle increases beyond θ_{rf} = 60°, the wind speed ratios in the gap decrease as the wind becomes more oblique. The observations comply with the predicted flow patterns. When the wind is more or less aligned with the gap (gap centerline = 30°), streamlines enter the gap easily and the contraction of the flow path could result in an increase in wind speed. When the wind is too oblique beyond some critical angle, flow separation takes place at the building corner and the gap is under the influence of the wake at least partially, leading to the decrease of wind speed. The critical angle in this measurement is around 30°, i.e. θ_{rf} = 60°.

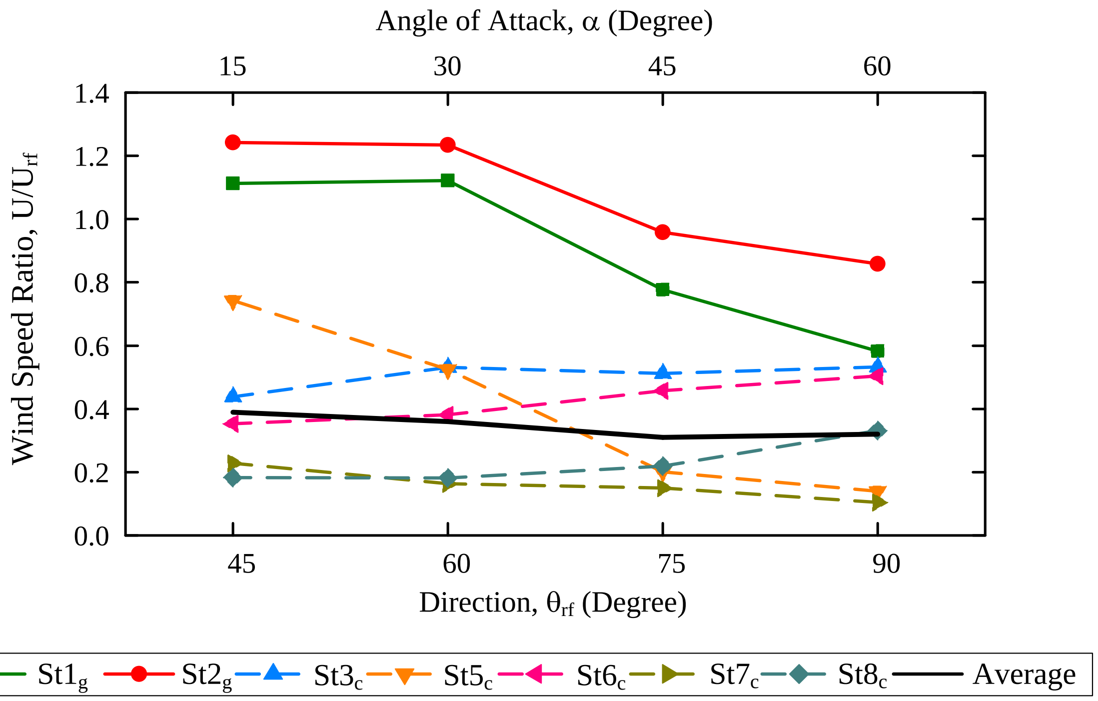

Figure 4.6 Wind speed ratio of each station on the eco-deck at four different prevailing wind angles during NE Phase I measurement. Solid line – gap stations; dotted line – canyon stations; bold black line – average of all canyon stations.

The wind speed of the eco-deck canyon stations (Station 3 – Station 8) does not vary significantly with the wind directions except for Station 5 (Figure 4.6). Station 3 and Station

6 demonstrate relatively higher wind speed ratios between 0.4 – 0.5 over all directions, whereas Station 7 and Station 8 have lower wind speed ratios between 0.1 – 0.2. Station 5 reports the highest wind speed ratio of 0.74 among all canyon stations at θ_{rf} = 45°, the ratio then decreases with increasing θ_{rf} until $U_{st5}/U_{rf} = 0.14$ at θ_{rf} = 90°.

The characteristics of wind speed ratios could be understood with the analysis of canyon wind directions and flow patterns. Figure 4.7 shows the wind direction at each canyon station at θ_{rf} = 45° and θ_{rf} = 90°. At both angles Station 3 is influenced by wind through the gap. However, Station 6 seems to be dominated by the flow through the gap of the buildings at θ_{rf} = 45° but dominated by the flow entered from the east end of the canyon at θ_{rf} = 90°. The commonality of the two stations, which is likely to be the reason of their similar wind speed ratios, is that both stations are under the influence of the primary flow. The low wind speed measured at Station 7 and Station 8 is probably because they are always in the recirculation bubble of the building on the east end. At θ_{rf} = 45°, Station 5 is affected by the flow through the gap, but at θ_{rf} = 90°, its direction suggests that it is enclosed in the recirculation zone of the building, thus reporting a reduced wind speed ratio comparable to Station 7 and Station 8.

All the canyon stations set up in this measurement are in the areas frequently used by residents. Therefore, it is justifiable to average the wind speed ratios of all canyon stations to generate an overall estimate of the wind condition on the eco-deck. The resultant wind speed ratio is also shown in Figure 4.6, which is not sensitive to wind direction change from 45° to 90°. Hence averaging over wind directions is performed and the final canyon-to-roof wind speed ratio is 0.344.

The variation of the wind speed ratios with wind direction can also be analyzed with respect to the angle of attack α, which is defined in Figure 4.7a as the angle between the incoming wind and the normal of the canyon. Figure 4.6 has the angle of attack α listed on the top axis which will be compared to the SW monsoon results and discussed later. Moreover, flow channeling does not seem to happen at these four major wind directions in the NE Phase I measurement.

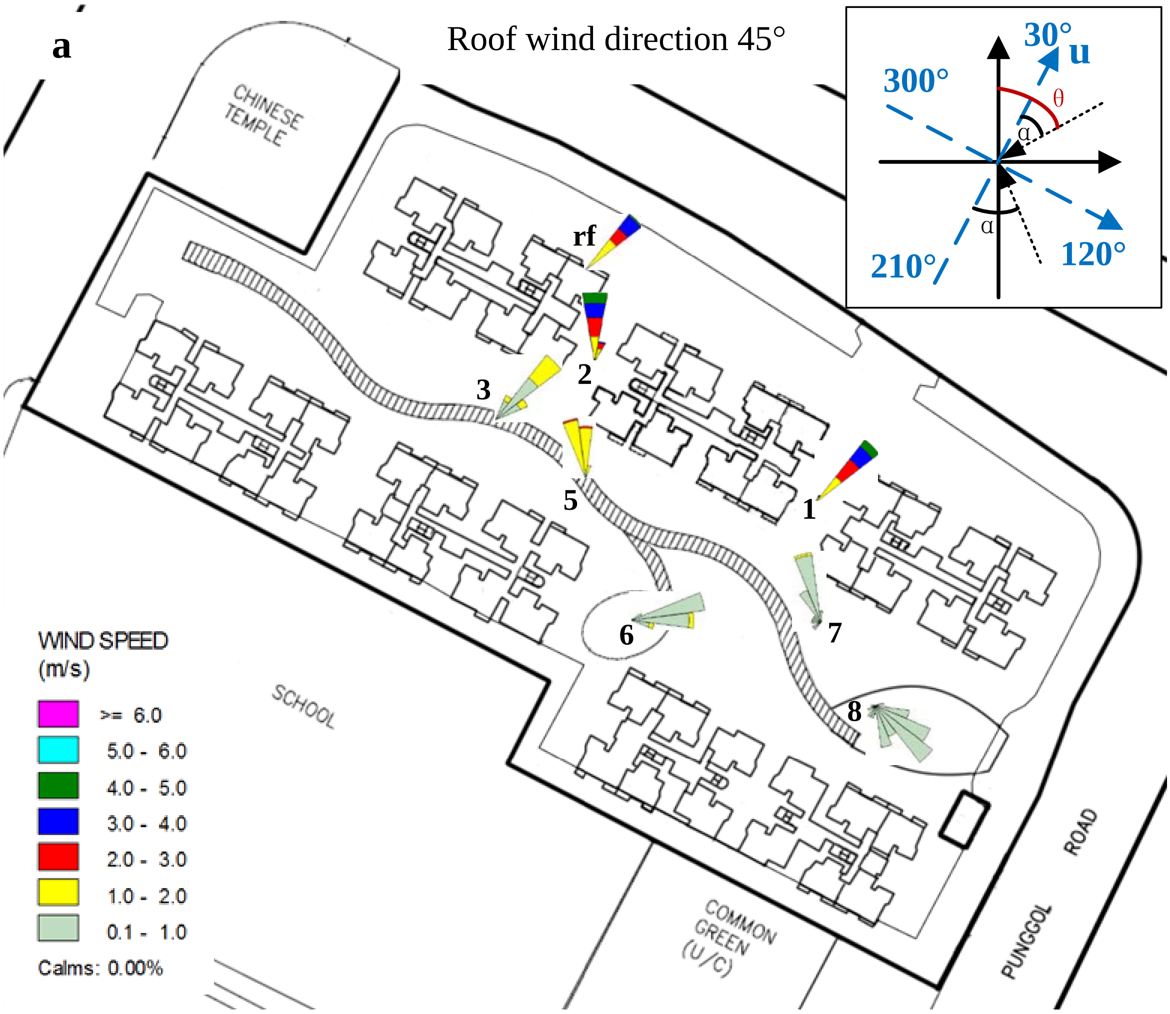

Figure 4.7 a. Wind roses of the roof station and the ground stations in NE Phase I when the roof wind direction is 45°. Top right: The definition of the local coordinate (blue dashed coordinate), wind direction θ and the angle of attack α at two approaching wind directions (dotted arrow).

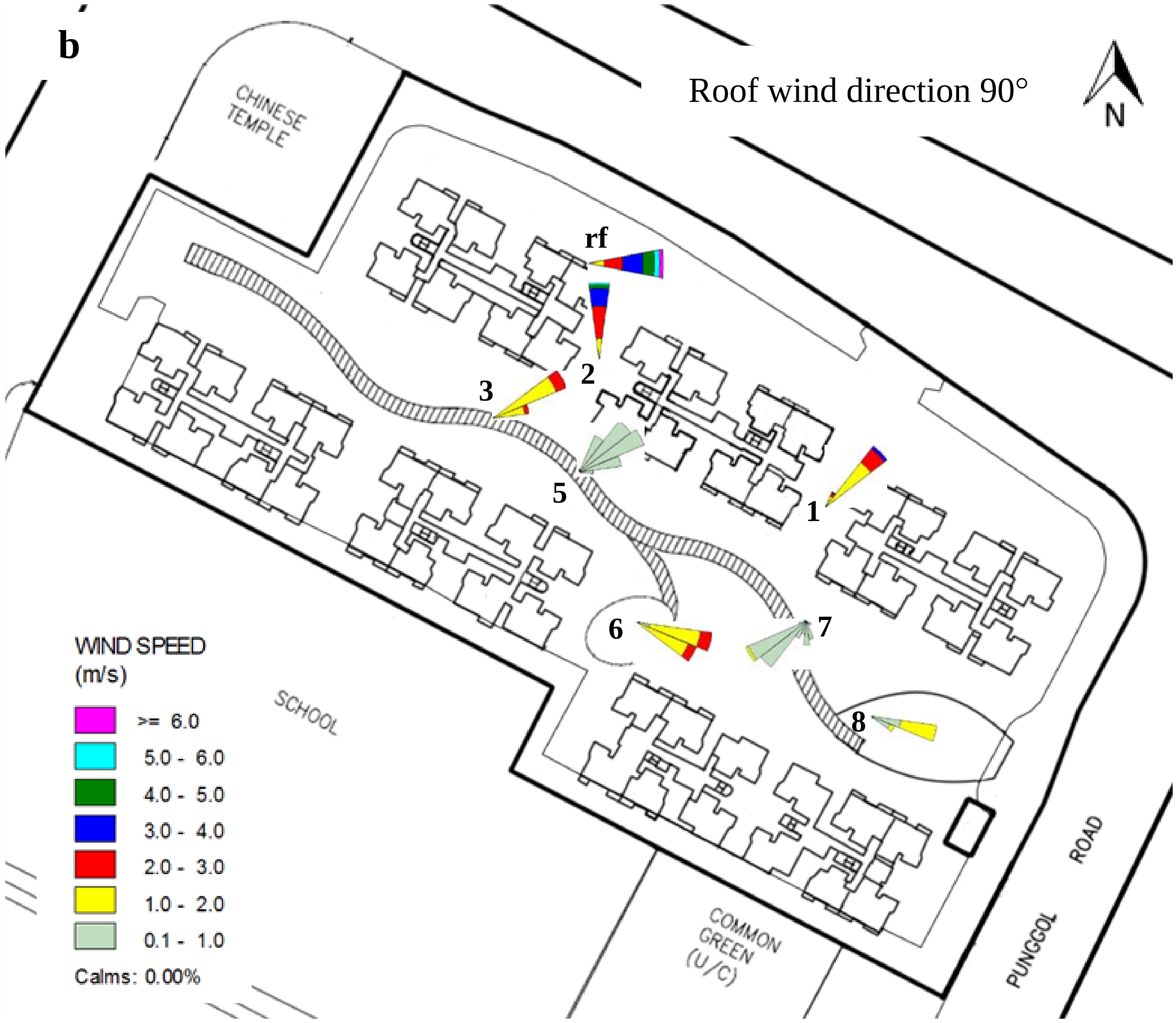

Figure 4.7 b. Wind roses of the roof station and the ground stations in NE Phase I when the roof wind direction is 90°.

4.4.2 SW Monsoon Season

In the NE Phase I the angle of attack $\alpha = 15° - 60°$, whereas more oblique wind happened in the SW Phase I with $\alpha = 45° - 90°$ (Figure 4.8). The common angles are $\alpha = 45°$ and $\alpha = 60°$, at which eco-deck flow characteristics measured in the SW monsoon are expected to be similar to the measurements in the NE monsoon. For $\alpha > 60°$ in the SW monsoon, flows are expected to change according to the trend.

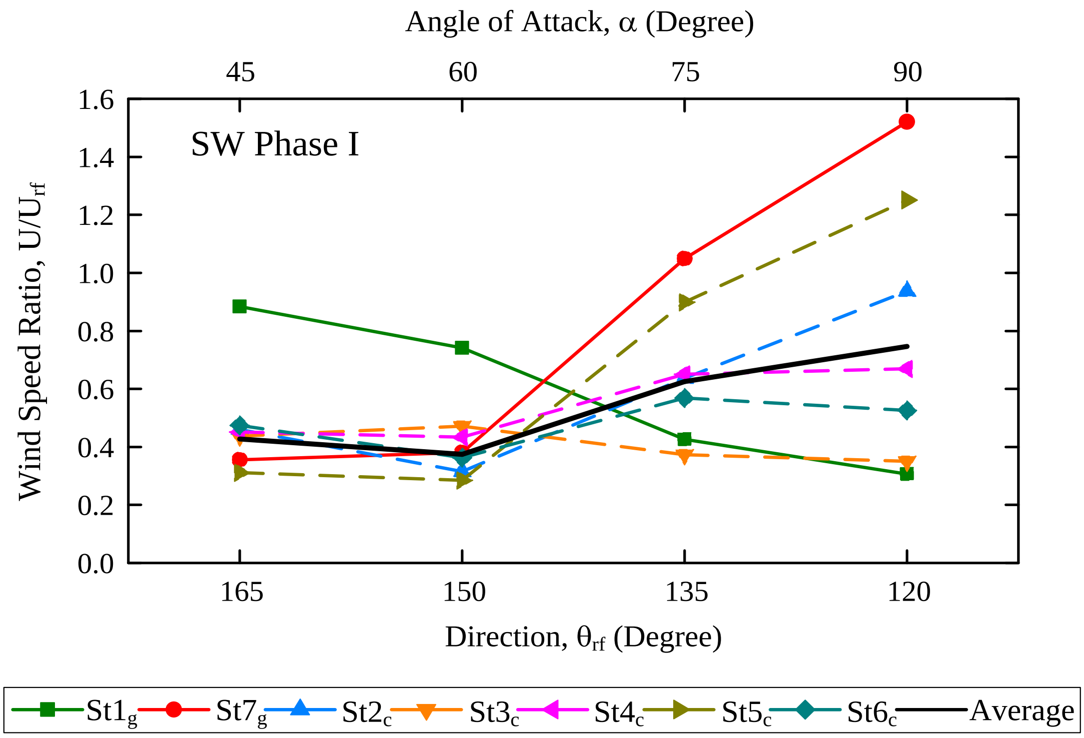

Figure 4.8 Wind speed ratio of each station on the eco-deck at four different prevailing wind angles during SW Phase I measurement. Solid line – gap stations; dotted line – canyon stations; bold black line – average of all canyon stations.

The measurement results are in general agreement with the prediction (Figure 4.8). At θ_{rf} = 165° and θ_{rf} = 150°, Station 1 (Station locations refer to Figure 4.9a) in the upwind gap measured higher wind speed (U_{st1}/U_{rf} = 0.884 and 0.741, respectively) than other stations on the eco-deck. The wind speed ratio at Station 1 then decreases as the prevailing wind becomes parallel to the canyon, and at θ_{rf} = 120° it measures the lowest wind speed among all eco-deck stations (U_{st1}/U_{rf} = 0.306). In contrast, Station 7 in the downwind gap exhibits the opposite trend. Low wind speed is reported at θ_{rf} = 165° and θ_{rf} = 150°, U_{st7}/U_{rf} = 0.355 and 0.381, respectively. As the angle of attack increases, the wind speed increases substantially to U_{st7}/U_{rf} = 1.521 at θ_{rf} = 120°.

The variation of wind speed ratios of the gap stations is accompanied by drastic change in flow patterns. Figure 4.9 compares the eco-deck flow patterns at θ_{rf} = 165° and θ_{rf} = 120°. It shows that at θ_{rf} = 165° wind directions at Station 1 and Station 7 are southerly (Figure 4.9a), due to the strong southerly component of the prevailing wind. However, at θ_{rf} = 120° the wind direction at Station 1 is highly fluctuating and Station 7 measures northerly wind (Figure 4.9b). Combined with the wind direction observations at other canyon stations, it implies such a flow pattern that when the prevailing wind is parallel to the canyon, flow channeling occurs along the canyon and air is sucked in through the pores of the canyon wall. That the suction is observed on the north side of the canyon but not the south side might be because there is a four-story school building on the immediate south of the Treelodge site blocking the flow. However, further evidence such as simulation is needed to verify the hypothesis that porous canyon leads to flow suction when strong flow channeling occurs.

At θ_{rf} = 165° and θ_{rf} = 150°, i.e. α = 45° and α = 60°, the wind speed ratios of the canyon stations (Station 3 – Station 6) clustered around 0.400 with maximum deviation of 0.115 (Figure 4.8), which is similar to the average canyon station wind speed ratio observed in the NE monsoon at the same angle of attack. As the angle of attack increases, the SW canyon wind speed ratios start to increase at different rates for different stations. The average U_{canyon}/U_{rf} grows to 0.747 at θ_{rf} = 120°, and the largest wind speed ratio at Station 5 differs from the smallest ratio at Station 3 by 0.901. The distinction between the wind speed ratios at θ_{rf} = 150° - 165° and the wind speed ratios at θ_{rf} = 120° - 135° is probably due to the onset of channeling flow along the canyon. At θ_{rf} = 165° (Figure 4.9a) Station 2 is affected by the flow through the gap, and Station 5 and Station 6 seem to be in the recirculation zone of the building on the south. On the contrary, at θ_{rf} = 120° (Figure 4.9b) all the above stations exhibit easterly flow along the canyon.

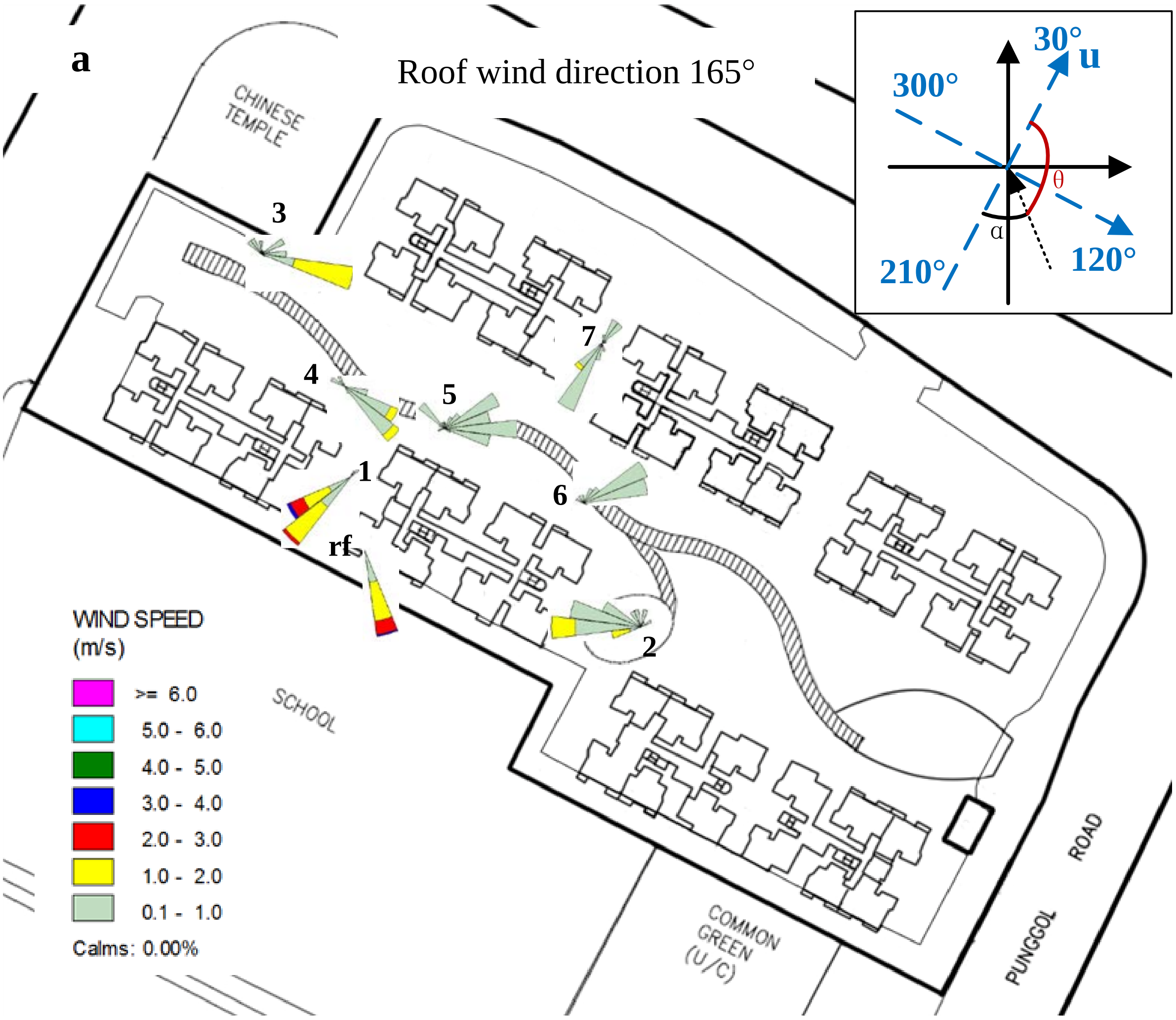

Figure 4.9 a. Wind roses of the roof station and the ground stations in SW Phase I when the roof wind direction is 165°. Top right: The definition of the local coordinate (blue dashed coordinate), wind direction θ and the angle of attack α at two approaching wind directions (dotted arrow).

Figure 4.9 b. Wind roses of the roof station and the ground stations in SW Phase I when the roof wind direction is 120°.

Although the Treelodge site is not a symmetric canyon, attempts have been made to combine the observations from the NE monsoon and the SW monsoon based on some common characteristics. It is suggested that for the Treelodge structure, U_{canyon}/U_{rf} is not sensitive to wind direction changes when $15° < \alpha < 60°$. The ratio is around 0.4, which is comparable to the findings by Hanna et al. [11] although their results represent the average ground-to-roof wind speed ratio over various prevailing wind conditions and the complex downtown terrain.

This ratio is smaller than what were reported in some typical canyon studies by DePaul and Sheih [12], Nakamura and Oke [13] and Rotach [14] (Table 2.1). The reason might be that in these studies, the in-canyon wind speed was monitored only at the center of the canyon, thus other locations with lower wind speed were not sampled.

At the angle of attack $\alpha > 60°$, U_{canyon}/U_{rf} increases as the above-roof wind direction turns parallel to the canyon axis, and flow channeling along the canyon becomes prominent and the wind speed ratios at most canyon stations increase. Brown et al. [15] observed in the field study of an urban canyon in downtown Oklahoma City that channeling through the entire length of the canyon was rare. For oblique wind sometimes up to 50° to the normal of the canyon, end vortex often appears at the upwind end of the canyon and channeling or complex mixed wind direction could appear near the downwind end of the canyon. In the current geometry, the porosity of the canyon wall further hindered flow channeling through the canyon at small angle of attack.

4.5 Vertical Wind Profiles

The weather stations installed at different heights in the buildings in the NE Phase II and the SW Phase II are meant to provide a profile of flow available for ventilating the buildings naturally. This profile is not equivalent to the wind profile measured in the canyon such as in [14]. Hence no deduction on the flow pattern in the canyon beyond the ground level is made based on the results in this section. Moreover, the opening sizes and the surrounding environments are different for the stations in the upwind buildings and in the downwind buildings. Therefore, comparison between the simultaneous measurements in the upwind building and the downwind building is not appropriate. However, installation conditions in the upwind buildings (Block 306C in NE Phase II and Block 306B in SW Phase II) are kept the same for both NE and SW monsoon seasons, and the same applies to the downwind buildings. Therefore, it is valid to compare the wind profile measured in the upwind building in the NE monsoon and the wind profile measured in the upwind building in the SW monsoon.

The prevailing wind in NE Phase II was north-northeast wind (345° - 60°) with a stronger northerly component compared to NE Phase I (Figure 4.10 a). The incoming wind in SW Phase II has the same direction range as SW Phase I (120° - 165°) (Figure 4.10 b).

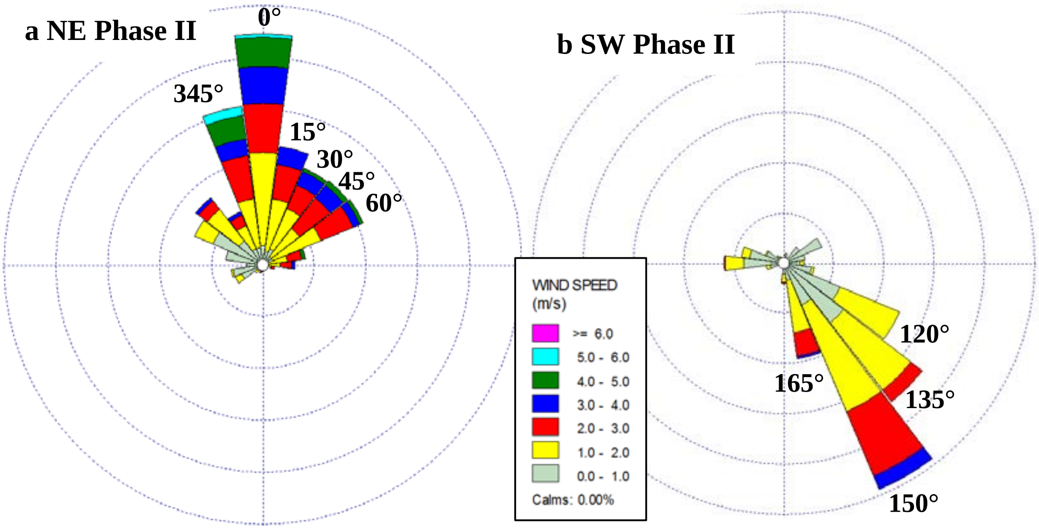

Figure 4.10 Wind rose of the roof station in a) NE Phase II, and b) SW Phase II.

The wind speed measured at different heights of the building in the NE monsoon (NE Phase II) is shown in Figure 4.11 against different approaching wind directions in the form of wind speed ratio, which has the same definition as Section 4.4. Due to the malfunction of the weather station on the 3rd level of the upwind building 3, the data at that height is not available. In general, for the downwind building the wind speed does not vary significantly with height and is also not sensitive to the approaching wind direction. An average wind speed ratio across all directions and all downwind stations is 0.332 with standard deviation of 0.037. For the upwind building the wind speed near the top of the building (15th level) has a small difference with the wind speed at the mid-height (9^{th} level), and they respond more to the wind direction variation.

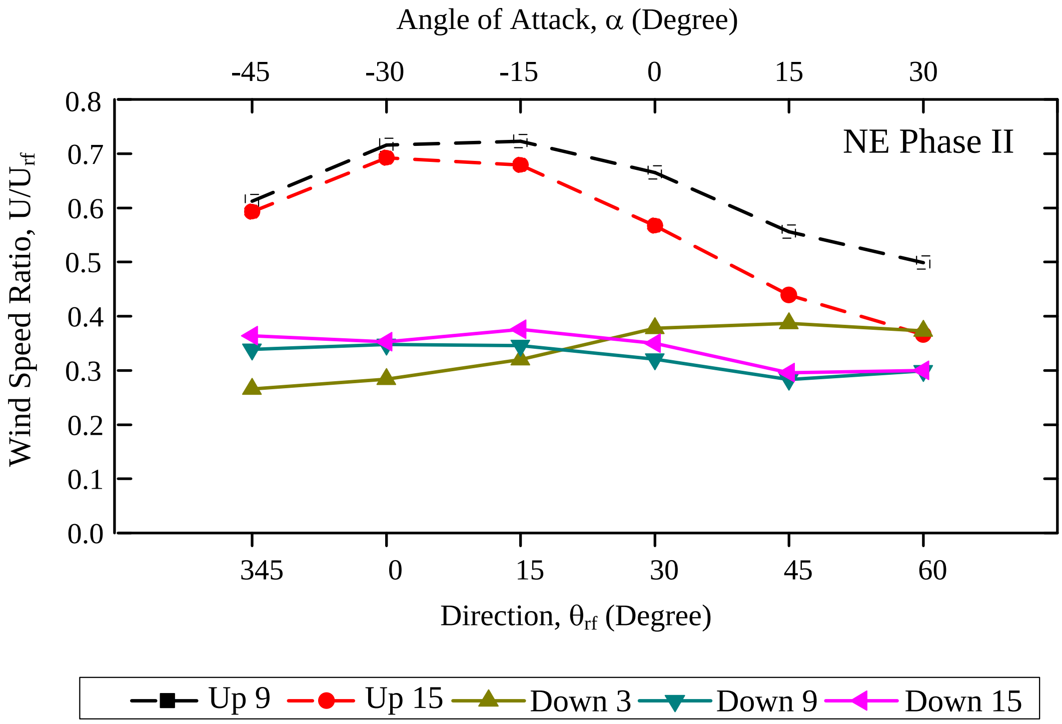

Figure 4.11 Wind speed ratio of each station in the buildings at six different prevailing wind angles during NE Phase II measurement. Dashed line – upwind building; Solid line – downwind building; "Up" – upwind building; "Down" – downwind building; "Up 9" – the 9^{th} level of the upwind building.

The wind speed measured in the downwind building in the SW Phase II demonstrates almost the same characteristics as the downwind building in the NE monsoon, that is the wind speed is approximately constant with height and insensitive to wind direction changes (Figure 4.12). The downwind building average wind speed ratio is 0.171 with standard deviation of 0.056. However, the wind speed in the upwind building appears to be affected by the prevailing wind direction. At θ_{rf} = 120° and θ_{rf} = 135°, the upwind building has a constant wind profile, whereas at θ_{rf} = 150° and θ_{rf} = 165°, the wind speed decreases exponentially as it goes deeper into the canyon. Further inspection shows that at 150° and 165°, wind enters the upwind building from the south, whereas at 120° and 135° the wind enters the building from the north. In other words, the wind profiles at 150° and 165° are more likely to reflect the incoming wind velocity profile from the south to the Treelodge buildings. Hence, it is suspected that the wind velocity profile in the urban canopy might be exponential.

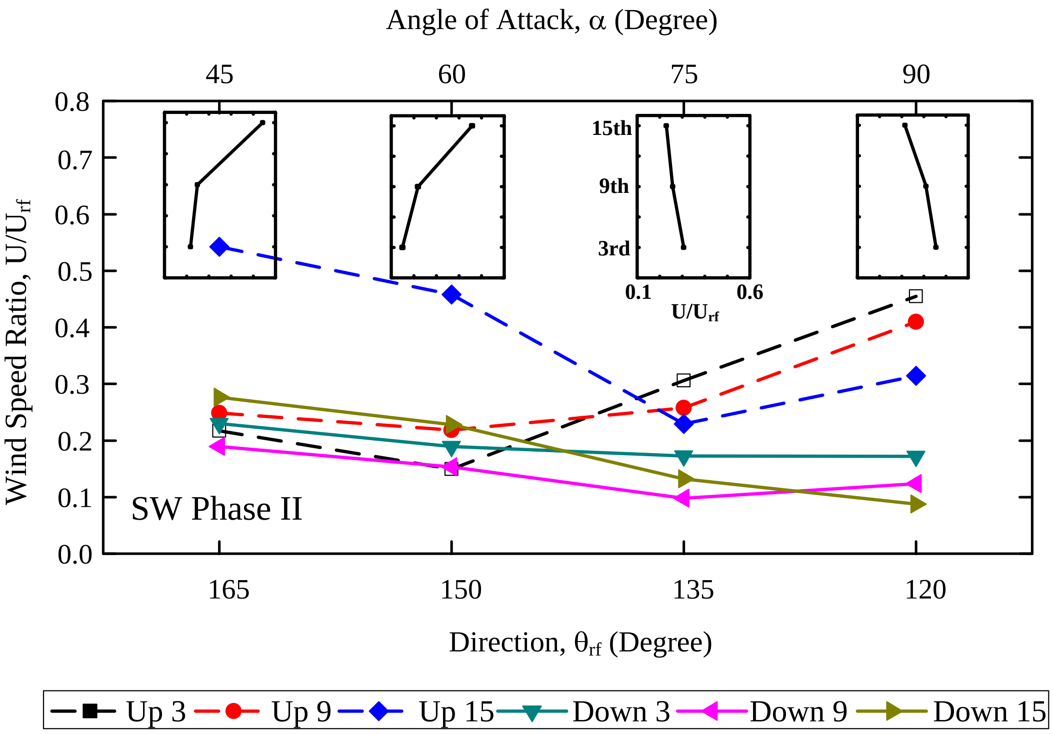

Figure 4.12 Wind speed ratio of each station in the buildings at four different prevailing wind angles during SW Phase II measurement. Dashed line – upwind building; Solid line – downwind building; “Up” - upwind building; “Down” – downwind building; “Up 9” – the 9th level of the upwind building. Wind profiles at different prevailing wind angles measured in SW Phase II.

In Chapter 2, the equation of the exponential velocity profile in an urban canopy has been reviewed and experiments suggest that it is only applicable to frontal area density less than 0.3 [16]. Thus, for the Treelodge precinct which has a frontal area density of 0.48, the exponential profile should not be observed in principle. However, the above criterion was obtained from wind-tunnel experiments of regular array, but in reality buildings are not uniform. South of the Treelodge is a community park that has almost zero building height. Therefore, one possible explanation of the observation of the exponential wind profiles in the upwind building during the SW monsoon at θ_{rf} = 150° and θ_{rf} = 165° is that the local reduction of building density allows the development of the exponential profile.

The nearly constant wind profiles measured in the downwind buildings in both NE and SW monsoon seasons can be backed up by the theory proposed by Bentham and Britter [17], which is also reviewed in Chapter 2. It is worth noticing that in both NE monsoon and SW monsoon, however different the wind profiles in the upwind building are, constant wind profiles form in the downwind building which is just one building height apart.

On average the wind speed ratios in the SW monsoon are smaller (half for downwind buildings) than their counterparts in the NE monsoon. To make the situation worse, the roof wind speed in the SW monsoon is only about half of the NE monsoon. In other words, the building ventilation rate in the SW monsoon season could only be a quarter of the NE monsoon. This is a clear evidence of the favorable location of the Treelodge during the NE monsoon.

4.6 Turbulence

The Vaisala weather stations record wind speed at 1Hz, thus only part of the turbulence spectrum is measured in this experiment. The turbulence fluctuations, u' and v', are obtained by subtracting the 10 min-average $\bar{u}$ and $\bar{v}$ from the instantaneous velocity u and v. Subsequently, the root mean square (rms) of u' and v' over each 10-min period were taken to generate σ_u and σ_v.

As reviewed in Chapter 2, the maximum turbulence fluctuation can be found around building height. Below and above roof height are more uniform profiles [18]. The turbulence level above the canopy has been reported as $\sigma_{u\_above} = 2.4\, u_*$ and $\sigma_{v\_above} = 1.9\, u_*$ [18-19], where u_* is the friction velocity computed from surface shear stress. The turbulence level within the canopy layer has been summarized from a few wind-tunnel experiments, for $\lambda_f > 0.4$, $\sigma_u = 1.0\, u_*$ and $\sigma_v = 1.0\, u_*$[20]. Combining the relations, it suggests that the σ_u and σ_v above the canopy are about twice the σ_u and σ_v in the canopy.

4.6.1 Turbulence at the Roof

The data available above the buildings in the current measurement at Treelodge were only provided by the roof stations. Conventionally, *u* and *v* represent the longitudinal and transverse wind components. When the turbulence is non-isotropic (e.g. $\sigma_{u\_above} = 2.4\, u_*$ and $\sigma_{v\_above} = 1.9\, u_*$ [18-19]), this distinction is important. However, in the analysis so far, *u* and *v* are defined based on the local coordinate of the Treelodge buildings, which are not necessarily the longitudinal and transverse wind components. This decomposition is less a problem for flow in the canyon, because the canyon geometry restricts the flow direction in the canyon so that it is more or less along the *u* or *v* direction. However, the roof wind directions are known to be different from the *u* and *v* directions (the wind rose plots in Figure 4.5 and Figure 4.10). Does the current definition of *u* and *v* affect the result? To answer this question, the conventional wind vector decomposition was performed on roof wind speed and direction in each measurement phase. Only small differences were found between σ_u and σ_v from the two methods. Therefore, decomposition of turbulence at the roof level is based on the canyon coordinates to be consistent with the other stations.

Turbulence intensity is also an important parameter of turbulent flow. In wind tunnel experiments it can be easily defined as u'/U where U is the inlet longitudinal velocity. This definition is difficult to apply to non-unidirectional flow, as in the current study. As a result, a new turbulence intensity is defined as

$$I_{rf} = \sigma_{rf}/U_{rf} \tag{4.6}$$

where U_{rf} is the roof wind speed magnitude and σ_{rf} is equivalent to the average of u' and v'.

$$\sigma_{rf}{}^2 = \sqrt[2]{\overline{(u'v')^2}}. \tag{4.7}$$

Figure 4.13 shows the time history of roof σ_u, σ_v and the resultant σ_{rf} during the NE Phase I measurement period. The roof σ_u and σ_v are similar to each other during the entire course of the measurement, exhibiting diurnal variations comparable to wind speed U_{rf} in Figure 4.4. The resultant σ_{rf} tracks closely the variation of σ_u and σ_v proving to be a valid measure of the roof turbulence. Similar observations are obtained in other measurement periods.

The roof turbulence intensities were then calculated and plotted against three variables, roof wind speed, roof wind direction and the hour of the day. No significant correlations were found except with roof wind speed (Figure 4.14). In general, I_{rf} increases with decreasing U_{rf} but at a higher rate when the wind speed is low. In the NE measurement where the roof wind speed covers a larger range, U_{rf} = 2.5 m/s is approximately the deflection point. In the SW measurement, however, data at high wind speed are not sufficient to allow the identification of an inflection point. Linear regressions are subsequently performed with U_{rf} = 2.5 m/s as the demarcation point where applicable. Strong similarities are found between the two phases in the same monsoon. For instance, in the NE monsoon although the predominant wind direction is 60° in the NE Phase I and 0° in the NE Phase II (Refer to Figure 4.5a and Figure

4.10a), their regression functions differ only in the third decimal place for $U_{rf} < 2.5$ m/s. For $U_{rf} > 2.5$m/s, I_{rf} is nearly independent of U_{rf} and is approximately ~0.3 in both cases. Compared to the NE monsoon, I_{rf} in the SW monsoon changes more slowly with U_{rf}. However, the ranges of I_{rf} at low wind speed are similar for both monsoon seasons, where I_{rf}(NE) ~ [0.1-0.9] and I_{rf}(SW) ~ [0.3-1.0].

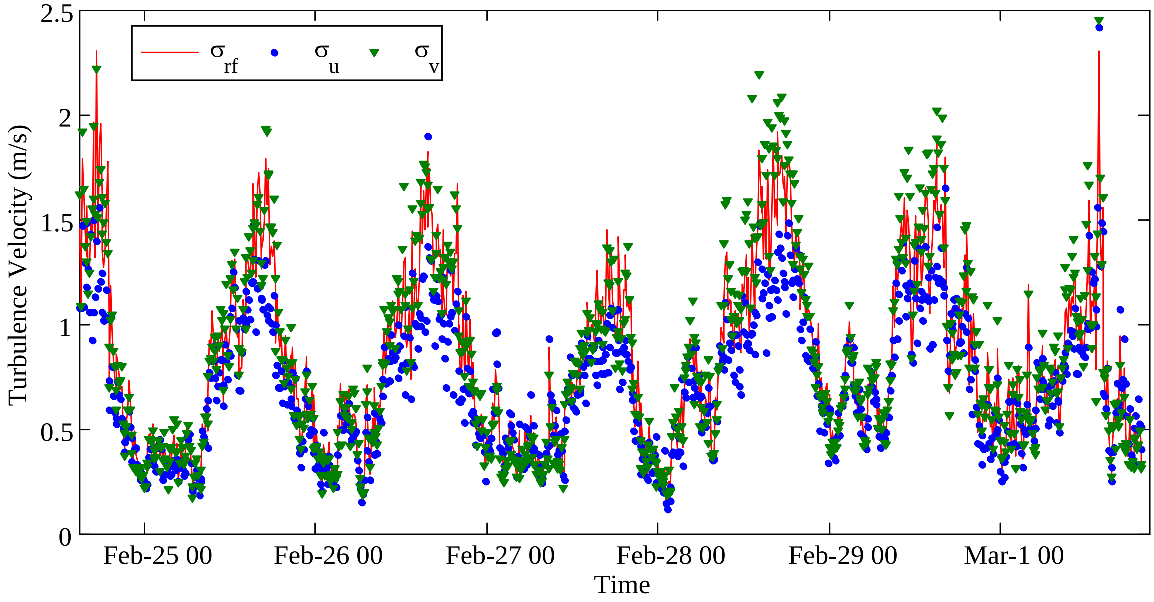

Figure 4.13 The rms of turbulence fluctuations, σ_u, σ_v and σ_{rf} of the roof station in the NE Phase I measurement.

The increase in turbulence intensity at low wind speed is probably the result of thermal effects. When the wind speed is high, the production of turbulence is dominated by the shear between the mean flow and the surface roughness. Given the large Reynolds number(~10^7), the flow is fully turbulent in this scenario and it is not surprising that turbulence intensity is independent of Reynolds number or the approaching wind velocity. However, in the low-wind condition, the production of turbulence through buoyant convection starts to have more weight and thus adds to turbulence intensity. If this hypothesis is correct, the turbulence intensity at low wind speed should be a function of ground-ambient temperature difference.

However, the current study does not have proper temperature measurements to verify this hypothesis.

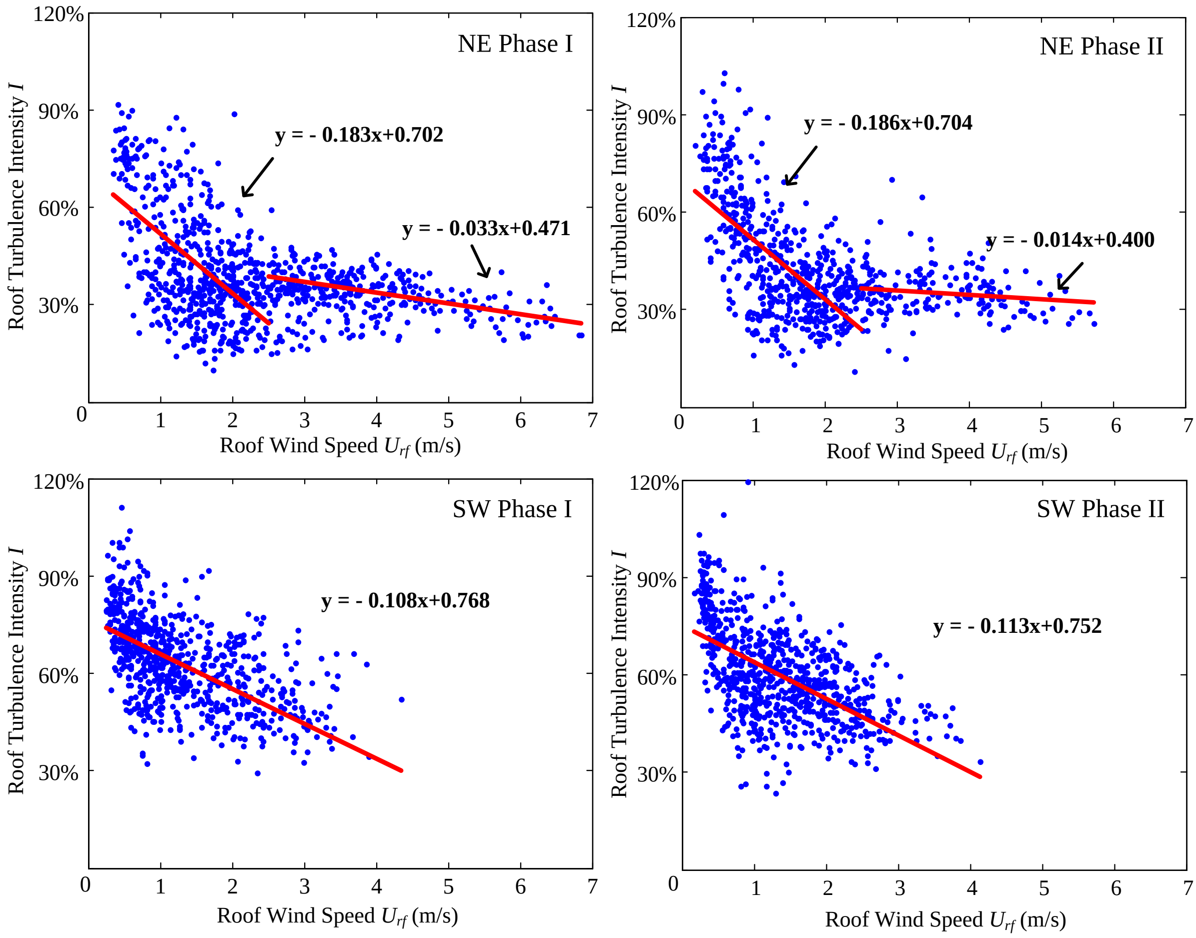

Figure 4.14 Variation of turbulence intensity *I* with roof wind speed U_{rf}.

4.6.2 Turbulence in the Canopy

The turbulence σ_u and σ_v in the building canopy also demonstrates clear diurnal variations. Figure 4.15 shows the σ_v of two ground stations in NE Phase I as well as the roof turbulence. The in-canopy turbulence is high during the day and low in the night with a magnitude smaller than that of the roof station.

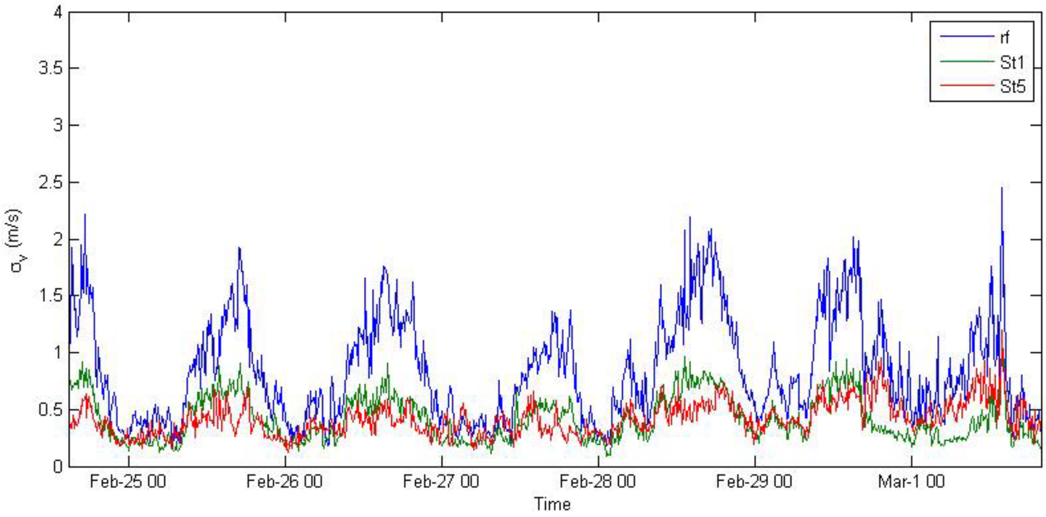

Figure 4.15 Diurnal variation of ground turbulence at Station 1 and Station 5 in the NE Phase I, comparing with the roof turbulence.

Field studies are characterized by constantly changing ambient conditions. Therefore, it is often necessary to normalize the measured data to rule out the changes of the boundary condition. The friction velocity measured in the inertial sublayer has been shown to be a useful scale [2, 18]. The square root of local Reynolds stress is also widely used [19, 21]. Because both of the above-mentioned variables are not available in the current study, two other scales are proposed, σ_{rf} and U_{rf}. A proper turbulence normalizing scale is expected to reduce the variability of σ_u and σ_v with time. Table 4.4 compares the standard deviation gauging the temporal variations of σ_u and σ_v [STD(t)] in each measurement period. STD(t) is computed using the method proposed by Hanna and Zhou [8]: the standard deviation of the 10-min rms value σ_u or σ_v is computed during each day at each station. There are 144 data points at each station on each day. The resulting STD(t) is then averaged over the five or six measurement days and further averaged over all the stations. It is obvious that normalization with σ_{rf} produces the smallest STD(t)/Mean for both σ_u and σ_v in all measurement periods. Normalization with U_{rf} can also reduce STD(t)/Mean in most cases except for NE Phase I but not as effectively. This is not surprising considering the previous observation that the roof turbulence is a function of roof wind speed, which means when the roof wind speed is not treated as a variable as in the case of σ_u/U_{rf}, additional variability would be introduced to the new combined variable. Therefore, σ_{rf} is chosen as the scale of the σ_u and σ_v of the in-canopy stations.

Table 4.4 Temporal variability of σ_u and σ_v normalized with σ_{rf} and U_{rf} and without normalization. The "Mean" is the average of all 10-min rms data in the corresponding measurement period.

	STD(t)/Mean w/o normalization		**STD(t)/Mean normalized w σ_{rf}**		**STD(t)/Mean normalized w U_{rf}**	
	σ_u	σ_v	σ_u/σ_{rf}	σ_v/σ_{rf}	σ_u/U_{rf}	σ_v/U_{rf}
NE Phase I	0.46	0.44	0.33	0.30	0.56	0.53
NE Phase II	0.52	0.45	0.33	0.31	0.43	0.47
SW Phase I	0.53	0.48	0.31	0.32	0.40	0.41
SW Phase II	0.57	0.48	0.30	0.31	0.36	0.43

The normalized σ_u and σ_v of all the in-canopy stations are presented in Figure 4.16. It can be observed that the temporal variability at each station, indicated by the error bar, is small, around 30% of the mean value (Table 4.5). The variability across different stations in each measurement period is also small. The STD(s) in Table 4.5 is a measure of spatial variability which is also suggested by Hanna and Zhou [8]. It is the standard deviation of the available in-canopy stations (7 or 8 stations) at each 10-min period and then averaged over the entire measurement period. STD(s)/Mean is also less the 40% of the mean value. Moreover, σ_u and σ_v for most stations are similar. For example, the mean σ_u/σ_{rf} and σ_v/σ_{rf} in SW Phase I is

0.54 and 0.55 (Table 4.5). Even if individual stations are examined (Figure 4.16), most stations have less than 30% difference. This is interesting given that the site is a canyon with strong geometric preference. The spatial uniformity and isotropy of turbulence indicate strong mixing in the porous canyon. It is likely that complex urban geometry tend to promote strong mixing and thus isotropic and spatially uniform turbulence. Hanna and Zhou [8] found similar results in the Manhattan Midtown 2005 Field Experiment and the 2003 Joint Urban Field experiment as listed in Table 4.5. σ_u and σ_v are almost exactly the same and the STD(s) is less than 50% of the mean. Comparing the MID05 results with the current study shows an interesting aspect that there is no sign of diurnal change in wind variables in MID05 in the data from 5 am local time to 12 am local time. This explains why MID05 has a smaller temporal variability STD(t) of 0.21 compared to the current study of ~0.3.

Table 4.5 Temporal and spatial variability of in-canopy stations in all measurement periods, and comparison with the spatial variability of the surface stations in MID05 and JU2003. The “Mean” is the average of all 10-min rms data in the corresponding measurement period.

	Mean		**STD(s)/Mean**		**STD(t)/Mean**		**STD(s&t)/Mean**	
	σ_u/σ_{rf}	σ_v/σ_{rf}	σ_u/σ_{rf}	σ_v/σ_{rf}	σ_u/σ_{rf}	σ_v/σ_{rf}	σ_u/σ_{rf}	σ_v/σ_{rf}
NE Phase I	0.62	0.58	0.33	0.23	0.33	0.30	0.41	0.34
NE Phase II	0.62	0.46	0.31	0.27	0.33	0.31	0.40	0.37
SW Phase I	0.54	0.55	0.36	0.30	0.31	0.32	0.43	0.39
SW Phase II	0.51	0.41	0.38	0.36	0.30	0.31	0.43	0.45
	σ_u	σ_v	σ_u	σ_v	σ_u	σ_v	σ_u	σ_v
MID05 [8]	0.64	0.65	0.22	0.31	0.21	0.21	0.27	0.33
JU2003 [8]	1.05	1.05	0.46	0.20	-	-	-	-

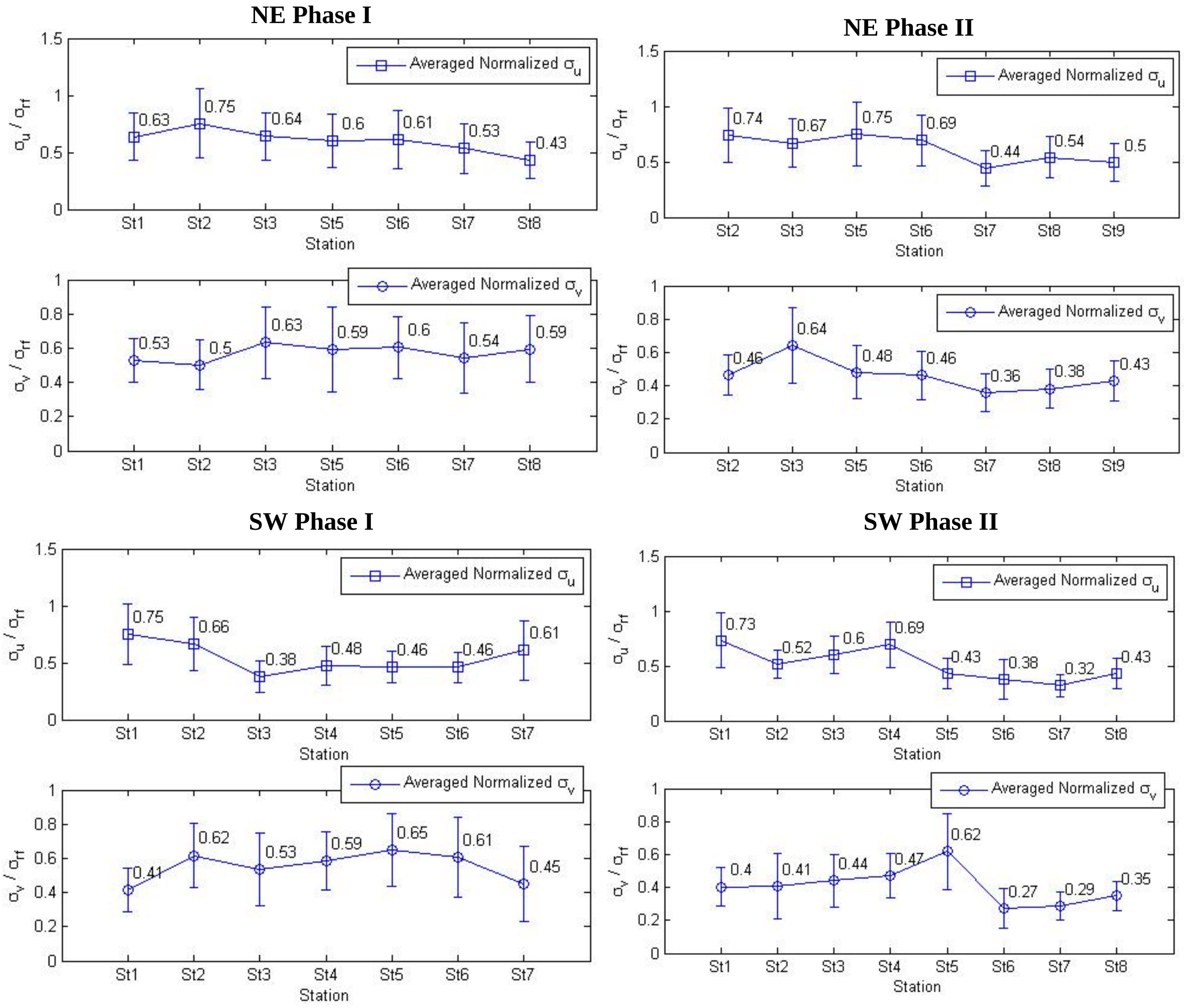

NE Phase I

NE Phase II

SW Phase I

SW Phase II

Figure 4.16 $\sigma_{u,v}/\sigma_{rf}$ of each station in each measurement period. The number is the mean value of $\sigma_{u,v}/\sigma_{rf}$ at each station averaged over the measurement period. The error bar indicates one standard deviation.

The in-canopy turbulence is about 40%-60% of the turbulence level at the roof (Table 4.5). It is also in agreement with the literature that the above-canopy turbulence is approximately twice of the in-canopy turbulence. This information and the knowledge of the roof turbulence intensity presented in Section 4.6.1 allow an estimation of the turbulence level in the Treelodge canyon for a given roof wind speed (Examples are given in Chapter 5). By further establishing the relation of the roof wind speed with the airport wind speed, the turbulence level could be estimated from airport wind speed, which is easily available.

4.7 Predicting Pedestrian Level Ventilation Potential from Wind Information on the Urban Scale

The ventilation effectiveness of a space can be gauged by the air change rate (*ACR*) of that space

$$ACR = \frac{Q}{Vol}, \tag{4.8}$$

where Q is the volumetric flow rate; and Vol is the volume of that space. For a given space that has fixed volume, the flow rate determines the air change rate. Considering an infinitesimal volume, the velocity at that point determines the air change rate at that point in space. In this study, only the horizontal wind components are measured, thus the total velocity at a point is unknown. However, since the horizontal components are stronger in the near-ground region of the canopy especially when the flow is fully developed [22], valuable information can be provided even if only the horizontal components of the flow velocity are considered. Therefore, as far as this study is concerned, the prediction of the ventilation potential at the pedestrian level is equivalent to the prediction of the horizontal velocity at the pedestrian level in the canopy. The rest of this section will provide a guideline of estimation of the pedestrian wind speed from an indicator of a larger scale wind speed such as the airport wind speed, based on the field measurement results obtained at the Treelodge.

The observations from the field measurement at the Treelodge are summarized in Table 4.6. The values of $U_{airport}$, $U_{rf}/U_{airport}$ and U_{canyon}/U_{rf} have been presented in the previous sections, from which the ratio of $U_{canyon}/U_{airport}$ can be derived as 0.34 for the NE monsoon and 0.19 for the SW monsoon. This means that for the Treelodge building group, during the NE monsoon the wind speed at the pedestrian level is 0.34 times of the airport wind speed, while during the SW monsoon the wind speed at the pedestrian level is 0.19 times of the airport wind speed. It also suggests that the *ACR* at the pedestrian level in the NE monsoon is about twice the *ACR* at the pedestrian level in the SW monsoon (NE/SW = 0.34/0.19 = 1.8).

Table 4.6 Summary of the Treelodge field measurement results from NE and SW monsoons.

	NE	**SW**
$U_{airport}$	Similar	Similar
$U_{rf}/U_{airport}$	1.0	0.47
U_{canyon}/U_{rf}	0.34	0.4
$U_{canyon}/U_{airport}$	0.34	0.19
$U_{downwind\ building}/U_{rf}$	0.33	0.17
$U_{downwind\ building}/U_{airport}$	0.33	0.08

The wind speed measured in the buildings can also be linked to the airport wind speed (Table 4.6). The downwind row of the buildings experiences around four times stronger wind speed in the NE monsoon than the SW monsoon, given the same airport wind speed (NE/SW = 0.33/0.08 = 4.1). The favorable location of the Treelodge building group in the NE monsoon is expected because of the open terrain on the North (Chapter 3).

Reference

1. Balogun, A.A., Tomlin, A.S., Wood, C.R., Barlow, J.F., Belcher, S.E., Smalley, R.J., Lingard, J.J.N., Arnold, S.J., Dobre, A., Robins, A.G., Martin, D., and Shallcross, D.E., "In-street wind direction variability in the vicinity of a busy intersection in central London," *Boundary-layer Meteorology*, 136 pp 489-513, 2010.

2. Louka, P., Belcher, S.E., and Harrison, R.G. "Coupling between air flow in street and the well-developed boundary layer aloft," *Atmospheric Environment*, 34, pp 2613-2621, 2000.

3. Nakamura, Y., and Oke, T. R., "Wind, Temperature and Stability Conditions in an East-West Oriented Urban Canyon," *Atmospheric Environment*, 22, pp 2691-2700, 1988.

4. Rotach, M.W., "Profiles of Turbulence Statistics in and above an Urban Street Canyon," Atmospheric Environment, 29, pp 1473-1486, 1995.

5. Niachou, K., livada, I., Santamouris, M., "Experimental Study of temperature and Airflow Distribution inside an Urban Street Canyon during Hot Summer Weather Conditions – Part I: Air and Surface Temperatures," *Building and Environment*, 43, pp 1383-1392, 2008.

6. World Meteorological Organization. "WMO Guide to Meteorological Instruments and Methods of Observation, Part II Observing Systems, Chapter 11 Urban Observation," Internet:ftp://ftp.wmo.int/Documents/MediaPublic/Publications/WMO8_CIMOguide/WMO8_Ed2008_Up2010_en.pdf. Aug, 2008 [27 Oct 2014].

7. Balogun, A.A., Tomlin, A.S., Wood, C.R., Barlow, J.F., Belcher, S.E., Smalley, R.J., Lingard, J.J.N., Arnold, S.J., Dobre, A., Robins, A.G., Martin, D., and Shallcross, D.E.,

"In-street wind direction variability in the vicinity of a busy intersection in central London," Boundary-layer Meteorology, 136 pp 489-513, 2010.

8. Hanna, S.R., and Zhou, Y., "Space and Time Variations in Turbulence during the Manhattan Midtown 2005 Field Experiment," Journal of Applied Meteorology and Climatology, 48, pp 2295-2304, 2009.

9. Yang, F., Qian, F., and Lau, S.S.Y., "Urban Form and Density as Indicators for Summertime Outdoor Ventilation Potential: A Case Study on High-Rise Housing in Shanghai," *Building and Environment*, 70, pp 122-137, 2013.

10. Ng, E., "Policies and Technical Guidelines for Urban Planning of High-Density Cities – Air Ventilation Assessment (AVA) of Hong Kong," *Building and Environment*, 44, pp 1478-1488, 2009.

11. Hanna, S., White, J., and Zhou, Y., "Observed Winds, Turbulence, and Dispersion in Built-up Downtown Areas of Okalahoma City and Manhattan," *Boundary-Layer Meteorology*, 125, pp 441-468, 2007.

12. DePaul, F. T., and Sheih, C. M., "Measurements of Wind Velocities in a Street Canyon," *Atmospheric Environment*, 20, pp 455-459, 1986.

13. Nakamura, Y., and Oke, T.R., "Wind, Temperature and Stability Conditions in an East-West Oriented Urban Canyon," *Atmospheric Environment*, 22, pp 2691-2700, 1988.

14. Rotach, M.W., "Profiles of Turbulence Statistics in and above an Urban Street Canyon," *Atmospheric Environment*, 29, pp 1473-1486, 1995.

15. Brown, M.J., Khalsa, H., Nelson, M., and Boswell, D., “Street Canyon Flow Patterns in a Horizontal Plane Measurements from the Joint Urban 2003 Field Experiment,” in *Proceedings of AMS Symposium on the Urban Environment,* Vancouver, B.C., 2004.

16. Macdonald, R. “Modelling the Mean Velocity Profile in the Urban Canopy Layer,” *Boundary-Layer Meteorology,* 97, pp 25-45. 2000.

17. Bentham, T., and Britter, R. “Spatially Averaged Flow within Obstacle Arrays,” *Atmospheric Environment,* 37, pp. 2037-2043. 2003.

18. Britter, R. E., and Hanna, S. R. “Flow and Dispersion in Urban Areas,” *Annual Review of Fluid Mechanics*, 35, pp 469-496, 2003.

19. Roth, M., “Review of Atmospheric Turbulence over Cities,” Quarterly Journal of the Royal Meteorological Society, 126, pp 941-990, 2000.

20. Lloyd, H., “Pollutant Dispersion in Urban Geometries – Turbulence within the Urban Canopy,” Fourth-Year Project Report, University of Cambridge, 2004.

21. Zajic, D., Fernando, J.S., Calhoun, R., Princevac, M., Brown, M.J., and Pardyjak, E.R., “Flow and Turbulence in an Urban Canyon,” *Journal of Applied Meteorology and Climatology,* 50, pp 203-223, 2011.

22. Hang, J., Li, Y., Buccolieri, R., Sandberg, M., and Di Sabatino, S., “On the Contribution of Mean Flow and Turbulence to City Breathability: The Case of Long Streets with Tall Buildings,” *Science of the Total Environment,* 416, pp 362-373, 2012.

Chapter 5 Estimation of Wind-Driven Natural Ventilation Rate

5.1 Chapter Overview

This chapter discusses two types of wind-driven natural ventilation, cross ventilation and single-sided ventilation. First, a study that relates wind pressure coefficient difference ΔC_p to morphological variables λ_p and λ_f is presented [1], and the ΔC_p corresponding to the Treelodge's λ_p and λ_f is found to generate the theoretical flow rate achievable at the Treelodge in the process of cross natural ventilation. Good agreement is found between the computed and the measured data. Second, simulations on a room with a single opening are performed to investigate the characteristics of the single-sided ventilation. The CFD simulation is validated by the wind tunnel experiment performed by Larson and Heiselberg [2]. Then two parameters that affect the flow, the incident angle of the wind and the turbulence intensity, are tested for the model. The results suggest that the air change rate increases with increasing turbulence intensity expect for the wind angle of 180°.

5.2 Estimate Wind-Driven Cross-Ventilation Flow Rate for High-Rise Buildings

5.2.1 Wind Pressure Coefficient for Buildings in Urban Areas

As reviewed in Chapter 2, the pressure difference Δp between the windward and the leeward facades of a building determines the flow rate,

$$Q = C_D A \sqrt{\frac{2\Delta p}{\rho}} \tag{5.1}$$

And the pressure difference can be reflected by the wind pressure coefficient difference ΔC_p at a certain reference wind speed

$$\Delta p = \Delta C_p \rho \frac{{U_{ref}}^2}{2} \tag{5.2}$$

Substitute Eq. 5.2 into Eq. 5.1. An effective area $A_{eff} = A/\sqrt{2}$ should be used for windward and leeward openings of the same area A, because the pressure difference Δp is across two openings.

$$Q = C_D A_{eff}\sqrt{\frac{2\Delta p}{\rho}} = C_D \frac{A}{\sqrt{2}} U_{ref}\sqrt{\Delta C_p}. \tag{5.3}$$

The ΔC_p, which is influenced by a few parameters including the shape of the building, the density of the buildings and the choice of the reference wind speed, is usually obtained through wind-tunnel experiments. Truong [1] found a way to combine the measured ΔC_p from different wind-tunnel experiments by using a common reference wind speed, which is the wind speed at 100m above the urban area. The standardized ΔC_p is then plotted against the plan area density λ_p with color coding of the frontal area density λ_f (Figure 5.1). The plan area density λ_p of Treelodge and the surround neighborhoods is 0.24 and the frontal area density λ_f is around 0.48 depending on the incident wind angle. Reading from Figure 5.1, the ΔC_p of the Treelodge area is within the range of [0.05-0.07], thus $\Delta C_p = 0.06 \pm 0.01$.

Another coefficient in Eq. 5.3 is the discharge coefficient C_D, which is normally assumed to be 0.6. However, since the Treelodge corridor is almost fully open and has only railing not wall at the bottom half, a larger C_D should be used. Vickery et al. [3] conducted wind tunnel experiments with low-rise buildings and found that when the window area is nearly the same as the wall area, $C_D = 0.8$. This value is thus chosen for Treelodge.

Substituting the value of ΔC_p and C_D into Eq. 5.3, and converting volumetric flow rate Q into velocity V,

$$V = \frac{Q}{A} = \frac{0.8}{\sqrt{2}} * \sqrt{0.06 \pm 0.01} U_{ref}, \tag{5.4}$$

Or

$$\frac{V}{U_{ref}} = 0.14 \pm 0.012. \tag{5.5}$$

U_{ref} is the reference wind speed at 100m.

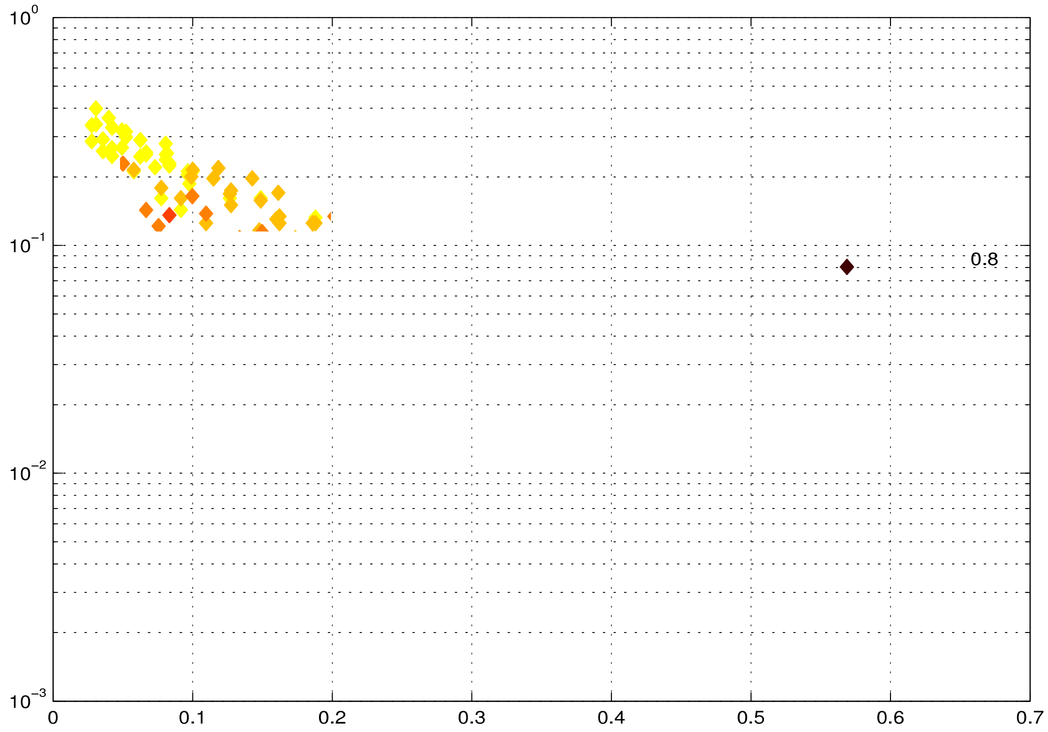

Figure 5.1 Variation of surface-averaged ΔC_p with λ_p and λ_f. Data are shown for normal wind incident angle [1].

5.2.2 Wind Speed in Buildings from Treelodge Field Measurement

As presented in Chapter 3 and Chapter 4, in the Treelodge field measurements, wind speed was measured at the corridor openings on the 3rd, 9th and 15th floor in the upwind and downwind buildings during the NE and SW monsoons. Considering that the ΔC_p summarized in [1] is measured in the fully developed flow region, only the SW monsoon data is appropriate to be used for comparison with the computed flow velocity.

The wind speed ratio U/U_{rf} at different incident wind angles during the SW monsoon is shown again in Figure 5.2. The surface-averaged ΔC_p plotted in Figure 5.1 is obtained with normal wind incident angle to the buildings [1]. Therefore, the measurement data with the incoming flow more perpendicular to the buildings is more appropriate for comparison. In this case, wind speed at θ_{rf} = 165° and 150° are used. Except for the 15th floor of the upwind building, all the other wind speed ratios at θ_{rf} = 165° and θ_{rf} = 150° cluster within the range of 0.15 - 0.27, i.e.

$$\frac{V}{U_{rf}} = 0.21 \pm 0.06. \tag{5.6}$$

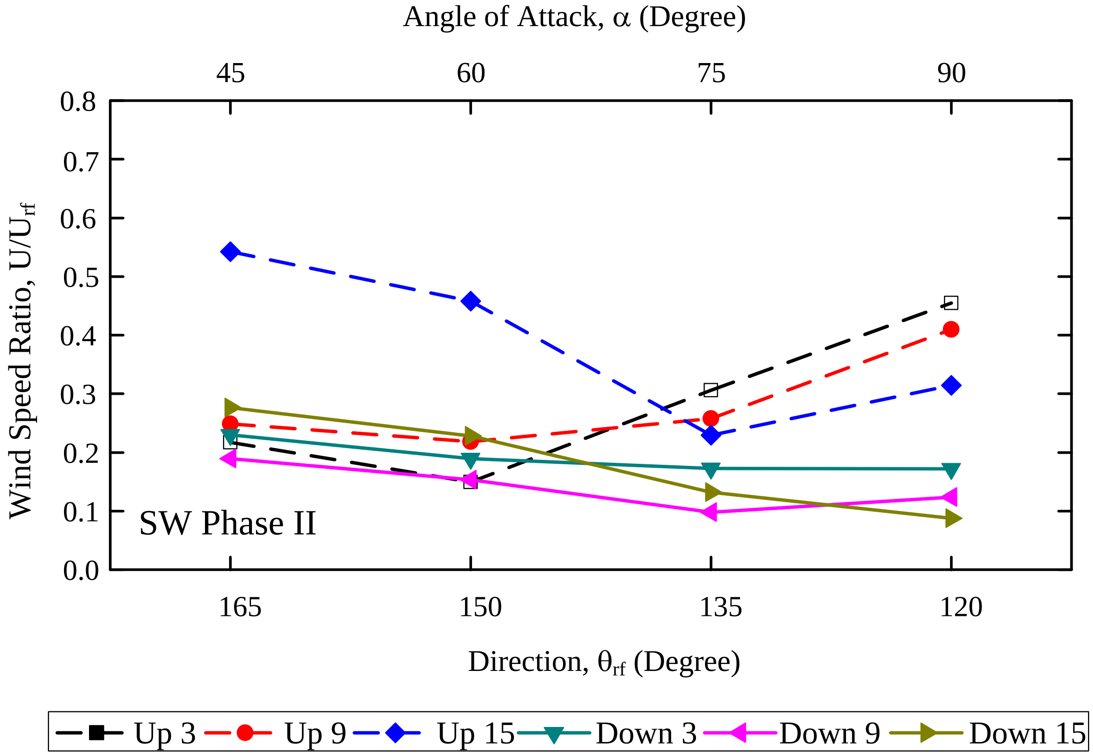

Figure 5.2 Wind speed ratio of each station in the buildings at four different prevailing wind angles during SW Phase II measurement. Dashed line – upwind building; Solid line –

downwind building; “Up” - upwind building; “Down” – downwind building; “Up 9” – the 9th level of the upwind building.

The reference wind speed at 100 m above the Treelodge area is unknown. There is also no simple method to estimate it from the measured roof wind speed with high confidence level. For a situation like this, the ASHRAE standards [4] recommend an approximation method by the power law

$$\frac{U_{rf}}{U_{ref}} = \left(\frac{50}{100}\right)^{0.33} = (\frac{1}{2})^{0.33}. \tag{5.7}$$

The exponent of 0.33 is cited from [4] for the high-rise urban terrain category. The resultant ventilation-velocity-to-reference-wind-speed ratio is

$$\frac{V}{U_{ref}} = \frac{V}{U_{rf}} * \frac{U_{rf}}{U_{ref}} = (0.21 \pm 0.06) * \left(\frac{1}{2}\right)^{0.33} = 0.17 \pm 0.05. \tag{5.8}$$

5.2.3 Discussion

The ratio of the cross-ventilation velocity to the reference wind speed V/U_{ref} computed from the empirical ΔC_p is 0.14± 0.012, and the V/U_{ref} obtained from the Treelodge field measurement is 0.17± 0.05. The two values agree relatively well and the field measurement result demonstrates slightly more variation. The good agreement suggests that the method of estimating the cross-ventilation flow rate of high-rise buildings based on the relationship between the empirical ΔC_p and the urban morphology parameters λ_p and λ_f is promising. However, it needs to be emphasized that in the current field measurement, wind speed was only measured at six locations in the buildings although the extended period of measurement provides some additional reliability of the data. Besides, the type of the opening at which the wind speed was measured is not the typical window seen in an apartment. The deduction of the reference wind speed at 100m might also introduce some errors. With all the uncertainties, the good match can be a coincidence. Further experiments are definitely required before any conclusion can be drawn.

5.3 Wind-Driven Single-Sided Ventilation

The literature review in Chapter 2 has demonstrated that the non-dimensional flow rate $Q^* = Q/AU$ can be approximated by a constant of 0.025 for a room with a single opening. However, closer inspections has suggested that Q* is influenced by factors including the incident angle of the wind with respect to the window and the turbulence intensity of the incident flow. This section intends to examine the effect of these two factors by using steady-state CFD simulations.

5.3.1 CFD Settings and Validation

Before making use of the CFD simulations, validation of the model is required. In the current study, the wind-tunnel experiments reported by Larson and Heiselberg [2] are used to validate the CFD model.

5.3.1.1 Wind Tunnel Experiment

The wind-tunnel experiments were conducted in the Japanese Building Research Institute [5]. A full-scale one-room building sized 5.56 m × 5.56 m × 3 m was built in the wind tunnel, with an opening of 0.86 m × 1.4 m (width by height) and positioned 0.54 m away from the right edge of the building. The internal room height was 2.4 m and the thickness of the walls was 0.1 m. The room volume was 68.95 m^3 [2]. The dimension of the wind tunnel is shown in Figure 5.3. The wind tunnel generates a uniform velocity profile at the inlet and the wind speeds of 1, 3 and 5 m/s were tested in the experiment. The turbulence intensity was below

5%. The building model was constructed on a turntable and was rotated between 0° to 345° with either a 15° or a 30° increase in the incident wind angle. A tracer gas was released in the room and the concentration change was used to calculate the air change rate under different conditions. In some experiment cases, the room temperature was set to a different value than the ambient temperature, but since the temperature effect was not of interest in this study, those cases were not considered.

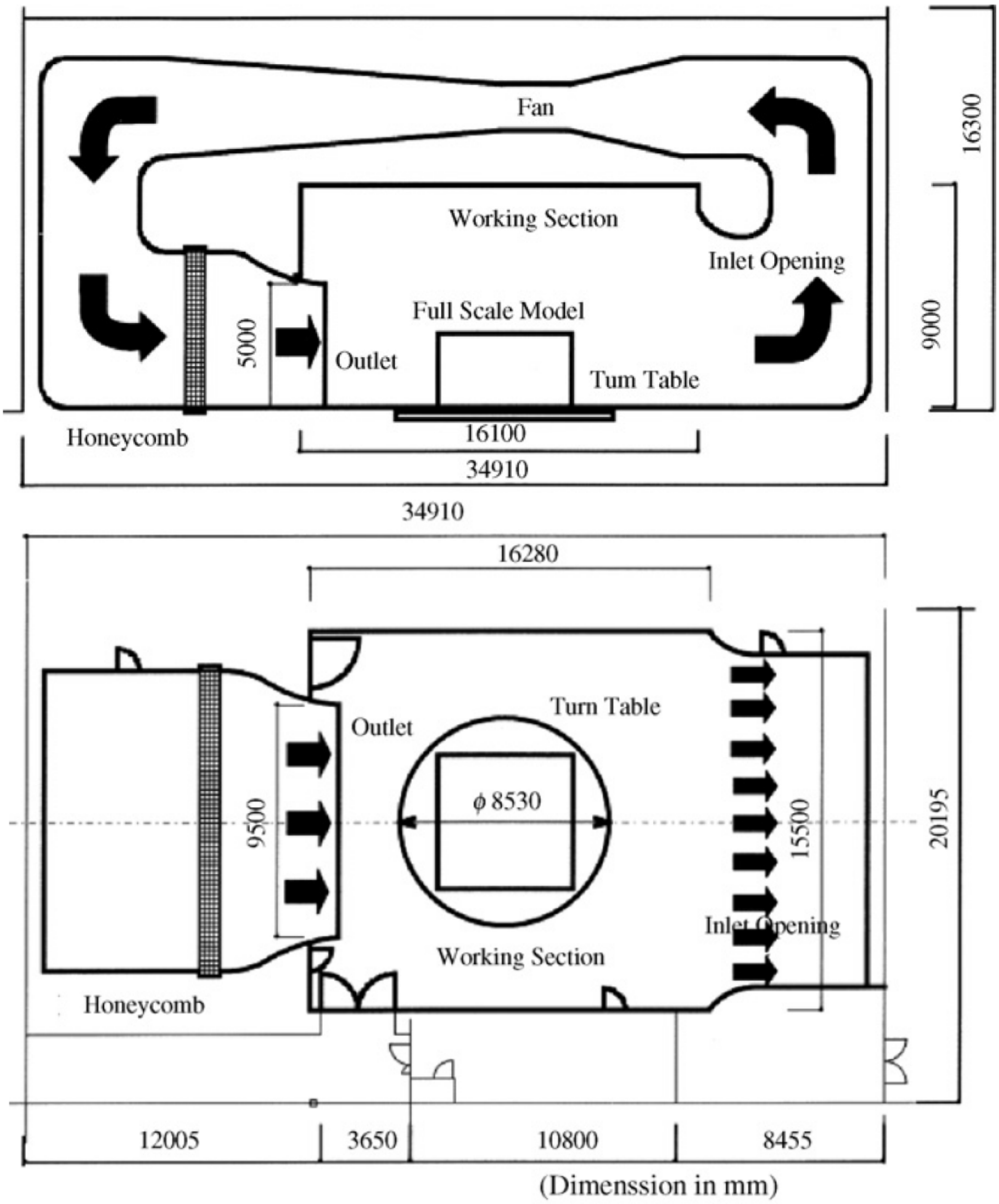

Figure 5.3 The schematic and the dimension of the wind tunnel in Japanese Building Research institute [2].

5.3.1.2 CFD Settings

For validation purpose, a wind-tunnel and a building model of exactly the same dimensions as the wind-tunnel experiment was built in ANSYS Design Modeler 13.0 (Figure 5.4). Four incident flow angles (0°, 90°, 180° and 270°) and two wind speeds (1 and 5 m/s) were simulated.

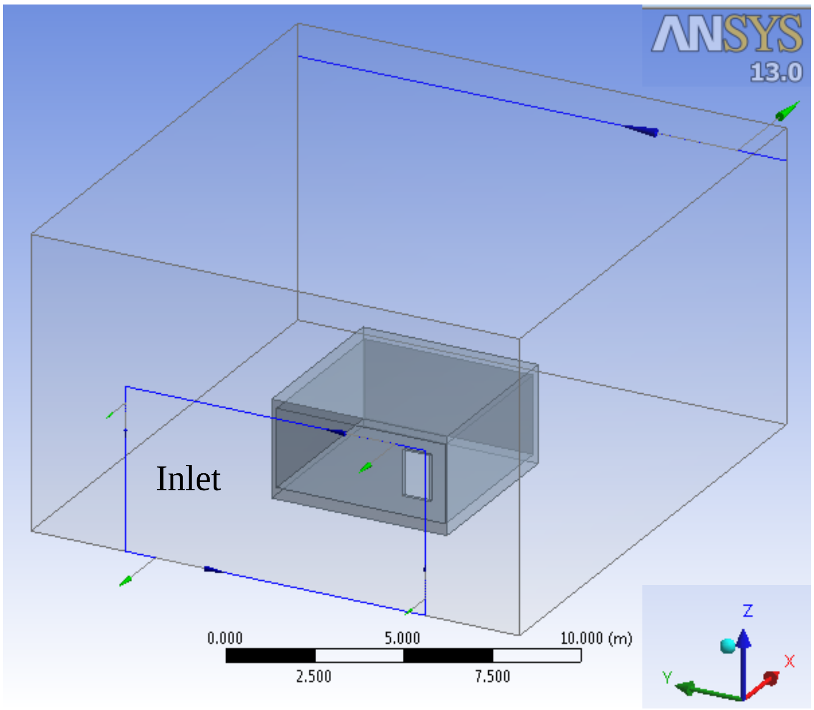

Figure 5.4 One of the wind-tunnel and the building models for CFD simulation.

A tetrahedral mesh (Figure 5.5) is used in the entire domain with three layers of inflation on all the building surfaces to make sure the first node is the region where $30 < y^+ < 300$ [6]. The simulated results prove that the y^+ was controlled well. No $y^+ > 300$ is found on the building wall surfaces and only a small portion of y^+ is less than 30. The element in the room and in the vicinity of the building is 0.14 m and all the elements are smaller than 0.5 m. The average element aspect ratio is 2.23. Given that the aspect ratio of one is ideal, the current meshing is acceptable.

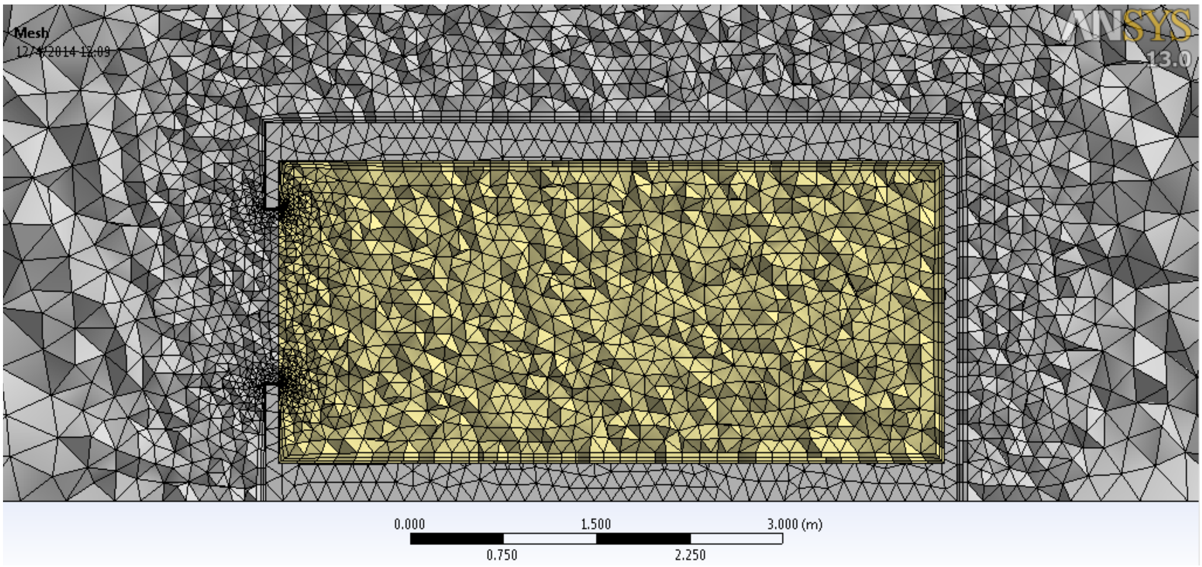

Figure 5.5 Cross-sectional view of the meshed building with the window facing left.

The steady formulation of the momentum and the turbulence equations are solved with the pressure-based solver using RANS turbulence model, specifically the standard k-ε turbulence model [7].

Continuity:

$$\frac{\partial}{\partial \mathrm{x}_i}(\rho u_i) = S_m \tag{5.9}$$

S_m is the defined mass source of CO emission, which is equal to 10^{-5} kg/m^3-s.

Momentum:

$$\frac{\partial}{\partial x_j}\left(\rho u_i u_j\right) = -\frac{\partial p}{\partial x_i} + \frac{\partial}{\partial x_j}\left[\mu\left(\frac{\partial u_i}{\partial x_j} + \frac{\partial u_j}{\partial x_i} - \frac{2}{3}\delta_{ij}\frac{\partial u_i}{\partial x_j}\right)\right] + \frac{\partial}{\partial x_j}\left(-\rho\overline{u_i' u_j'}\right) \tag{5.10}$$

μ is the viscosity of the fluid, δ_{ij} is the Kronecker's delta.

Transport equations for turbulence kinetic energy, k:

$$\frac{\partial}{\partial x_i}(\rho k u_i) = \frac{\partial}{\partial x_j}\left[\left(\mu + \frac{\mu_t}{\sigma_k}\right)\frac{\partial k}{\partial x_j}\right] - \rho\overline{u_i' u_j'}\frac{\partial u_j}{\partial x_i} - \rho\epsilon \tag{5.11}$$

Transport equations for dissipation rate of turbulence kinetic energy, ϵ:

$$\frac{\partial}{\partial x_i}(\rho\epsilon u_i) = \frac{\partial}{\partial x_j}\left[(\mu + \frac{\mu_t}{\sigma_\epsilon})\frac{\partial \epsilon}{\partial x_j}\right] + C_{1\epsilon}\frac{\epsilon}{k}(-\rho\overline{u_i' u_j'}\frac{\partial u_j}{\partial x_i}) - C_{2\epsilon}\rho\frac{\epsilon^2}{k} \quad (5.12)$$

The turbulent viscosity $\mu_t = \rho C_\mu \frac{k^2}{\epsilon}$.

The model constants are $C_{1\epsilon}$ = 1.44, $C_{2\epsilon}$ = 1.92, C_μ= 0.09, σ_k = 1.0, σ_ϵ = 1.3 [7].

The inlet of the domain is a velocity inlet with a uniform profile. The inlet turbulence is also uniform with a turbulence intensity *I* = 5% and the turbulence length scale *l* = 3 m, which is the smallest dimension of the building. The turbulence kinetic energy k and the dissipation rate ϵ can then be computed according to the following relationships.

$$k = \frac{3}{2}(UI)^2. \quad (5.13)$$

$$\epsilon = C_\mu^{3/4}\frac{k^{3/2}}{l}. \quad (5.14)$$

where *U* is the uniform velocity at the inlet.

The interior and exterior building surfaces are set to non-slip walls with standard wall functions and the wind-tunnel walls as slip walls. The slip wall boundary condition of the wind-tunnel walls are set to eliminate the formation of boundary layer in order to mimic the wind-tunnel experiment in [2]. It is reported in [2] that the measured flow at the outlet of the wind tunnel is still quite uniform. The pressure outlet with zero gauge pressure is the outlet boundary condition.

The passive species transport model is activated with CO-air as the mixture materials. CO is selected as the tracer gas because it has a similar molecular weight to the average molecular weight of the air so that the buoyancy effect can be negligible. ANSYS FLUENT computes the steady-state passive species transport by solving the following convection-diffusion equation,

$$\nabla \cdot (\rho \vec{v} Y) = -\nabla \cdot \vec{J} + S \tag{5.15}$$

where Y is the mass fraction of the species; $\vec{J}$ is the mass diffusion flux; and S is the rate of source release [7]. In this simulation, the entire volume of the room is defined as a volume source releasing CO at the rate $q = 10^{-5}$ kg/m^3-s.

In turbulent flows, the mass diffusion flux is computed in the following form,

$$\vec{J} = -(\rho D + \frac{\mu_t}{Sc_t}) \nabla Y \tag{5.16}$$

where D is the molecular diffusion coefficient of CO-air mixture = 2.88×10^{-5} m^2/s, and Sc_t is the turbulent Schmidt number. The default value $Sc_t = 0.7$ was taken [7].

Double precision is used in accordance with the recommendation by COST [8]. The simulations converge within 8000 iterations.

5.3.1.3 CFD Model Validation

Larson and Heiselberg [2] reported the air change rate (ACR) of the room and the same metric should be used for CFD validation. The ACR of the simulation is computed as follows.

The mass balance equation of the room at the steady state is

$$0 = q \cdot Vol + c_{in} \cdot Q_{in} - c \cdot Q_{out} \tag{5.17}$$

Where q is the volumetric source [kg/m^3-s]; Vol is the volume of the room [m^3]; c_{in} is the CO concentration of the flow that enters the room through the opening which is assumed to be zero [kg/m^3]; Q_{in} is the flow rate of the flow that enters the room [m^3/s]; c is the average CO concentration in the room [kg/m^3]; and Q_{out} is the flow rate of the flow that exit the room [m^3/s]. It should be noted that Q_{out} is not equivalent to the mean outflow at the window, because in single-sided ventilation, turbulence exchange can account for a large portion of air exchange. Hence, to emphasize the distinction, Q_{out} will be replaced by Q_{eff} meaning effective flow rate.

Therefore, the mass balance equation becomes

$$q \cdot Vol = c \cdot Q_{eff}. \tag{5.18}$$

Then ACR is

$$ACR = \frac{Q_{eff}}{Vol} = \frac{q}{c} = [s^{-1}]. \tag{5.19}$$

The CFD simulations output CO concentration at each node within the volume of the room and the average CO concentration can then be calculated. The ACR of each test case is presented in Table 5.1. Larson and Heiselberg illustrated the variation of the ACR in a figure (Figure 5.6) [2]. The ACR values of the corresponding cases are read from the figure and listed in Table 5.1. Figure 5.7 is a graphic representation of Table 5.1.

It is shown that at 90°, 180° and 270°, the simulated ACR and the measured ACR match well for both wind speed of 1 and 5 m/s (Figure 5.7), but when the incident angle is zero, that is when the flow is normal to the window, the simulated ACR is smaller than the measured ACR at wind speed of 1m/s and larger than the measured ACR at wind speed of 5 m/s. However, inspecting the data in Table 5.1 more carefully, it can be seen that as the wind speed increases from 1 m/s to 5 m/s, the simulated ACR also increases around 5 times for each incident angle. A similar proportional increase is found in measured ACR too expect for the wind angle of 0°, at which the ACR measured in the wind-tunnel experiment only increases from 5 hr^{-1} to 10.8 hr^{-1}. This discrepancy might suggest that at 0°, the actual air exchange mechanisms are more complex than what the CFD simulation assumes.

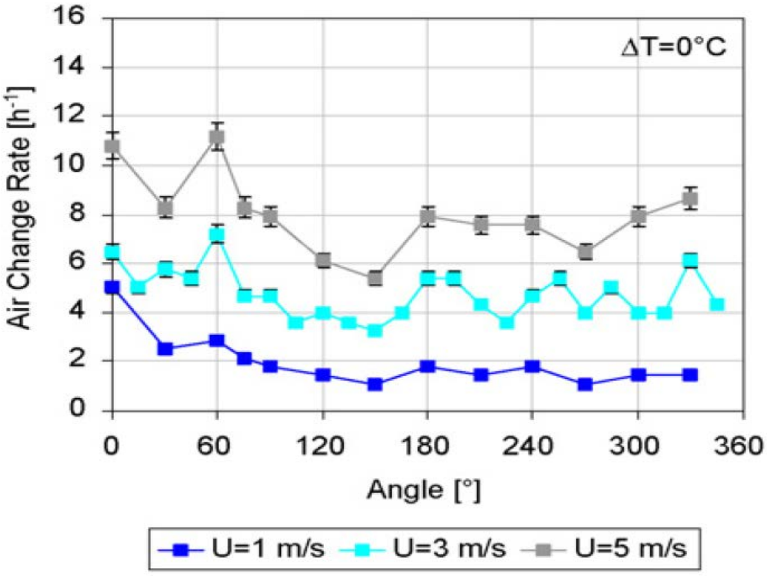

Figure 5.6 The effect on the air change rate of different incident angles and different wind speeds with zero temperature difference [2].

Table 5.1 Comparison of air change rates simulated from the CFD model (CFD) and measured in the wind-tunnel experiments in [2] (L&H) at wind speed of 1 and 5 m/s and four wind incident angles.

Wind Angle	**CFD-1 m/s**	**L&H-1 m/s**	**CFD-5 m/s**	**L&H-5 m/s**
0	3	5	18.6	10.8
90	1.1	1.8	5.4	8
180	1.4	1.8	7	8
270	1.4	1.2	7	6.5

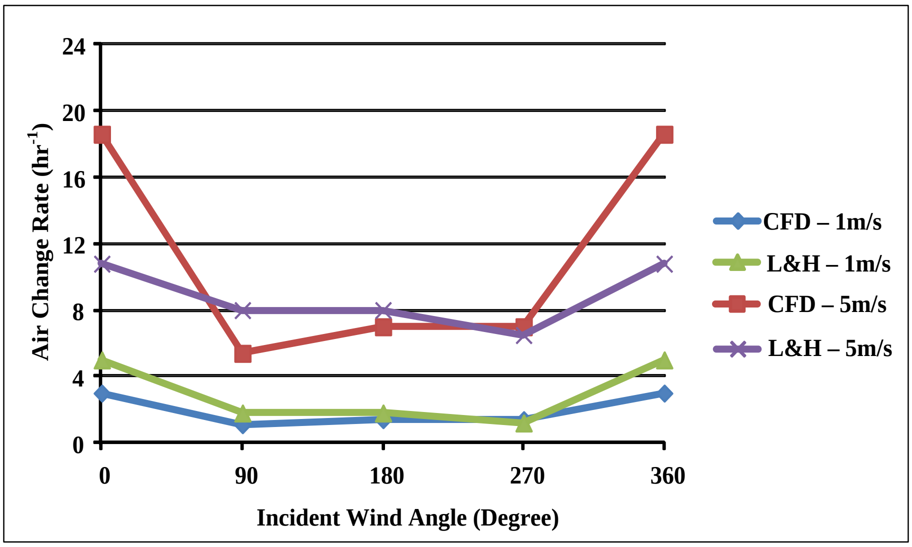

Figure 5.7 Air change rates simulated from the CFD model (CFD) and measured in the wind-tunnel experiments in [2] (L&H) at wind speed of 1 and 5 m/s and four wind incident angles.

In summary, the CFD model is capable of predicting the air change rate of an isolated one-room building with a single opening. The prediction is more accurate at incident wind of 90°, 180° and 270°. For normal incident flow, the simulated result can be different by a factor of two.

5.3.2 The Effect of Turbulence Intensity on ACR at Different Wind Angles

As reviewed in Chapter 2, Warren and Parkins [9] have demonstrated that the non-dimensional flow rate $Q*$ increases when the turbulence intensity of the free stream flow is higher. $Q*$ is defined as

$$Q^* = \frac{Q}{AU}, \tag{5.20}$$

Where Q is the volumetric flow rate; A is the area of the window and U, for wind-tunnel experiment with a uniform velocity profile, is the inlet velocity.

However, Warren and Parkins only evaluated two turbulence intensity levels (0.8% and 9%), which are also relatively small for flow in an urban canopy. In Chapter 4 Section 4.6, the turbulence observations from the field measurement at Treelodge are presented. The roof turbulence intensity $I_{rf} \approx 30\%$ for $U_{rf} > 2.5$ m/s ($I_{rf} = \sigma_{rf} / U_{rf}$). The later part of Section 4.6 shows that the turbulence level in the canopy is about 50% of the turbulence level at the roof ($\sigma_{u,v} / \sigma_{rf} \approx 0.5$). Combining the results, the turbulence intensity in the canopy computed with respect to the roof wind speed is $I_{c\text{-}rf} = \sigma_{canopy} / U_{rf} = 15\%$. In Section 4.4, it has been shown that the near ground wind speed is about 40% of the roof wind speed. Therefore, the canopy turbulence intensity computed with respect to the canopy wind speed is $I_{c\text{-}c} = \sigma_{canopy} / U_{canopy} = 37.5\%$.

In principle, it is not valid to compare the turbulence intensity in the urban canopy, either $I_{c\text{-}rf}$ or $I_{c\text{-}c}$, with the free stream turbulence intensity in the wind tunnel. However, most studies on single-sided ventilation have only considered an isolated building, not an array of buildings. Hence, the effect of the turbulence produced by the building canopy on the single-sided ventilation cannot be predicted directly from the existing studies. In the current study, it is assumed that it is the turbulence level and characteristics right at the window that affect the ventilation effectiveness. Therefore, the effect of turbulence is still investigated with a model of an isolated building in the current study for the sake of simulation time saving but with a larger range of free stream turbulence intensity inputs to mimic the condition of the urban canopy.

The same CFD geometry and settings that have been validated in the previous section are used, with five different turbulence intensities I = 1%, 5%, 10%, 20% and 40%, specified at the inlet. For I = 5% and 20%, two inlet wind speeds 1 m/s and 5 m/s are tested and it is found out that the ACR simply increases 5 times when the wind speed increases 5 times.

Therefore, in the other simulations, only the inlet wind speed of 5 m/s is used. Four incident wind angles are tested, 0°, 90°, 180° and 270°.

Figure 5.8 shows the flow pattern in the room at wind speed of 1 m/s, turbulence intensity of 5% and incident angle of 0°. Slow flow circulations along the walls of the room are seen. The velocity of the flow is higher at the entrance of the room, and gradually reduces. The streamlines in Figure 5.8c suggest that some of the particles entered may be trapped in the room and come to an almost zero velocity. In general, the mean flow movement in the room is very slow.

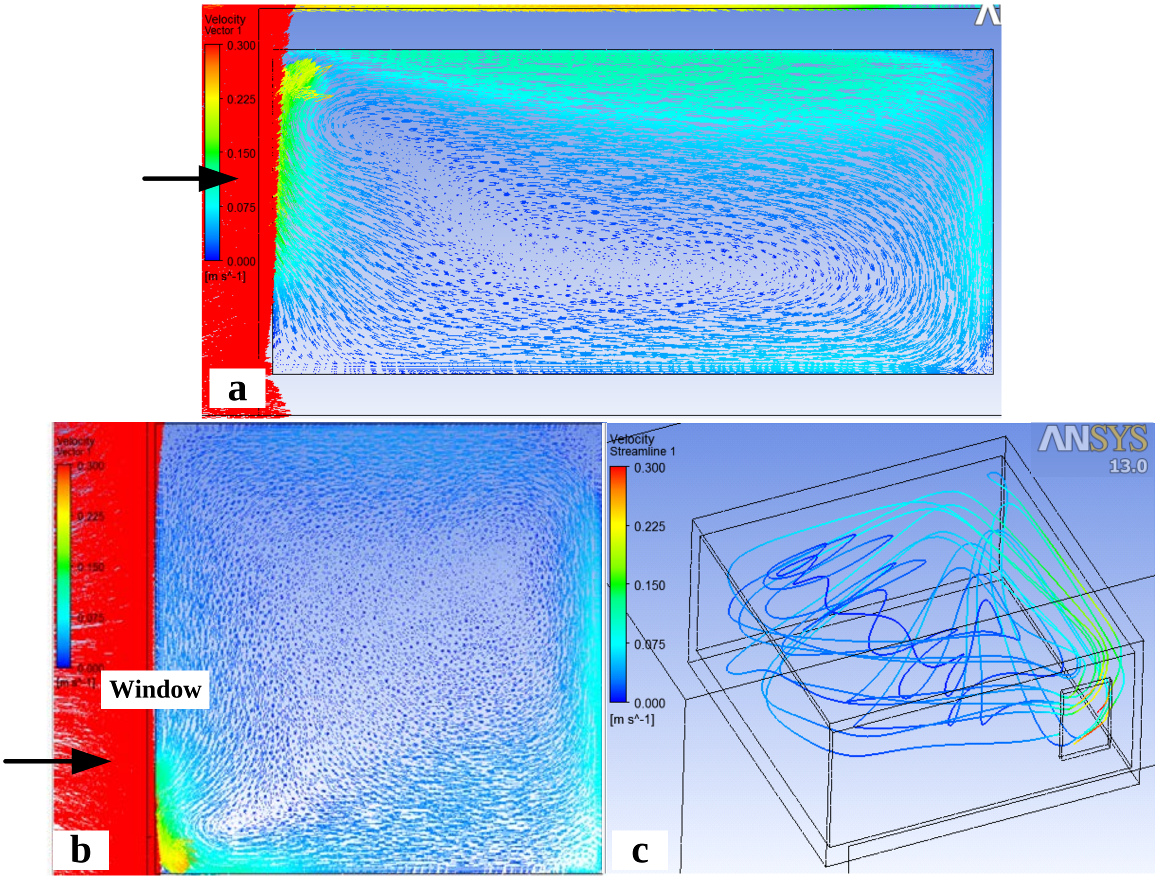

Figure 5.8 a. Side view of the velocity vectors in the room on a plane cut through the middle of the window at incident angle of 0°; b. Top view of the velocity vectors in the room on a plane at mid-height of the window at incident angle of 0°; c. Streamlines at incident angle of 0°.

The differences in CO concentration in the room at 5% input turbulence intensity and 20% input turbulence intensity are clearly illustrated in Figure 5.9 and Figure 5.10 for the incident angle of 0° and 90° respectively. The CO concentration reduces substantially at the higher turbulence level. The ACR of each test case is tabulated in Table 5.2 and plotted in Figure 5.11.

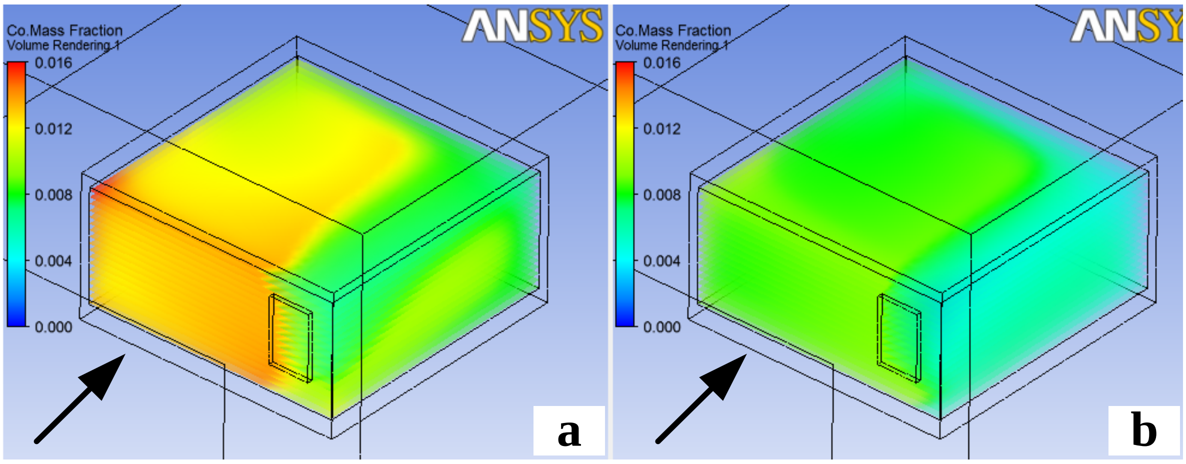

Figure 5.9 The CO concentration distributions at wind speed of 1 m/s, incident wind angle of 0°, and a) turbulence intensity of 5%; b) turbulence intensity of 20%.

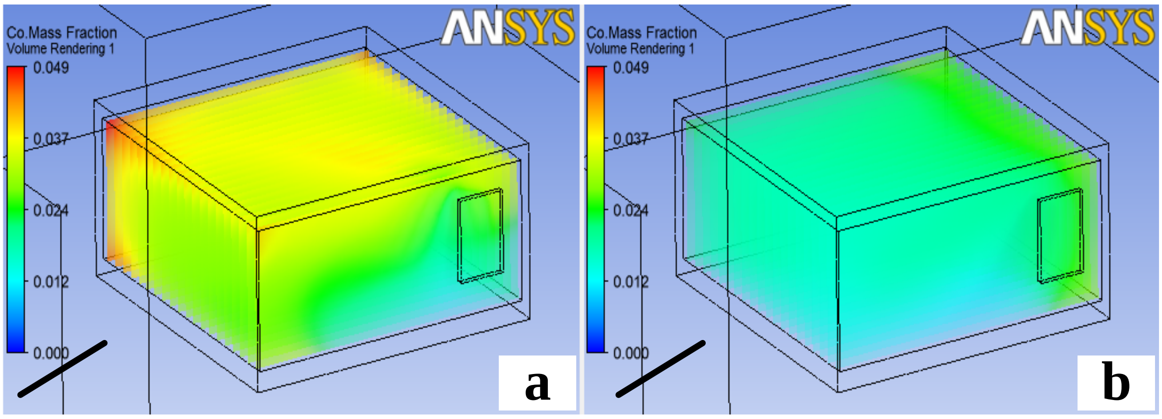

Figure 5.10 The CO concentration distributions at wind speed of 1 m/s, incident wind angle of 90°, and a) turbulence intensity of 5%; b) turbulence intensity of 20%.

Table 5.2 Effect of turbulence intensity on air change rate at different incident wind angles.

Turbulence Intensity *I*	**Incident Wind Angle**			
	0	90	180	270
1%	17.2	4.3	7	6.7
5%	18.6	5.4	7	7
10%	20.9	6.8	6.9	7.3
20%	22.4	8.1	6	8.4
40%	26.0	8	4.8	9.4

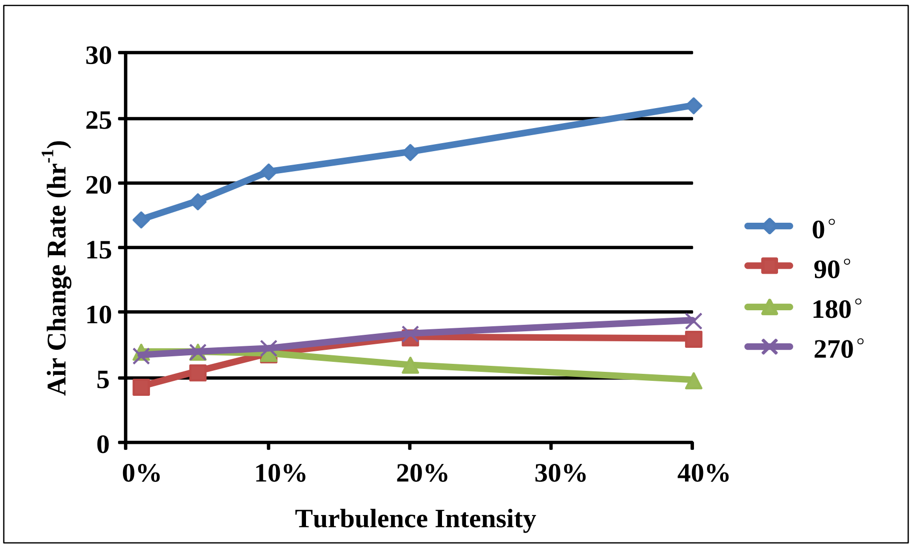

Figure 5.11 Effect of turbulence intensity on air change rate at different incident wind angles.

The air change rate increases with increasing turbulence intensity for all wind angles except for 180°. The increase is most significant for the wind angle of 0°. Moreover, the increase in ACR is faster when the turbulence intensity *I* changes from 1% to 10%. The effect tends to taper with further increment of *I*.

The velocity contours and the turbulence kinetic energy (TKE) contours at the window at different incident wind angles are plotted to investigate the reasons behind the changes of the ACR with turbulence intensity. For wind angles of 0°, 90° and 270°, the velocity of the flow near the window decreases with increasing free stream turbulence intensity *I*, but the TKE level near the window increases with increasing *I*. Since the ACR also increases with *I*, it suggests that the effect of TKE on single-sided ventilation is stronger than the effect of the mean flow. The wind angle of 180° is different, because it is found that when *I* is high, both the velocity and TKE in the wake region behind the building are lower than when *I* is low. Therefore, the window on the leeward side is disadvantageous for single-sided ventilation when the free stream turbulence intensity is high.

When the ACR is known, the effective flow rate Q_{eff} can be calculated from Equation 5.19,

$$Q_{eff} = ACR \cdot Vol. \tag{5.21}$$

Then the non-dimensional Q^*_{eff} can be computed according to Eq. 5.14. The trend of Q^*_{eff} variation is the same as ACR because the volume of the room is fixed (Table 5.3). As reviewed in Section 2.5.2 Chu et al. [10] summarized a few experiments and found that the range of Q^* is [0.015, 0.04]. Alternatively, $Q^* = 0.025 \pm 0.01$ roughly holds for a number of experiments. The Q^*_{eff} calculated from the simulations is within this range for all turbulence intensities tested at the incident wind angles of 90°, 180° and 270°. However, for the wind angle of 0°, Q^*_{eff} is larger than the prediction by as much as four times. Given that the normal incident wind is used in most wind tunnel experiments in the literature from which the estimate of Q^* is generated, it is supposed that the simulations of the flow at normal wind angle may be inaccurate. One explanation for the inaccuracy might be that the k-ε model produces too much turbulence in regions of stagnant flow [11]. In the current model, the stagnation zone is on the windward wall. At 0° the window is under the influence of the elevated turbulence level, which leads to higher ventilation rate than expected.

Table 5.3 Variation of Q^* with turbulence intensities at different incident wind angles.

Turbulence Intensity *I*	**Incident Wind Angle**			
	0	90	180	270
1%	0.055	0.014	0.022	0.021
5%	0.060	0.017	0.024	0.022
10%	0.064	0.022	0.022	0.023
20%	0.071	0.026	0.019	0.027
40%	0.083	0.026	0.015	0.030

Reference

1. Truong, P.H., “Recommendations for the Analysis and Design of Natrually Ventilated Buildings in Urban Areas,” Thesis of Master of Science in Building Technology, Massachusetts Institute of Technology, 2012.

2. Larsen, T.S., and Heiselberg, P., “Single-Sided Natural Ventiation Driven by Wind Pressure and Temperature Difference,” *Energy and Buildings*, 40, pp 1031-1040, 2008.

3. Vickery, B.J., Baddour, R.E. and Karakatsanis, C.A., “A Study of the External Wind Pressure Distributions and Induced Internal Ventilation Flow in Low-Rise Industrial and Domestic Strucctures.” Report No. BLWT-SS#-1083, Boundary Layer Wind Tunnel Laboratory, University of Western Ontario, Jan 1983.

4. ASHRAE. “Chapter 24 Airflow around Buildings,” in *2009 ASHRAE Handbook—Fundamentals (SI)*, 2009, pp. 24.1.

5. Sawachi, T., “Detailed Observation of Cross Ventilation and Airflow through Large Openings by Full Scale Building Model in Wind Tunnel,” in *Proceedings of ROOMVENT 2002*, pp 565-568, 2002.

6. ANSYS, Inc. “ANSYS FLUENT User’s Guide,” ANSYS, Inc, Nov 2010, Release 13.0.

7. ANSYS, Inc. “ANSYS FLUENT Theory Guide,” ANSYS, Inc, Apr 2009, Release 12.0.

8. Franke, J., Hellsten, A., Schlunzen, H., and Carissimo, B., “Best practice guideline for the CFD simulation of ows in the urban environment,” COST Action 732: Quality assurance and improvement of microscale meteorological models, Technical report, COST Office, May 2007.

9. Warren, P.R., and Parkins, L.M., “Single-Sided Ventilation through Open Windows,” *Proceedings ASHRAE SP 49*, pp 209-228, 1985.

10. Chu, C.R., Chen, R.H, and Chen, J.W., “A Laboratory Experiment of Shear-Induced Natural Ventilation,” *Energy and Buildings*, 43, pp 2631-2637, 2011.

11. Schatzmann, M., and Leitl, B., “Issues with Validation of Urban Flow and Dispersion CFD Models,” *Journal of Wind Engineering and Industrial Aerodynamics*, 99, pp 169-186, 2011.

Chapter 6 Conclusion and Future Work

6.1 Conclusion

This research work aims to develop an in-depth understanding of the mean flow and turbulence in high-rise building neighborhoods in order to predict the outdoor and indoor ventilation potentials of the neighborhoods. The goal is set because effective ventilations could improve the thermal comfort and the air quality for the residents, creating a better living environment. Despite the popularity of high-rise residential buildings, the knowledge of the airflow characteristics of such neighborhoods is limited. The main research methods employed in this study are the field measurement and the CFD simulations.

The field measurement campaign was carried out at a high-rise residential neighborhood in Singapore in the northeast (NE) and the southwest (SW) monsoon seasons to investigate the flow and turbulence characteristics. The neighborhood consists of two rows of buildings and a canyon in between. Integrated weather stations were installed at the pedestrian level in the canyon and in the buildings at high spatial resolution. Reference wind velocities at the roof and at the airport standard meteorological weather station were also measured. The measurement lasted for two weeks in each monsoon season.

The unstable conditions are found at the measurement neighborhood a majority of the time during the field campaign. Relatively homogeneous wind speed was observed at the pedestrian level in the canyon between buildings when the angle of attack is less than 60° in both NE and SW monsoon seasons. The angle of attack is defined as the angle between the incident wind and the normal of the canyon. In such a case, the average ratio of the pedestrian wind speed to the roof wind speed is around 0.4. When the angle of attack is larger than 60°, flow channeling along the canyon takes place and the pedestrian level wind speed increases at most locations. The vertical wind speed profiles are found to be approximately uniform in the downwind buildings in both monsoon seasons. The turbulence characteristics are also studied. The turbulence intensity at the roof tends to decrease with increasing wind speed, but the root mean square of turbulence velocities in the canyon scaling on the turbulence velocity at the roof are highly spatially and temporally uniform. The in-canopy turbulence is about 40%-60% of the turbulence level at the roof.

Furthermore, the flow patterns are compared between the NE and the SW monsoon seasons, because the northeast of the measurement site is an open terrain whereas the south is the urban area. For a given wind speed at the airport reference station, it is found that the wind speed at the roof in the NE monsoon can be as twice as the roof wind speed in the SW monsoon. The canyon wind speed in the NE monsoon is also almost twice the canyon wind speed in the SW monsoon. The situation is worse when it comes to the wind speed in the buildings. The wind speed in the downwind building in the SW monsoon is only one quarter of the wind speed in the NE monsoon. In a word, larger amount of airflow can enter the neighborhood when there is less obstruction upwind of it. For the neighborhood where the field measurement was conducted, the outdoor ventilation condition is better in the NE monsoon than the SW monsoon.

The wind speed measured at the openings in the building during the field campaign can also be used to approximate the cross-ventilation velocity of the building. Besides, the cross-ventilation flow rate of a building in a neighborhood with certain frontal and plan area densities (λ_f and λ_p) can be computed from the wind pressure coefficients associated that pair of λ_f and λ_p, which are obtained empirically from experiments. Relatively good agreement is found between the measured and the computed ventilation velocities.

The indoor ventilation through a single opening is studied using steady-state CFD simulations with a passive species transport equation calculated on top of the momentum equations. The model was validated with a wind-tunnel experiment reported in the literature before the effect of turbulence intensity was tested at different wind angles. It is found that the air change rate increases with increasing turbulence intensity when the only window is on the windward or the side walls. In contrast, the air change rate decreases slightly with increasing turbulence intensity when the window is on the leeward wall. Moreover, the simulation results show that when the window is on the side or the leeward walls, the non-dimensional flow rate $Q*$ is in the range of 0.025±0.01, but the $Q*$ for window in the windward wall appears to be elevated.

6.2 Future work

More field measurement campaigns can be conducted in high-rise building neighborhoods with different building configurations and arrangements to investigate whether the wind speed and the turbulence ratios obtained in this study can be generalized. Airflow measurements in the actual living unit can also be useful in determining the ventilation flow rate. Moreover, measurement of other variables can be considered such as the surface temperature and the radiations, because the thermal dynamics can be an important determinant of the airflow in the neighborhood.

CFD simulations on the high-rise neighborhood where the field campaign is conducted can be performed to develop a better understanding of the flow patterns. Interesting results may be revealed by simulations on simple building geometry. For example, a canyon with two solid walls and a canyon similar to the measurement site in the current study (“a porous canyon”) can be simulated. Perhaps no change in flow pattern will be found until a certain porosity is reached.

The single-sided ventilation can be combined with the high-rise building neighborhood setting, by, for example, simulating a room with a single window in an array of high-rise buildings. Parameters such as the location of the window (e.g. lower part of the building or upper part of the building) and the orientation of the window (e.g. windward or leeward) can be manipulated. The effect of the type of the window (sliding or casement window) on single-sided ventilation is also worth studying.